

# **Self-Organisation of Confined Active Matter**

---

Hugo Wioland

Churchill College

This dissertation is submitted for the degree of

*Doctor of Philosophy*

December 2014



## Preface

This dissertation is the result of my own work and includes nothing which is the outcome of work done in collaboration except as declared in the preface and specified in the text.

It is not substantially the same as any that I have submitted, or, is being concurrently submitted for a degree or diploma or other qualification at the University of Cambridge or any other University or similar institution except as declared in the preface and specified in the text. I further state that no substantial part of my dissertation has already been submitted, or, is being concurrently submitted for any such degree, diploma or other qualification at the University of Cambridge or any other University of similar institution except as declared in the Preface and specified in the text.

In chapter 1, I describe the self-organisation of bacterial suspensions, illustrated by experiments in special microchambers. These chambers have been designed and prepared by Vasily Kantsler, a post-doc in Ray Goldstein's group at the time and now an assistant professor at the University of Warwick. I performed the experiments and the analysis.

In chapter 2, I present experimental results in flattened drops and race-tracks. I have designed chambers and carried out all experiments. I analysed movies using MATLAB (The MathWorks) plugin mPIV, which has been previously adapted for time averaging by Aurelia Honerkamp-Smith, a post-doc in Ray Goldstein's group. Experimental results on flattened drops have been published in *Physical Review Letters* [1].

Chapter 3 first introduces an experimental method I have developed to simultaneously measure the directions of swimming and of motion of bacteria. Mutant strain amyE::hag(T204C) DS1919 3610 is a gift from Linda Turner Stern, a research associate at the Rowland Institute, and Daniel

Kearns, an associate professor at Indiana University. This mutant has been created in Daniel Kearns' group and he also helped me on protocol technicalities. The second part of this chapter presents *in silico* studies. Enkeleida Lushi, who visited the Newton Institute and is now a post-doc at Brown University, wrote and performed all simulations. I only thoroughly discussed the results with her. Experiments on fluorescent bacteria and simulations in flattened drops have been published in *Proceedings of the National Academy of Sciences* [2]. Experiments and simulations results in racetracks will be submitted in the near future [3].

Chapter 4 introduces experimental and theoretical work on lattices of vortices. For this project, I collaborated with Francis Woodhouse, a former PhD student in Ray Goldstein's group and now a research assistant professor at The University of Western Australia, and Jörn Dunkel, a former post-doc in Ray Goldstein's group and now an assistant professor at MIT. I carried out all experiments. Theories are the result of discussions between the three of us and I performed the direct analyses presented in this manuscript.

## Acknowledgements

I would like to warmly thank Ray Goldstein for welcoming me in his lab, first as a master student and then as a PhD student. It has been a great pleasure to work in Cambridge and to discover marvellous organisms like *Bacillus*, *Chara*, and *Volvox*.

I would also like to thank all members of Ray Goldstein's and Eric Lauga's groups, in particular Kyriakos Leptos, for his regular biological advices, Aurelia Honerkamp-Smith and Vasily Kantsler, for their help on experiments, Francis Woodhouse and Jörn Dunkel, for great collaborations, Jocelyn Dunstan Escudero, Pierre Haas, Philipp Khuc Trong and François Peaudecerf, for fruitful discussions.

Enkeleida Lushi has considerably contributed to this PhD, and I am thankful for our collaboration. I also would like to thank Linder Turner Stern and Daniel Kearns for their friendly help on experiments with fluorescent bacteria.

Finally, I am extremely thankful to all colleagues who proofread this manuscript, including Stephanie Höhn, Emily Riley, Kirsty Wan and others cited above.

This work was supported by the EPSRC and ERC Advanced Investigator Grant 247333.

## Summary

Active matter theory studies the collective behaviour of self-propelled organisms or objects. Although the field has made great progress in the past decade, little is known of the role played by confinement and surfaces. This thesis analyses the self-organisation of dense bacterial suspensions in three different microchambers: flattened drops, racetracks and lattices of cavities.

Suspensions of swimming bacteria are well-known to spontaneously form macroscopic quasi-turbulent patterns such as jets and swirls. Confinement inside flattened drops and racetracks stabilises their motion into a spiral vortex and wavy streams, respectively.

We have quantitatively measured and analysed bacterial circulation and discovered cells at the interfaces to move against the bulk. To understand this phenomenon, we developed a method able to measure simultaneously the directions of swimming and of motion. Experiments in drops reveal that cells align in a helical pattern, facing outward and against the main bulk circulation. Likewise, bacteria in racetracks share a biased orientation against the overall stream.

Particle-based simulations confirm these results and identify hydrodynamic interactions as the main driving force: bacteria generate long-range fluid flows which advect the suspension in the bulk against its swimming direction, resulting in the double-circulation pattern.

We have finally injected dense suspensions of bacteria into lattices of cavities. They form a single vortex in each cavity, initially spinning clockwise or counterclockwise with equal probabilities. Changing the topology of the lattice and the geometry of connections between cavities allows us to control the lattice state (random, ferromagnetic, antiferromagnetic, or

unstable). Edge currents along interfaces and connections appear to determine the lattice organisation. We finally propose an Ising model to understand experimental results and estimate Hamiltonian and interactions parameters.

This work opens new perspectives for the study of active matter and, we hope, will have a great impact on the field.



# Contents

<b>1</b>	<b>Introduction</b>	<b>1</b>
1.1	Active Matter . . . . .	2
1.2	Bacterial Motion . . . . .	4
1.2.1	Different Motility Mechanisms . . . . .	4
1.2.2	Swimming in <i>Bacillus subtilis</i> . . . . .	5
1.2.3	Fluid Flows . . . . .	10
1.3	Dense Suspensions of Bacteria . . . . .	15
1.3.1	Collective Motion of Bacteria . . . . .	15
1.3.2	Modelling Active Matter . . . . .	19
1.4	Bacteria under Confinement . . . . .	23
1.4.1	Effect of Interfaces on the Swimming of Single Microswimmers	24
1.4.2	Active Matter under Confinement . . . . .	26
1.4.3	Thesis Outlook . . . . .	27
<b>2</b>	<b>Bacteria under circular and linear confinement</b>	<b>29</b>
2.1	Introduction . . . . .	29
2.2	Flattened drops . . . . .	31
2.2.1	Protocol . . . . .	31
2.2.2	Results . . . . .	36
2.2.3	Discussion . . . . .	43
2.3	Racetracks . . . . .	46
2.3.1	Protocol . . . . .	47
2.3.2	Results . . . . .	49
2.3.3	Discussion . . . . .	57

2.4	Cross channels . . . . .	60
2.5	Conclusion . . . . .	61
<b>3</b>	<b>Bacterial Self-Organisation Mechanisms and the Role of Fluid Flows</b>	<b>65</b>
3.1	Introduction . . . . .	65
3.2	Experimental Observation of Fluid Flows . . . . .	66
3.2.1	Introduction . . . . .	66
3.2.2	Protocol . . . . .	67
3.2.3	Results . . . . .	68
3.2.4	Discussion . . . . .	71
3.3	Simulation . . . . .	73
3.3.1	Model . . . . .	73
3.3.2	Results . . . . .	75
3.3.3	Discussion . . . . .	83
3.4	Conclusion . . . . .	85
<b>4</b>	<b>Lattice of Vortices</b>	<b>87</b>
4.1	Introduction . . . . .	87
4.2	Experiments . . . . .	88
4.2.1	Protocol . . . . .	88
4.2.2	Analysis . . . . .	90
4.2.3	Results . . . . .	91
4.2.4	Discussion . . . . .	94
4.3	Modelling the Square Lattice as an Ising System . . . . .	99
4.3.1	Model . . . . .	99
4.3.2	Direct Analysis of the Experiments . . . . .	101
4.3.3	Results . . . . .	108
4.4	Conclusion . . . . .	112
<b>5</b>	<b>Conclusion</b>	<b>115</b>

# Chapter 1

## Introduction

“Order without power”<sup>1</sup>. It is in these words that Pierre-Joseph Proudhon, in his book “The Confessions of a Revolutionary” [4], defines the anarchist society... or bacterial communities.

Bacteria are certainly anarchists according to the etymological definition, “without rulers”, as their behaviour is usually not dictated by a subset of the population. And yet they can achieve strong ordering as observed in macroscopic colonies which bacteria form [5, 6, 7]. In such structures, there exist no notion of government or property but rather cooperation, collective decision making and public goods [8, 9, 10].

Comparing bacterial colonies to anarchist states is of course highly anthropomorphic and it would be more accurate to speak of self-organisation instead. Self-organisation can be described as the process by which large scale order arises from interactions between individual agents only. In the case of bacteria, interactions can take various forms. Chemical signalling can be used to communicate on the cell physiological status, measure the density of bacteria (quorum sensing) or inform on environmental conditions [9, 11, 12, 13, 14]. Mechanical interactions such as direct steric repulsion or hydrodynamic forces can affect the spatial organisation and dynamics of colonies [5, 15, 16, 17]. Other complex mechanisms such as DNA exchange can also play a critical role on population behaviour [18].

These interactions, taking place at the level of individual cells, can lead to various collective behaviours: population migration [9, 19, 20], formation of structured

<sup>1</sup>“L’anarchie, c’est l’ordre sans le pouvoir.”

biofilms [5, 6, 7] and fruiting bodies [12, 21], collective adaptation of phenotype [11, 14], cannibalism [15, 22], and many more.

Self-organisation and collective behaviours can of course be found in many other organisms, from the formation of fruiting bodies in the slime mold *Dictyostelium* [23], foraging in social insects [24], to the motion of flocks of birds [25, 26]. These behaviours have not only fascinated biologists but also physicists. In particular a new subfield has recently emerged, namely active matter, which seeks to understand the physical properties of self-organising systems under motion [27].

## 1.1 Active Matter

Active materials are composed of a set of objects, organisms or molecules able to move in their environment by internally consuming energy. Unlike classical passive materials, they are by nature out of equilibrium. These objects then interact through various forces and can self-organise into large stable or unstable patterns.

Examples of active matter range from submicron molecules to large mammals and can either be extracts and full living organisms, or artificial objects. I present here a non exhaustive list of commonly studied systems:

**Flocks of birds and shoals of fishes** Animals are able to move in groups, in these two cases, the visual cues are predominant to explain the mechanisms of organisation [25, 26]. Birds for example have been shown to finely control their density depending on the flock size [25]. Motion in flocks and shoals can be a defence mechanism against predators.

**Swarms of locusts** Even though locusts are not truly social insects ('eusocial'), they often live in swarms, and can collectively migrate [28]. Cannibalism has been proposed to explain the motion of marching locust, which adapt their orientation to avoid contact and being eaten [29].

**Fruiting bodies of *Dictyostelium*** The slime mold *Dictyostelium* is an eukaryotic organism that exhibits both unicellular and multicellular life styles. When nutrients become scarce, cells attract each other by chemical signalling and aggregate into

a slug, precursor of the fruiting body [23]. At the top of the fruiting body, *Dicystelium* turns into spores able to survive starvation. A similar fruiting body formation happens in Myxobacteria, also called “slime bacteria” [12, 21].

**Swimming bacteria, algae and sperm cells** Numerous microorganisms have evolved to swim and explore their environment. Population of microswimmers can form various circulation patterns: dense bacteria can generate turbulent swirls [7, 30, 31, 32]; algae, bioconvection [33]; and sperm cells, arrays of vortices [34]. The behaviour of microswimmers will be described in further detail in the rest of this thesis.

**Eukaryote cytoskeleton** The skeleton of eukaryotic cells is mainly composed of filaments, including actin and microtubules, on which many proteins interact. These proteins can be purified to create artificial active system *in vitro*. When microtubules and kinesin motors are copurified, the latter slide filaments past each other, resulting in a collective rearrangement exhibiting  $+\frac{1}{2}$  and  $-\frac{1}{2}$  defects typical of liquid crystal assembly [35, 36]. An alternative setup is to place actin filaments on a carpet of myosin motors, themselves bound to a surface. At high concentration, filaments, gliding on the myosins, can organise into ordered clusters (‘swarms’), travelling bands and migrate uniformly [37, 38].

**Bristlebots** Centimetre-long objects are in contact with a surface through asymmetric bristles. Vibration of the surface or of the bots results in a directed motion. Bristlebots interact through direct repulsion and have been shown to form stable vortices under confinement [39, 40, 41].

**Janus particles** These micron-sized colloids have two sides with different chemical properties. One half typically reacts with a compound present in the medium, generating a chemical gradient that sets the particles into motion [42]. Janus particles have been shown to decelerate at high density thus assembling into dense immotile groups [43].

These systems exhibit a great variation in their form, propulsion mechanism, interaction and resulting pattern formation. Nature teems with active matter and new artificial forms are quickly being developed.

I decided to work with suspensions of swimming bacteria. They present several advantages: they are simple to grow and prepare, can be controlled either by changing external conditions (e.g. oxygen concentration) or by using mutants, are easy to image, and most importantly can self-organise into a variety of dynamic patterns.

In the following sections, I first describe how bacteria explore their environment with particular focus on the role of fluid flows. I then present experimental and theoretical results on dense bacterial suspensions. I finally introduce the topic of my PhD: how confinement and interfaces modify the self-organisation of bacterial suspensions.

## 1.2 Bacterial Motion

### 1.2.1 Different Motility Mechanisms

Bacteria make an extremely diverse kingdom and as such have developed numerous locomotion mechanisms, which can be listed into five main groups [44, 45, 46]:

**Swimming** Bacteria grow helical flagella that are spun by a rotor embedded in the membrane. The rotation of the flagella creates a net force on the fluid and on the body, thus propelling the cell [47]. Depending on the species, a bacterium can have one or numerous flagella, placed at one or both ends, in the middle or covering the entire body [48]. The swimming motion is described in more detail below. Some bacteria have also been found to be covered in short cilia that beat in waves similar to *Paramecia* locomotion [49, 50].

**Swarming** As for swimming, swarming is also driven by flagella. Yet, not all swimming bacteria can swarm. This motion happens at the interface of a gel and air and has mostly been studied on agar plates. In order to swarm, bacteria need to grow numerous flagella (called peritrichous bacteria). They often produce surfactant, creating a thin film in which they can move. Bacteria can form dense groups in which they are aligned and move in a common direction, thus giving them the name *swarms* (figure 1.1a). The migration of swarming bacteria on an agar plate can result in macroscopic patterns whose shape depends on nutrient concentration and surface stiffness [19].

**Twitching** Some bacteria are equipped with long pili which they extend, bind to surfaces and retract to move towards the attachment point (figure 1.1b) [51]. As in swarming, bacteria exhibit collective motion on agar plates, which can take the form of dense groups.

**Gliding** This motion is the least understood and most probably corresponds to different mechanisms depending on the specific species. In some bacteria, focal adhesion points are placed on an helical pattern around the cell body and are actively displaced from one end to the other. When attached to a surface, this motion propels the bacterium in a forward and rotating fashion (figure 1.1c) [52, 53].

**Sliding** Bacteria growing on agar plates form colonies initially limited to a single layer. When expanding, steric repulsion between bacteria leads to the outward motion of the cells (figure 1.1d). This mechanism cannot exactly be called motility as, apart from the cell growth, it is passive. Yet it is necessary to understand the migration and structure formation of bacterial colonies [16, 17].

## 1.2.2 Swimming in *Bacillus subtilis*

*Bacillus subtilis* is one of the most studied bacteria. It can grow multiple flagella and is a model for swarming, swimming and active matter. It is also extensively used to study the formation of biofilms, sporulation, chromosome replication, etc. Even if the general mechanism for swimming is conserved among bacteria, the exact actuation varies between species and I only describe here that of *B. subtilis*.

### Flagellar Structure

Flagella are organelles growing at the outside of the cell. They are composed of three main parts: a long filament, a rotor and a hook joining the two (figure 1.2).

The filament is a hollow tube assembled as a periodic array of subunits: the protein flagellin. Each subunit migrates inside the flagella from the cell body to the tip where it is added, the filament then grows from its free end rather than its base, independently of the flagella length [54, 55].

To form the hollow filament, flagellin assemble into a closed array of eleven fibrils or protofilaments [56]. Flagellin can take two conformations, right and left type.

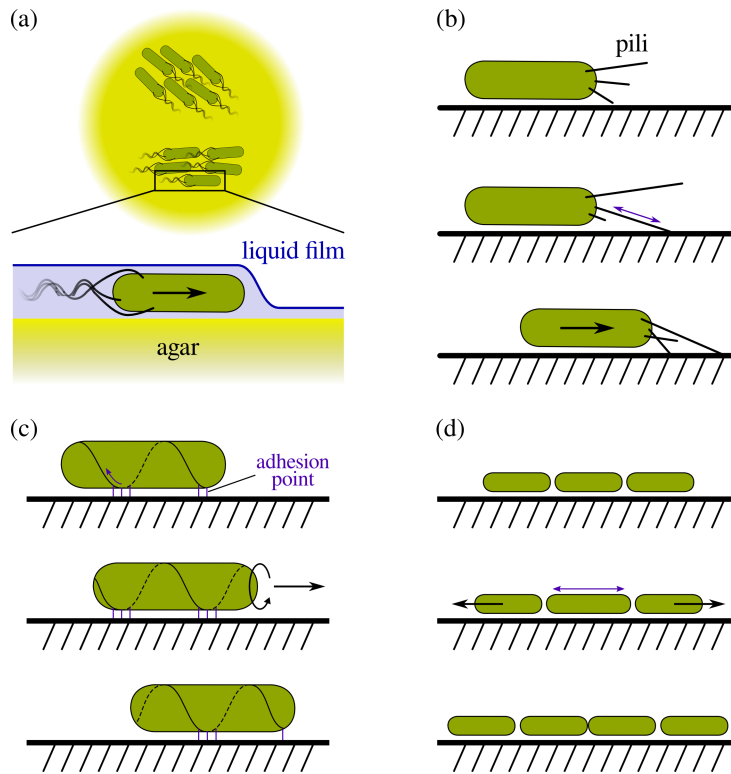


Figure 1.1: Locomotion mechanisms in various bacterial species. (a) Swarming: flagellated bacteria move on a gel surface in dense groups, *swarms*. Surfactant helps in making a thin liquid film for the cell to move. (b) Twitching: bacteria expand, bind and retract pili to move towards the attachment point. (c) Gliding: in this example, focal adhesion points are moved on an helical line around the cell body (purple arrow). This traction results in the spinning and net motion of the bacteria. (d) Sliding: by growing and dividing, bacteria push their neighbours outwards.

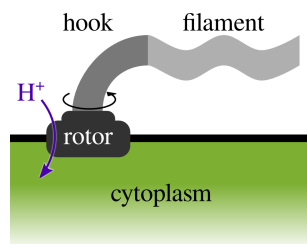


Figure 1.2: Structure of the flagella split into three main pieces: rotor, hook and filament.

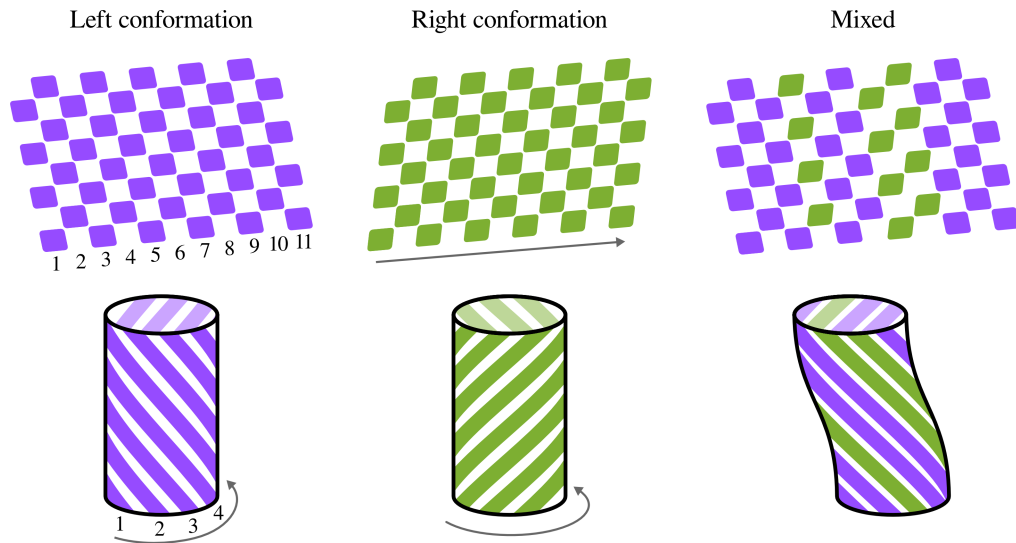


Figure 1.3: Filament macroscopic shape is determined by the combination of left (purple) and right (green) conformations. When all fibrils (numbered 1 to 11) take the same conformation, the filament forms a straight tube. In case of heterogeneous conformations, supercoiling generates a helical shape. Each rhombus represent a single flagellin protein.

Generally, all proteins on a given fibril have the same conformation. If all fibrils share the same conformation, the filament takes a straight shape. However if fibrils become heterogeneous, supercoiling of the filament modifies the macroscopic structure into a helical shape (figure 1.3). A total of twelve theoretical combinations of right and left conformations have been identified, each giving rise to a specific flagella geometry: helical pitch, radius, and handedness [57].

Some of the theoretical shapes have been observed experimentally on swimming *Escherichia coli*: normal, coiled, semi-coiled, curly [57, 58]. Notably, bacteria adapt the shape of their flagella depending on their swimming behaviour (as explained in the next subsection). For example, the “normal” conformation has been shown to be the most hydrodynamically efficient for self-propulsion [47] and turns out to be the one used for that purpose [58].

The spinning of a flagellum is actuated by a rotor embedded in the cell membrane [54]. This motor is a masterpiece of engineering, made of about thirteen different proteins (and twice as many are necessary for its assembly) [59]. It is driven by an influx of protons towards the inside of the cell (protons are then expelled by an active

pump placed in the membrane). Protons going through the rotor actuate its rotation, up to several hundreds Hertz, either clockwise (CW) or counterclockwise (CCW) [60, 61]. The exact details of how the flagella rotor works are still to be discovered.

The filament and the motor are finally attached to one another by a hook [54]. The hook is flexible in bending, such that the filament can point to either end or side of the bacteria, but rigid in twisting to properly transmit torque from the rotor to the filament [62].

## Flagella Expression

Cells do not always need to swim and have developed mechanisms to regulate the production of flagella [63, 64]. In biofilms for example, swimming bacteria can disrupt the complex organisation [65] and cells collectively prevent the formation of flagella [6]. Likewise, when bacteria are placed in a fresh nutritious medium, they switch to a growing state without flagella and form chains of partially divided cells. Once they have consumed most of the nutrients (at the end of the exponential phase), they revert to a swimming phenotype to seek another source of food [64, 66].

To precisely control the formation of flagella, all genes involved are placed under a unique master regulatory operon [54, 63, 64]. The gene expression is regulated depending on the external conditions but also monitors the number of flagella. Some bacterial species grow only one or two flagella [48]. Peritrichous bacteria like *B. subtilis* and *E. coli* instead use multiple flagella. *E. coli* has about ten rotors at a time, while *B. subtilis* can have up to thirty<sup>1</sup>. In peritrichous bacteria, flagella emanate from the entire body surface. Their distribution is homogeneous over the cell length and the distance between rotors is controlled such that, in *B. subtilis*, they are further away from one another than if randomly distributed [48].

## Swimming Behaviour

In order to propel themselves, bacteria simultaneously spin all flagella CCW (when looking from the flagella to the body) [67]. Flagella are in a *normal* conformation (left-handed) such that they exert a force expelling the fluid and pushing on the body.

<sup>1</sup>Not all rotors are associated with a functional flagellum, as the filament can be undeveloped. However more than half of them typically contribute to the swim [48, 63].

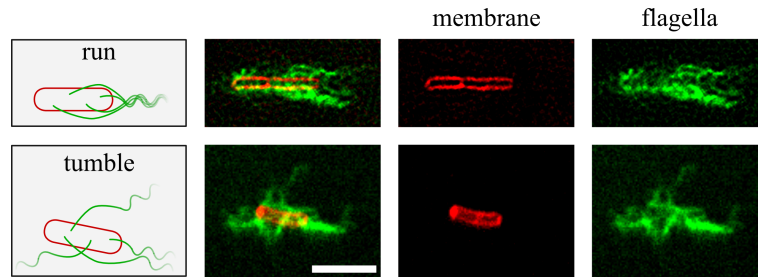


Figure 1.4: Bundling and unbundling of flagella during a run & tumble. Run: flagella emerge from the entire cell body and form, in the model, a tight bundle. In experiments I observed flagella to aggregate at the rear of the cell. Tumble: upon the reversal of some flagella rotors, filaments unbundle. This state was obtained experimentally by shining a blue light onto the sample cell. Scale bar:  $5\mu\text{m}$ . Membrane and flagella were labelled respectively with fluorophores FM4-64 (false coloured red) and Alexa Fluor 488 C5 Maleimide (false coloured green). Labelling and imaging methods are explained in full details in chapter 3.

Since rotors cover the entire cell body, flagella bundle at one end of the rod-like body in order to generate a net propelling force [58]. Bacteria do not have an intrinsic front or back and the bundle can form at either end. Some cells have even been observed to revert the bundle position after hitting a wall [68].

This bundle was first described in *E. coli* where all  $\sim 8$  flagella perfectly merge and spin as a single object [58]. The formation of this bundle has been shown to result from hydrodynamic interactions between each of the helical filaments [69, 70]. In the case of wild-type *B. subtilis* (strain 168), which I used in my experiments, even though flagella accumulate at one end, they do not form a tight bundle but rather a large cylindrical or conical aggregate (figure 1.4). This is probably due to the shape of cells, which are two to three times larger than *E. coli* and to the larger number of flagella, which physically limits the formation of the bundle [71].

This swimming behaviour results in a straight motion called a run and lasts about a second. In order to turn, bacteria revert the spinning direction of one or several rotors, thus disassembling the bundle [58, 67]. The filament conformation is also changed from a left-handed (*normal*) to a right-handed conformation (*semicoiled* and *curly I*) [67], such that the filament is still pushing on the cell body. Flagella point outward in different directions, randomly turning the cell. This step is called a tumble and only lasts a tenth of a second. A succession of runs and tumbles results in a

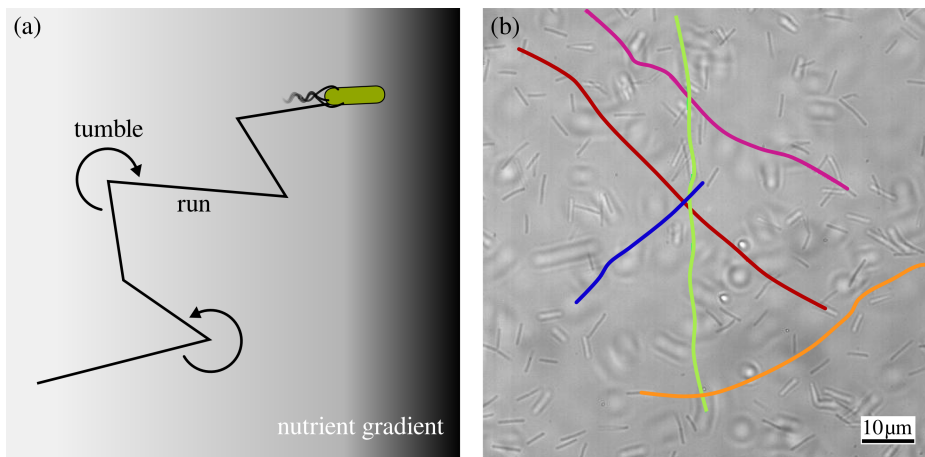


Figure 1.5: Trajectories of swimming bacteria. (a) Model of run and tumbles. Runs are longer when bacteria are swimming up a gradient of nutrients, resulting in a chemotactic behaviour. (b) Wild-type *B. subtilis* trajectories show an absence of tumbles. Tracking was done manually on bacteria in and out of the plane of focus.

random walk motion (figure 1.5a) [72]. Run & tumble has been described in several bacteria including *E. coli* and some *B. subtilis* strains [58, 67, 72, 73]. However I did not observe clear tumbles with the strain 168 of *B. subtilis* but rather smooth turns (figure 1.5b). *E. coli* has also been observed to lack tumbles when swimming close to surfaces [74].

Bacteria can regulate the frequency of tumbles in order to navigate in their environment. For example they are able to swim towards nutrient and oxygen sources [72, 73]. Since cells are too small to directly sense chemical gradients, they integrate the information over time instead: if the chemical concentration increases, i.e. if the bacterium is swimming towards the source, it will down regulate tumbles, and likewise shorten the run period when the concentration decreases [72]. This behaviour, called *chemotaxis*, allows bacteria to have net motion along chemical gradient (figure 1.5a).

### 1.2.3 Fluid Flows

Bacteria can only live in water and their motion is affected by flows, advecting and rotating them. Moreover while swimming, they generate specific fluid flows that can result in long-range interactions. These phenomena happen on very small scales (tens of microns) at low Reynolds number.

## Reynolds Number $Re$

The motion of an incompressible Newtonian fluid is governed by the Navier-Stokes equation,

$$\rho \left( \frac{\partial \mathbf{v}}{\partial t} + \mathbf{v} \cdot \nabla \mathbf{v} \right) = -\nabla p + \mu \nabla^2 \mathbf{v} + \mathbf{f}, \quad (1.1)$$

where  $\mathbf{v}$  is the fluid velocity,  $\rho$  its density,  $p$  its pressure,  $\mu$  its dynamic viscosity and  $\mathbf{f}$  any force acting on the fluid. This equation shows the balance between inertia (left-hand side of the equation) and viscosity ( $\mu \nabla^2 \mathbf{v}$ ). The Reynolds number  $Re$  measures the ratio between the two, such that

$$Re = \frac{\text{inertial forces}}{\text{viscous forces}} = \frac{\rho V L}{\mu}, \quad (1.2)$$

where  $V$  and  $L$  are typical velocity and length of the system. In the case of a *B. subtilis* in water,  $\rho = 10^3 \text{ kg/m}^3$ ;  $\mu \approx 10^{-3} \text{ Pa.s}$ ;  $V \sim 10 \mu\text{m/s}$ ;  $L \sim 1 \mu\text{m}$ , and

$$Re \sim 10^{-5} \ll 1. \quad (1.3)$$

Thus viscous forces largely dominate such that, if a bacteria stops swimming, it will keep on moving by inertia for less than an Ångström. Likewise, fluid flow around a microswimmer is only determined by instantaneous forces, and equation 1.1 can be reduced to the Stokes equation,

$$-\nabla p + \mu \nabla^2 \mathbf{v} + \mathbf{f} = 0, \quad (1.4)$$

with incompressibility,  $\nabla \cdot \mathbf{u} = 0$ .

The motion of bacteria simply results from the balance of forces. The self-propulsion speed for example can be computed from the force  $\mathbf{f}$  applied by the flagella on the fluid, and by the viscous drag [75], such that

$$\mathbf{f} + 6\pi\mu a \mathbf{v} = \mathbf{0}, \quad (1.5)$$

where  $a \sim 1 \mu\text{m}$  is the typical size of a bacterium.

## Fluid Flow Generated by a Bacterium

A swimming bacterium then applies two forces to the surrounding fluid; one arising from the spinning of the flagella, and one from viscous drag centred around the body. Each force can be approximated by a point *stokeslet* [76, 77].

A point force  $\mathbf{f} = f\mathbf{e}_x$  at  $\{x, y\} = \{0, 0\}$ , in a low  $Re$  fluid results in a disturbance of fluid (figure 1.6a),

$$\begin{cases} v_x = \frac{f}{8\pi\mu} \left( \frac{1}{r} + \frac{x^2}{r^3} \right), \\ v_y = \frac{f}{8\pi\mu} \frac{xy}{r^3}, \\ v_z = \frac{f}{8\pi\mu} \frac{xz}{r^3}, \end{cases} \quad (1.6)$$

where  $r^2 = x^2 + y^2 + z^2$  and  $\mathbf{v} = (v_x, v_y, v_z)$ .

In the case of a bacterium and many other microswimmers, the two forces are close (but not colocalised) and in opposite directions, generating a *stresslet*. The fluid flow around two point forces  $\mathbf{f}_1 = f\mathbf{e}_x$  at  $\{x, y\} = \{\delta x/2, 0\}$  and  $\mathbf{f}_2 = -f\mathbf{e}_x$  at  $\{x, y\} = \{-\delta x/2, 0\}$  (figure 1.6b) is given by

$$\begin{cases} v_x = \frac{D}{8\pi\mu} \left( -\frac{x}{r^3} + \frac{3x^3}{r^5} \right), \\ v_y = \frac{D}{8\pi\mu} \left( -\frac{y}{r^3} + \frac{3yx^2}{r^5} \right), \\ v_z = \frac{D}{8\pi\mu} \left( -\frac{z}{r^3} + \frac{3zx^2}{r^5} \right), \end{cases} \quad (1.7)$$

where  $D = \delta x \cdot f$  is the stresslet strength.

The fluid around a swimming *B. subtilis* has been predicted to move away at the front and back and towards the side of the cell (figure 1.6c). Microswimmers having this behaviour are called pushers [78]. The opposite, pullers, also exist if flagella are placed at the front of the cell. The green alga *Chlamydomonas* is a good example of such an arrangement, with two flagella pulling fluid at the front of the cell in a breast stroke motion (figure 1.6d) [79].

The fluid flows around *E. coli* has been experimentally measured using passive colloids as tracers. The experimental measurement matches the stresslet model, except in the near vicinity of the cell (figure 1.6c) [78]. In the case of *Chlamydomonas*,

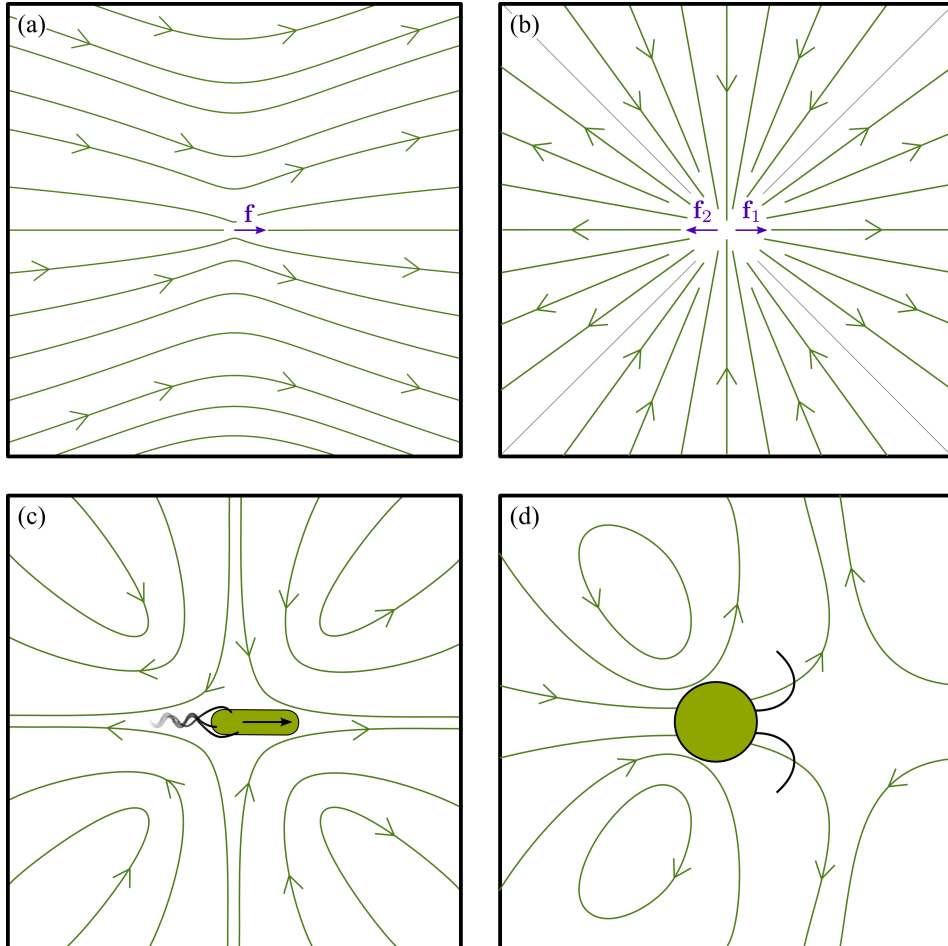


Figure 1.6: Fluid flows at low Reynolds number. (a) Streamlines around a point force. (b) Streamlines around a force doublet. (c) Streamlines around a swimming bacterium. (d) Streamlines around a *Chlamydomonas* cell.

fluid flows are more complex, as each of the two flagella applies its own force. However, in the far field of the cell, fluid flows are consistent with the puller model (figure 1.6d) [80].

### Transport of Bacteria by Fluid Flow

Similar to other micron-sized objects, bacteria can also be moved by external fluid flows. The contribution of fluid flows to the motion of a rod-like cell can be divided into two parts: advection and reorientation [75, 81].

The first term simply states that the cell is pushed along streamlines. The motion of the centre of mass  $\mathbf{X}$  of a single bacterium in fluid flow is then described by

$$\frac{d\mathbf{X}}{dt} = U\mathbf{P} + \mathbf{v}, \quad (1.8)$$

where  $U$  is the swimming speed,  $\mathbf{P}$  the cell orientation and  $\mathbf{v}$  the fluid flow at position  $\mathbf{X}$ .

The body of *B. subtilis* has a cylindrical shape, capped with half spheres. It is 4 to 8  $\mu\text{m}$  long and  $\approx 1 \mu\text{m}$  in diameter. A cell can be approximated as a prolate spheroid which is reoriented following Jeffery's equation [82]. When a swimming bacterium is placed in a shear flow, it exhibits Jeffery's orbits as theoretically predicted [83].

Moreover if the shear is not homogeneous, cells accumulate in high-shear regions [83]. This phenomenon can be simply understood: size of orbits is inversely proportional to the shear strength, resulting in a trapping effect where shear is the greater. When bacteria are placed in a channel with parabolic flow, this effect result in the accumulation of the cells close to surfaces [83].

### Long-range Hydrodynamic Interactions

When passive colloids are placed in a bath of microswimmers, they move by Brownian motion and advection by the fluid generated by the cells. This results in the enhanced diffusion of colloids [84, 85].

Likewise, the motion of bacteria is also affected by that of other swimmers. The combination of pusher disturbance, advection and reorientation can result in long-range hydrodynamic interactions [86].

In the case of two swimmers, this force is often negligible compared with self-propulsion and direct contact forces between swimmers [7, 78, 87, 88]. Yet when the bacterial concentration increases, the cumulated hydrodynamic interactions between multiple swimmers, could become significant and affect the suspension motion. This question is still controversial in the field of active matter [89, 90, 91] and will be considered in detail in chapter 3.

## 1.3 Dense Suspensions of Bacteria

When *B. subtilis* are grown in a liquid medium (rather than on agar plates), they can reach a maximum concentration of  $10^8$  cells/mL (volume fraction  $\sim 0.01\%$ , distance between swimmers  $\sim 10\mu\text{m}$ ). At such a density, the suspension is said to be dilute: the motion of one bacterium is weakly affected by that of others. If the concentration is further increased, either artificially or by growing cells on agar, interactions lead to the formation of collective motion, typical of active matter systems [30, 31, 32, 92, 93].

### 1.3.1 Collective Motion of Bacteria

Swimming bacteria are a common model to study active matter and their behaviour in large quasi-2D and 3D chambers has been extensively described<sup>1</sup>. A classical approach is to concentrate cells by centrifugation before injecting them into the setup [7, 92]. I present here an alternative method developed by Vasily Kantsler, former post-doc of the group, to study sperm cells (he prepared the PDMS chambers and I performed experiments with *B. subtilis*).

The setup consists of two main chambers, a central one in which cells are concentrated and a larger one around it, used as a reservoir of bacteria (figure 1.7a). They are connected by several radial and asymmetric channels, the walls of which are shaped as ratchets, as designed by Denissenko *et al.* [94]. When swimming along the walls, bacteria are reoriented to travel towards the central chamber (figure 1.7b).

<sup>1</sup>I call quasi-2D a chamber whose height is small enough for the bacterial motion to mostly happen in the plan of focus. In the case of *B. subtilis*, I used chambers 15 to 25  $\mu\text{m}$  in height. I also assume in both quasi-2D and 3D chambers that the medium and the suspension are homogeneous along the vertical direction.

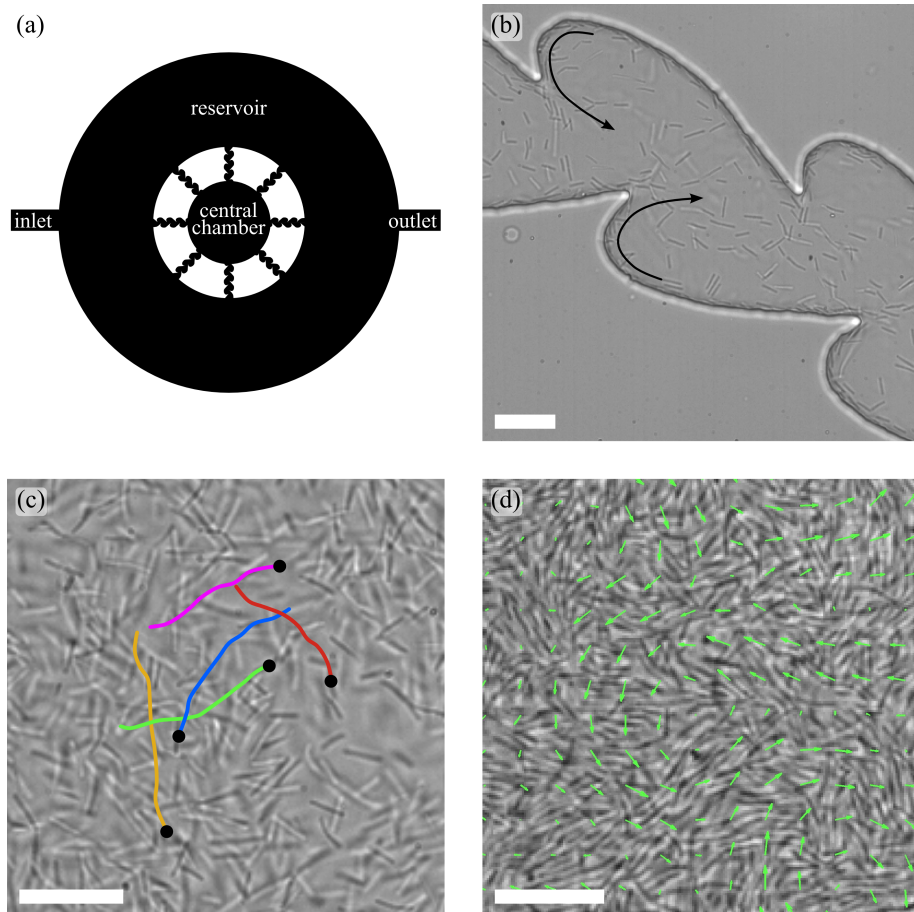


Figure 1.7: Collective behaviour arises in dense suspensions. (a) Sketch of the PDMS chamber used to concentrate bacteria. Cells are injected through the inlet and swim with a net migration from the reservoir to the central chamber. The reservoir can be mm-large while the central chamber as a typical diameter of  $100\mu\text{m}$ . (b) Ratchet-like wall reorient the bacteria to swim towards the central chamber. (c) Motion in the central chamber at the beginning of the experiment. Trajectories of dilute bacteria are weakly correlated. Lines: cell trajectories, manually tracked. Circle: initial position. (d) Motion after 75 minutes. The dense suspension forms large patterns like swirls and jets. Arrows: bacterial flow measured by PIV (see Methods in chapter 2, here obtained using PIVLab [95]). Scale bars:  $20\mu\text{m}$ .

## Effect of the Increasing Concentration

The experiments run over a few hours, starting with an homogeneous dilute suspension. Migration of the bacteria towards the central chamber results in a progressive increase of the concentration, which allows us to observe the emergence of collective motion.

At low density, bacteria interact weakly and mainly follow single-cell trajectories (figure 1.7c). The cell concentration then slowly increases such that after 75 minutes, collective motion appears. Bacteria frequently come into contact with one another. Since they are rod-shaped, they locally align, akin to nematic liquid crystals. The combination of self-propulsion, steric and hydrodynamic interactions then results in collective motion of the suspension. This motion is said to be quasi-turbulent as it forms large scale patterns such as swirls and jets, stable for only a fraction of a second [7, 30, 31, 32, 92, 93, 96]. The length scale of these patterns is on the order of tens of  $\mu\text{m}$  (the diameter of a swirl is typically  $\sim 70\mu\text{m}$ ), an order of magnitude larger than bacteria (*B. subtilis* are 4 to  $8\mu\text{m}$  long).

If the bacterial concentration is further increased, cells enter a jammed state where the density is too large for them to move [7]. I did not observe this state in this experiment.

## Cell Concentration

Different methods have been used to measure cell concentration: direct counting, optical density or plates counting [32, 88]. I did not find any method that was precise and reproducible enough. By measuring the length and number of individual cells in shallow chambers (1 and  $2\mu\text{m}$  in height), I evaluated the volume fraction between 5 and 20% ( $\sim 1$  to  $4 \cdot 10^{10}$  cells/mL). This measure only takes into account the body of the bacteria. Yet flagella which are extremely thin, can extend over  $10\mu\text{m}$  around the body, thus yielding a much larger effective volume fraction. Similar values have been given in previous publications [88].

## Pattern Length Scale

A classical approach to quantitatively study the bacterial flow is to estimate its typical length scales. Two measures have been regularly used, the size of the vortices and the

correlation length. The former is usually 50 to 90  $\mu\text{m}$  in diameter and can depend on the chamber's height (quasi-2D chambers have smaller swirl diameter [7, 96]).

The latter is computed from the two-points spatial correlation. It indicates over which distance the suspension orientation is conserved. As the cell concentration increases, collective motion appears and so grows the persistence length [31, 32]. These questions are discussed in more detail in chapter 2, section 3.

## Oxygen Concentration

Unlike *E. coli*, *B. subtilis* need oxygen to swim. A good way to control the velocity of the suspension is then to change oxygen concentration. Sokolov *et al.* have shown that the mean speed of the dense suspension scales almost linearly with the oxygen concentration. Moreover, the correlation length quickly increases with the oxygen, before reaching a plateau value for  $[O_2] > 0.1 \text{ mM}$  and persistence length  $\approx 40 \mu\text{m}$  [93].

Likewise Dunkel *et al.*, without measuring the oxygen concentration, have characterised the turbulence of the suspension by first measuring the local vorticity  $\omega = \partial_x u_y - \partial_y u_x$ , where  $\mathbf{u}$  is the bacterial flow velocity. They then estimated the enstrophy, the energy associated with the vorticity, defined as  $\Omega = \langle \omega^2/2 \rangle$ . The enstrophy is used to quantify the turbulence of the suspension motion. They then compared  $\Omega$  with the kinetic energy  $E = \langle \mathbf{u}^2/2 \rangle$  and found that the enstrophy scales linearly with the energy:  $\Omega = E/\Lambda^2$  where  $\Lambda \approx 24 \mu\text{m}$  compares to a quarter of a typical swirl diameter [96].

Equations of motion at low  $Re$  are all linear, which explains this behaviour: decreasing the oxygen concentration reduces the swimmer speed and overall motion but does not affect the pattern formation otherwise.

## Collective Behaviour in Other Chambers

The motion in quasi-2D and 3D chambers is quite similar, except for the length scales, which are larger in the latter. Other setups have been considered. In particular drops and freely standing films can give rise to convection patterns.

I have only presented so far chambers that were homogeneous in bacteria and chemicals in the medium. When a liquid/air interface is added, oxygen that is consumed by the cells, can diffuse into the medium. This results in the formation of a

gradient of oxygen concentration, low in the bulk where it is consumed and large at the interface where it diffuses. Microswimmers, by chemotaxis, accumulate in regions of high oxygen concentration. Moreover bacteria are slightly denser than water, giving rise to a Rayleigh-Taylor instability. This motion leads to the formation of bioconvection patterns on the scales of several millimetres [92, 97].

In the rest of this thesis, I only use solid or liquid interfaces and try to avoid as much as possible gradients of oxygen in the chamber. I also limit the height of the chamber to less than  $30\mu\text{m}$  (quasi-2D chamber) to ensure that most of the bacterial flow happens in the plane of focus (except when otherwise stated).

### 1.3.2 Modelling Active Matter

The field of active matter is dominated by theoretical papers. Models often quest for the simplest unified theory that can reproduce the behaviour of many if not all active systems.

#### Vicsek and Toner-Tu Models

Vicsek and Toner-Tu models are two facets of the same ordering mechanism, which only assumes that self-propelled particles reorient themselves along the local mean direction [98].

Vicsek *et al.* first proposed a simulation method in which birds, locusts or bacteria are represented as a set of particles, moving at constant speed and whose orientation at each time step is set as the average of nearby particles [99].

Toner and Tu proposed a continuum version for this model [100]. The motion of particles is only represented by the mean local velocity  $\mathbf{u}$ , which follows the set of equations:

$$\begin{aligned} \frac{\partial \mathbf{u}}{\partial t} + (\mathbf{u} \cdot \nabla) \mathbf{u} = & \alpha \mathbf{u} - \beta |\mathbf{u}|^2 \mathbf{u} - \nabla P \\ & + D_L \nabla (\nabla \cdot \mathbf{u}) + D_1 \nabla^2 \mathbf{u} + D_2 (\mathbf{u} \cdot \nabla)^2 \mathbf{u} + \mathbf{f}, \end{aligned} \quad (1.9)$$

$$P = \sum_{n=0}^{\infty} \sigma_n (\rho - \rho_0)^n, \quad (1.10)$$

and

$$\frac{\partial \rho}{\partial t} + \nabla \cdot (\mathbf{u}\rho) = 0. \quad (1.11)$$

Equation 1.9 is designed as a Navier-Stokes equation with added terms to account for the self-propulsion and collective behaviour of the suspension. The left-hand side describes advection at swimming speed  $\mathbf{u}$ .  $\alpha$  and  $\beta$  are two positive terms representing self-propulsion, respectively increasing and decreasing  $\mathbf{u}$ , such that in a mean field approach, swimmers move at constant speed  $\sqrt{\alpha/\beta}$ .  $D_{L,1,2}$  are constants that represent the diffusivity of  $\mathbf{u}$  (or likewise the viscosity of the active fluid).  $D_{L,1,2}$  are taken positive such that the velocity becomes uniform, representing the fact that swimmers align their velocity with neighbours. If no noise  $\mathbf{f}$  is included, this set of equation result in all swimmers moving in a common direction at constant speed  $\sqrt{\alpha/\beta}$ .

Finally, swimmers repel each other by steric interactions, such that the local concentration must be finite. This effect is taken into account by the effective pressure  $P$  which depends on the cell density  $\rho$ , the mean density being conserved by equation 1.11. In equation 1.10,  $\sigma_n$  are positive constants and  $\rho_0$  represent the mean density.

Both models give rise to various collective behaviours depending on the alignment strength, noise and particle density [98]. The most common patterns are as follows [99, 101]:

**Disordered** At low alignment strength or high noise, each particle moves independently of its neighbours (in continuum models,  $\mathbf{u}$  has a short spacial correlation).

**Swarms** At moderate concentration, particles cluster into dense groups. Each cluster moves independently of others, but particles inside a single cluster share the same orientation.

**Travelling bands** Particles form dense strips. Particles are usually oriented perpendicular to the strip length.

**Uniform** The density is rather homogeneous and particles travel in a common direction.

These models are able to reproduce some behaviours observed in nature, from schools of fish, locust swarms, and bacteria in agar plates, but not the quasi-turbulent motion described above.

## Meso-scale Turbulence Model

With this limitation in mind, Wensink *et al.*<sup>1</sup> have proposed a variation of Toner-Tu model to generate quasi-turbulence [7, 96]. The bacterial suspension velocity  $\mathbf{u}$  follows the dynamics

$$\begin{aligned} \left( \frac{\partial}{\partial t} + \lambda_0 \mathbf{u} \cdot \nabla \right) \mathbf{u} = & \alpha \mathbf{u} - \beta |\mathbf{u}|^2 \mathbf{u} - \nabla P + \lambda_1 \nabla \mathbf{u}^2 \\ & + \Gamma_0 \nabla^2 \mathbf{u} + \Gamma_2 (\nabla^2)^2 \mathbf{u}, \end{aligned} \quad (1.12)$$

and

$$\nabla \cdot \mathbf{u} = 0. \quad (1.13)$$

As in equation 1.9, the suspension is set into motion by terms  $\alpha$  and  $\beta$ , with typical velocity  $\sqrt{\alpha/\beta}$ . The pressure  $P$  ensures the fluid incompressibility (equation 1.13). Here,  $\lambda_0$  can be different from 1 which, along with  $\lambda_1$ , account for hydrodynamic interactions between swimmers [98].

But the turbulent behaviour relies on the two last terms  $\Gamma_0$  and  $\Gamma_2$ .  $\Gamma_0$  was already introduced in Toner-Tu model, noted  $D_1$ . However, unlike in equation 1.9,  $\Gamma_0$  can here take positive or negative values. In the first case, it has the same effect as a diffusion or viscosity term, making the velocity  $\mathbf{u}$  uniform over the domain. If instead  $\Gamma_0 < 0$  any disturbance in the velocity field becomes unstable, generating turbulence. This effect is dampened by  $\Gamma_2$  (as would  $\beta$  for the velocity), resulting in quasi-turbulent patterns of typical length scale  $2\pi \sqrt{\frac{\Gamma_2}{-\Gamma_0}}$  [102].

This model was compared to experiments in quasi-2D and 3D chambers by measuring the velocity and vorticity  $\boldsymbol{\omega} = \nabla \times \mathbf{u}$  [7, 96]. Statistics and spacial distribution of the two measures are comparable in experiments and in simulations.

This model could then be used to predict the suspension self-organisation under different conditions, yet its aim is only to give a minimal description of turbulent motion in active matter and thus presents some limitations. First it only represents microswimmers through the average velocity  $\mathbf{u}$ . Two other quantities could be important to fully understand bacterial motion: their orientation and the fluid flow  $\mathbf{v}$ . Moreover, the model is only phenomenological, the macroscopic flow patterns are reproduced but no insights into the physical interactions is gained. It is then unlikely to help in

<sup>1</sup>Jörn Dunkel, a post-doc in Ray Goldstein's group at that time and now an assistant professor at MIT, and Ray Goldstein contributed to this model and to this thesis.

understanding the microscopic phenomena driving bacterial self-organisation.

## **Q-tensor**

Toner-Tu and the meso-scale turbulence models reproduce active matter starting from the macroscopic behaviour, both assume some alignment mechanism and in the latter, quasi-turbulence. An alternative approach is to start from the physical interactions and try to derive the suspension motion [103, 104, 105].

The Q-tensor method was imported from nematic liquid crystal theories [106], expanding it to include self-propulsion and long-range active hydrodynamic interactions [104, 107]. The Q-tensor represents the distribution of particle orientation. At a given position, unlike in the two previous models, not all particles are aligned in the same direction. To model fluid flows, the stresslet approximation is used. As described above, particles can have a pusher (e.g. bacteria, cytoskeleton extracts) or puller behaviour (e.g. *Chlamydomonas*). Different suspension patterns have been predicted depending on this fluid disturbance [108].

The active nematic is the class of active matter modelled by Q-tensor theories and can be simply understood as a nematic liquid crystal whose elements are self-propelled. The archetype probably corresponds to extracts of microtubules set into motion by kinesin motors: long thin filaments locally behave like liquid crystals but sliding powered by motors generate turbulent flows characterised by  $+\frac{1}{2}$  and  $-\frac{1}{2}$  defects [35, 36].

This approach may appear as the most appropriate to model bacterial suspensions. However, a crucial limitation can come from the size of bacteria relative to that of the suspension flows: a coarse-grained approach requires particles (bacteria) to be small compared to the simulation grid. Yet this condition is not always met as I will show in chapter 3.

## **Particle-based Simulations**

A final approach is to directly model the motion of individual particles (as in the Vicsek model [99]) and the various interactions between them. The difficulty in these simulations is not to write the governing equations but rather to make appropriate approximations so that computations run in a humanly acceptable time.

A widespread approximation is to look at the motion in a 2D domain, significantly

reducing interactions and the total number of particles in a given domain size. A main concern is that, if steric interactions are included, particles cannot swim over one another, as they do experimentally in 3D or even in quasi-2D chambers. Yet simulations do not seem to suffer significantly from this approximation (chapter 3). Experimentally, the main difference between truly 2D and quasi-2D or 3D chambers appears in the hydrodynamic interactions, which varies in strength and flow pattern. Yet all these differences do not rely on the domain itself but on the governing equations and can easily be implemented [109, 110, 111].

Another recurring idea is to neglect fluid flows, supported by the fact that “measurements [78] ... suggest that hydrodynamic far-field interactions are negligible for bacterial reorientation” [7]. Moreover, models with steric interactions only are able to reproduce the quasi-turbulent state. Particle-based simulations have managed to reproduce dense suspension behaviours: disordered, swarming, turbulent, jammed; and to predict several others, including lanes. These states depend on the bacterial density and aspect ratio [7, 90].

However these simulations do not prove that fluid flows are actually negligible in dense suspensions. Indeed, models that only include hydrodynamic interactions, rather than steric repulsion, also show the suspension motion to be unstable and result in a quasi-turbulent behaviour [89, 91, 109].

Only few articles have considered full systems with both direct steric and long-range interactions [90, 110]. The question of fluid flows, their significance and the correct way to model them is still under debate. In chapter 3, I will discuss these issues and present results supporting hydrodynamics as a key ingredient for bacterial self-organisation.

## 1.4 Bacteria under Confinement

I have mostly presented so far results in 3D or quasi-2D chambers (periodic domains in simulations). Most experiments that look at dense bacterial suspensions have actually been performed in large homogeneous chambers<sup>1</sup>.

And yet bacteria and other active systems can regularly encounter interfaces and

<sup>1</sup>A notable exception is that of drop and freely standing films presented above [92, 97].

confinement. *B. subtilis* for example is a soil bacterium and its motion is most certainly affected by sand particles and liquid/air interfaces. Likewise, bacteria infecting eukaryotic cells are trapped into an environment about ten fold their size [112].

### **1.4.1 Effect of Interfaces on the Swimming of Single Microswimmers**

Even though very few papers have considered the effect of interfaces on dense bacterial suspensions, the case of dilute bacteria has been well documented. Here, I consider interfaces, solid or liquid, that only play a mechanical role but do not modify the chemical environment (oxygen cannot diffuse through the interface for example).

#### **Accumulation at Interfaces**

When swimming bacteria are placed in a large chamber with solid walls, they quickly accumulate at interfaces, emptying from the centre of the chamber [113, 114]. This behaviour is not due to sedimentation as bacteria accumulate at top walls as well. Two effects have been proposed to explain this attraction: long-range hydrodynamics and direct steric interactions.

When a bacterium swims, it pushes fluid away from its front and back and towards its side. If a cell is parallel to a wall, fluid flows result in a net force attracting the swimmer to the interface [78, 113]. However this argument has been debated as the force may be too weak compared to that of swimming or Brownian motion [115, 116].

Instead, the shape of the microswimmer could explain the trapping mechanism: when considering the full volume explored by flagella, the front of the swimmer is thinner than its back. When swimming at an interface, steric interactions then make the cell point slightly towards the wall. The same argument holds for sperm cells [117] and can explain why the green alga *Chlamydomona* escapes from walls: with flagella at the front, where the triangular shape is reversed [116].

#### **Swimming Behaviour at an Interface**

Once a bacterium is trapped at an interface, its motion changes. First of all, Molaei *et al.* have observed that *E. coli* cells reduce their tumbling rate by 50% and move in

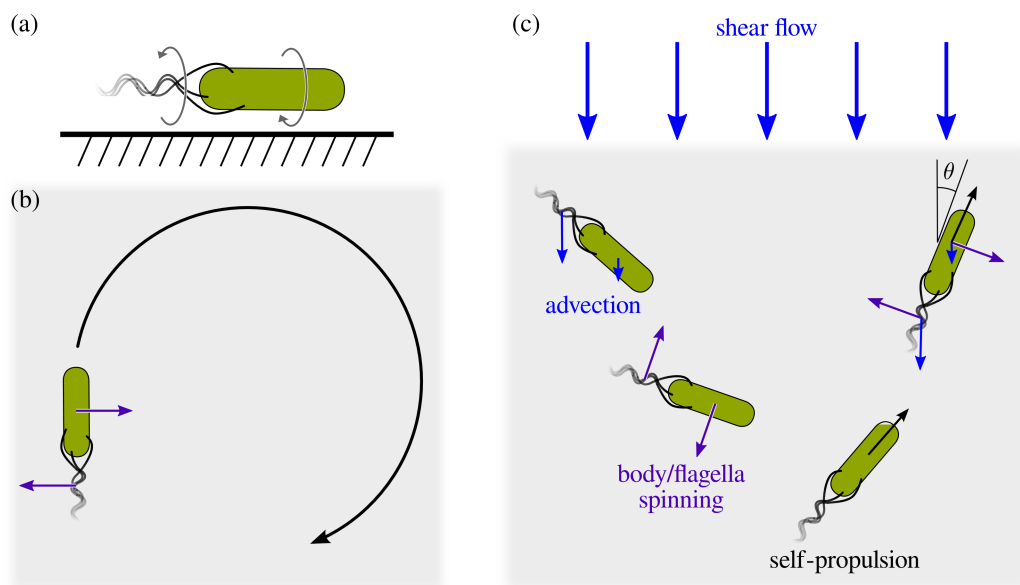


Figure 1.8: Effect of surfaces and shear flow on the swimming of *B. subtilis*. (a) Body and flagella spin in opposite directions, (b) creating a lubricated friction between the swimmer and the surface, of opposite direction at the head and flagella (small arrows). These two forces generate a torque in the vertical direction thus make the bacteria follow a circular trajectory. (c) When a flow is applied, cells are reoriented by the fluid flow (blue), friction with the surface (purple) and move by self-propulsion (black). Balance between forces result in the bacterium swimming against the flow, at an angle  $\theta$ .

smoother trajectories [74]. Hydrodynamic forces that lead to unbundling are thought to be dampened by the near surface.

Furthermore, when swimming, the body of the bacterium spins in opposite direction to its flagella, ensuring that the microswimmer is torque-free along its swimming direction (figure 1.8a). The rotation of the body next to an interface generates a net force. The same effect applies to the flagella but in opposite direction. This results in a net torque orthogonal to the interface, the sign of which depends on the interface type, free-shear or no-slip [118]. In the case of a solid wall, bacteria then have CW circular trajectories, with a radius of curvature typically tens of  $\mu\text{m}$  in the case of *E. coli* (figure 1.8b) [119, 120].

### Swimming Against a Fluid Flow

When a fluid flow is then applied to the chamber, it reorients bacteria, setting their swimming direction [121].

Both the body and flagella are subject to advection by the fluid and friction in the vicinity of the surface. The difference in shape between flagella and body is such that the latter is more inclined to advection, acting like a tail to reorient the cell against the fluid.

As a secondary effect, the torque that leads to circular trajectories in the absence of fluid flow still applies here. The exact angle between the swimmer and the fluid flow results from the balance of this torque and that of reorientation against the flow. Bacteria thus swim against the current at a fixed angle  $\theta$ , as shown on figure 1.8c [122, 123, 124].

## 1.4.2 Active Matter under Confinement

Confinement has already been shown to have a strong effect on the self organisation of some active systems. In chapters 2 and 3 I will compare and discuss in full detail previous experiments with results I obtained. Here I briefly give examples of confining geometries used experimentally and found in nature.

**Circular confinement** Probably the simplest geometry, active matter is placed in a flat (2D or quasi-2D) cylinder. Examples range from bristle-bots [39, 40] to single

or multiple eukaryotic cells [125, 126]. Under certain conditions (confinement size, shape of the boundary, concentration...), the self-propellers coordinate their direction of motion to form a single vortex.

**Racetrack** A racetrack is a periodic channel. This geometry has been used to study marching locusts in the lab [29] and rolling colloids [127]. As for circular confinement, interfaces promote the alignment of the particles such that all objects or organisms move in a common direction. This motion is usually stable and can take the form of a travelling wave, as seen in rolling colloids [127].

**Sphere** Changing the confinement from a 2D to a 3D chamber can have dramatic effects. Indeed, while for example racetracks have a preferred direction along the channel length, spheres are symmetric along all three coordinate axis. A notable example is that of microtubules and kinesin motors in vesicles. Filaments aggregate at the lipid bilayer and start flowing collectively. Their motion sets the vesicle into motion, rolling over the substrate, but the direction of motion is unstable due to the symmetry, resulting in the random walk of the vesicle [35].

### 1.4.3 Thesis Outlook

The effect of confinement on the self-organisation of dense bacterial suspensions has been mostly unexplored. During my PhD, I have studied, mainly experimentally, how *B. subtilis* behaviour changes with confinement geometry. The aim of this project was not only to discover new active phenomena under confinement, but also to use these setups to better understand general properties and behaviours of bacterial suspensions.

Chapter 2 presents experimental results in two main setups: flattened drops and racetracks. I quantitatively measured the flow patterns with a strong emphasis on the role of chamber geometry: drop diameter, racetrack width, chamber height. I also found bacteria at the interface to move against the bulk circulation. This phenomenon has not been reported in earlier experiments or models and was initially not understood.

Chapter 3 introduces a new simulation method developed in collaboration with Enkelaida Lushi, the aim of which was to fully describe interactions between swimmers and with interfaces. An important point was to understand the role (if any) played by hydrodynamic interactions. We prove that under these confinements, the suspen-

sion motion cannot be understood without considering fluid flows. Results were also confirmed with a new experimental method that I developed, enabling us to observe simultaneously the orientation and the direction of motion of individual bacteria.

Chapter 4 focuses on a new confining geometry: a lattice of flat circular cavities. Each cavity is similar to a flattened drop, except for junctions between them, allowing for interactions between vortices. While the direction of circulation in an isolated vortex is random, a chain, square or triangular lattice can spontaneously turns itself into an ordered array. I observed two critical patterns: ferromagnetic, when all vortices share the same direction, and antiferromagnetic, when each vortices spins in opposite direction to its neighbours. Finally, in collaboration with Francis Woodhouse and Jörn Dunkel, I analysed this phenomenon using an Ising model in a decorated lattice. In particular I obtained directly from experimental measurements simplified parameters of the system Hamiltonian.

## Chapter 2

# Bacteria under circular and linear confinement

### 2.1 Introduction

In the 1950's, Yoshio Yotsuyanagi took 10cm long internodal cells from the algae *Nitella* and *Chara*, and manually isolated the content such that part of the cytoplasm would get encapsulated into vesicles [128, 129]. He then observed that the content of these vesicles, while being subject to Brownian motion, could also actively move, spontaneously creating protuberances, pulsations and sometimes circulation. This motion is most probably due to myosin motors carrying smaller vesicles along actin filament bundles, a mechanism used to generate cytoplasmic streaming in live cells [130]. However, how such an active fluid could self-organise was not understood.

Sixty years later, Francis Woodhouse, a PhD student in Ray Goldstein's group at that time and currently a research assistant professor at the University of Western Australia, reproduced this self-organisation using a continuum model [131]. He showed in particular that the motion of motors on actin filaments generate a stresslet disturbance. I also managed to experimentally reproduce Yotsuyanagi observations (figure 2.1) but this system presented several challenges to work with: the content of the cytoplasm (proteins, vesicles...) is not well characterised, it is difficult to visualise constituents (actin filaments, motors), and the myosin motors are very unstable once purified.

Instead, swimming bacteria such as *B. subtilis* present many advantages: they are

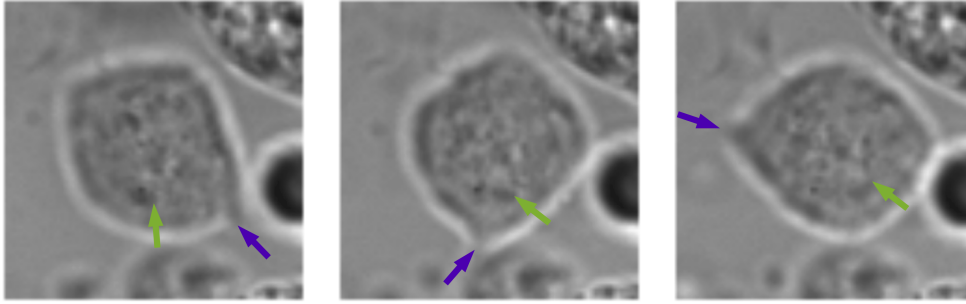


Figure 2.1: Rotating vesicle of *Chara* extract, prepared by manually squeezing out the cytoplasm of an internodal cell. The extract has not been mixed into any buffer, the surrounding medium is the vacuole content. The vesicle edge takes a polygonal shape with a protrusion (purple arrow) which rotates CW, while the bulk circulates CCW (green arrow). Diameter:  $15\mu\text{m}$ . Timescale  $\approx 1\text{ s}$ .

a model system for active matter, better characterised than *Chara* cells, are easy to grow and image, and the numerous mutants can be useful to understand the population behaviour. Even though *Chara* cytoplasmic streaming and bacterial swimming have no common biological basis, they both generate a stresslet disturbance in the surrounding fluid and thus Woodhouse's simulations can still be relevant for the study of bacterial circulation.

In large chambers, dense bacterial suspensions self-organise into two main turbulent patterns: vortices and jets. In this chapter, I describe how each flow pattern can be stabilised by confinement in a specific microchamber. The last section presents an opening to more complex confining topologies.

I first studied dense bacterial suspensions inside flattened drops, similar in shape to *Chara* vesicles, and found that the cells would spontaneously self-assemble into a single spiral vortex state. Bacteria also form a boundary layer moving in the opposite direction to the bulk, a finding which was not predicted by Woodhouse's model. I then injected the dense suspension into periodic channels, which stabilise the bacterial motion into a persistent directed stream.

I quantitatively studied the bacterial dynamics in these two systems, measuring in particular the flow pattern dependence on the chamber size. Confinement not only stabilised and controlled the suspension dynamics, but also gave us valuable information on bacterial self-organisation and raised questions on the mechanism driving bacterial

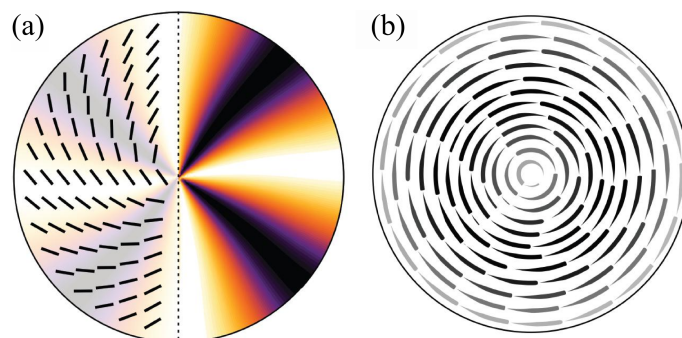


Figure 2.2: Numerical results of *Chara*-like active matter confined into a circular chamber. (a) nematic order orientation. Dark areas indicate vertical and horizontal orientation, brighter ones, diagonal orientation. (b) spontaneously circulation streamlines. Darker lines reflect faster motion. Adapted from [131]

motion. These questions will be studied in details in the next chapter.

The last section of this chapter presents how bacteria self-organise in an 8-shaped channel and shows that the bacterial motion can be finely controlled by the exact geometry of the chamber.

## 2.2 Flattened drops

Dense bacterial suspensions have been extensively studied in unconfined 3D or 2D chambers. My first challenge was to design experimental chambers that could enclose the suspension into a limited volume. Inspired by algal extract vesicles, I first considered flattened cylinders.

### 2.2.1 Protocol

Dense bacterial suspensions have been studied for many years [7, 30, 31, 32, 92, 93, 96] and there are now standardised protocols to grow cells, image them and analyse their motion. A common approach to make microchambers is to use microfluidic channels made of Polydimethylsiloxane (PDMS). However, this technique is not appropriate to form flattened cylinders. An issue I encountered is that the injection channels (inlets) would affect the motion inside the small cavity. Instead I modified a method used to study *Xenopus* frog egg extract in an oil emulsion [132, 133].

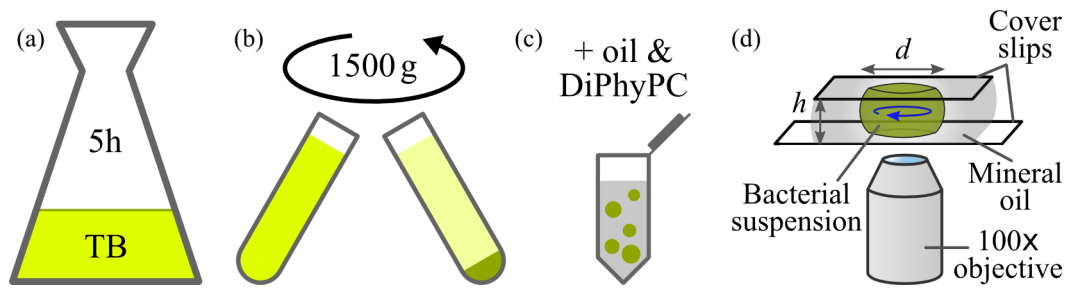


Figure 2.3: Protocol. (a) Bacteria were grown in TB and (b) concentrated 200 fold by centrifugation. (c) The pellet was then mixed into mineral oil to form an emulsion, (d) placed between two hydrophobic coverslips. Chamber height  $h$  was typically  $25\ \mu\text{m}$  and drop diameter  $d$ ,  $15 - 100\ \mu\text{m}$ .

### Bacterial preparation

Wild type *Bacillus subtilis* (strain 168) were grown following a standard method [7, 32]. A stock of bacteria was maintained in a  $-80^\circ\text{C}$  freezer, mixed with 50% glycerol. A few days prior to the experiment, a small amount was transferred on an agar plate using a sterile inoculating loop. Bacteria were grown in a growth chamber at  $35^\circ\text{C}$  for 12 to 24 hours. A day before the experiment, a monoclonal colony of bacteria was transferred to 20 mL of liquid medium and left to grow overnight at  $35^\circ\text{C}$  on a shaker to allow for a better mixing of the suspension and higher concentration of oxygen thus increasing the growth rate.  $100\ \mu\text{L}$  was then transferred to 20 mL of fresh medium and allowed to grow for 5 to 6 hours before being harvested for the experiment.

As a nutritious medium, I used Terrific Broth (TB, Sigma) which contains 12 g/L of tryptone, 24 g/L of yeast extract, 8 mL/L of glycerol, 9.4 g/L of  $\text{K}_2\text{HPO}_4$  and 2.2 g/L of  $\text{KH}_2\text{PO}_4$ . The medium is more concentrated than the widely used Luria Broth which only contains 10 g/L of tryptone, 5 g/L of yeast extract and no glycerol. *B. subtilis* can then reach higher concentration than in LB.

Bacteria adapt their phenotype depending on external conditions. In particular they only start swimming when the nutrient concentration is sufficiently low [64]. After 5 to 6 hours of incubation, cells reached the end of the exponential phase, at which stage the vast majority is swimming. Nishihara *et al.* quantified this effect and observed up to 80% of cells swimming [66]. Prior to any experiment, I quickly confirmed the suspension motility. Under a  $40\times$  objective, I would find less than ten immotile cells in a field of view containing around a hundred swimmers.

I then harvested 10 mL of the suspension. To further increase the cell density, the suspension was centrifuged (1500 g, 10 min) and the pellet was directly used. I tried different methods to estimate the density with difficulty to obtain an accurate measure. By measuring the length and number of individual cells in a shallow chamber (1 and 2  $\mu\text{m}$  in height), I evaluated the volume fraction between 5 and 20%.

### **Drop formation**

The dense bacterial suspension was then mixed into 4 times the volume of mineral oil (Sigma) with added diphytanoyl phosphatidylcholine (10 mg/mL, DiPhyPC, Avanti). By gentle pipetting, the mixture forms an emulsion with drops filled with bacteria, 1  $\mu\text{m}$  to 1 mm in diameter. The lipid DiPhyPC reduced the coalescence of drops. Bacteria, which only live in aqueous medium, did not swim into the oil phase.

I left the largest drops settle at the bottom of the tube and pipetted 10  $\mu\text{L}$  of the emulsion over a 55  $\times$  22 mm coverslip. A second coverslip, 22  $\times$  22 mm, was placed over the emulsion which then spread by surface tension to the edge of the top coverslip. No spacer or seal was used and the height of the chamber was simply set by the volume of the emulsion and the surface area of the smaller coverslip. This method has the advantage to prevent evaporation and large macroscopic flow.

Additionally glass surfaces were made hydrophobic by a silane treatment before being used: 5  $\mu\text{L}$  of Dichlorodimethylsilane (Sigma) were vaporised in a vacuum chamber, alongside glass coverslips. The hydrophobicity modifies the shape of the drops, such that the radius at the top and bottom of the chamber was smaller than in the centre (figure 2.3d).

### **Imaging**

The suspension quickly self-organises and I solely imaged the steady state. Two seconds long movies were acquired on a high-speed camera (Photron Fastcam) at 125 fps, with bright field illumination, through a 100 $\times$  oil-immersion objective, on an inverted microscope (Zeiss Axio Observer Z1). I focused the focal plane in the centre of the chamber to image the largest cross-section and avoid optical distortion from the water/oil interface. Yet, the suspension's motion did not depend on the height except for the slower velocity close to the coverslips. The dense suspension quickly consumed

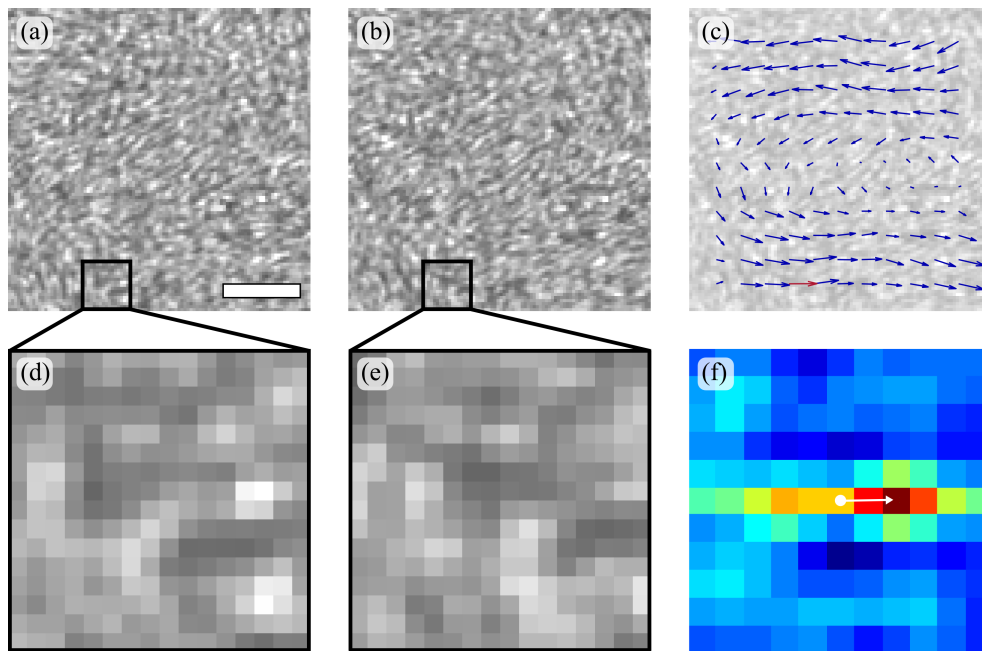


Figure 2.4: Measure of the suspension velocity using a standard PIV method. (a,b) Two images of the suspension, taken at  $1/60$ s interval are compared. Scale bar:  $20\mu\text{m}$ . (c) PIV flow field between the two images. For clarity, the arrow size is much larger than the displacement between the two frames. The red arrow indicates the velocity obtained by comparing subwindows (d) and (e). (f) Cross correlation  $C_{\text{PIV}}(\mathbf{s})$  between (d) and (e). White circle: origin,  $\mathbf{s} = 0$ . Arrow: estimated displacement.  $C_{\text{PIV}}$  is colour coded with dark red for the largest value and dark blue for the smallest

the oxygen, and even though oxygen diffuses from the oil phase, bacteria stopped swimming in less than 10 minutes.

### Flow measurement

To measure the bacterial flow, I used a standard particle image velocimetry (PIV) method. PIV was initially developed to measure fluid flows through the motion of tracer colloids. Here I did not add colloids to bacteria but simply used the speckle made by the dense suspension (figure 2.4). I measured the bacterial flow, not the fluid flow.

Images were first divided into subwindows, typically  $8 \times 8$  pixels large ( $2 \times 2\mu\text{m}$ ), with 50% overlap (i.e. centres are placed every 4 pixels). Each subwindow was then

cross-correlated with itself, on the next frame, at time  $t + dt$ ,

$$C_{\text{PIV}}(\mathbf{s}, t) = \sum_{\mathbf{n}} I(\mathbf{n}, t) \cdot I(\mathbf{n} + \mathbf{s}, t + dt), \quad (2.1)$$

where  $\mathbf{n} = \{n_x, n_y\}$  are the pixel positions inside the subwindow, and  $I$  is the pixel intensity. The maximum of  $C_{\text{PIV}}$  at  $\mathbf{s}^{\text{max}}$  gives a first approximation to the average displacement  $\tilde{\mathbf{s}} = \mathbf{s}^{\text{max}} + d\mathbf{s}$  of the suspension in the subwindow. To obtain subpixel resolution, I used a classical three-points Gaussian fitting in each coordinate direction [134],

$$ds_i = \frac{1}{2} \frac{\ln(C_{\text{PIV}}(s_i^{\text{max}} - 1)) - \ln(C_{\text{PIV}}(s_i^{\text{max}} + 1))}{\ln(C_{\text{PIV}}(s_i^{\text{max}} - 1)) - 2\ln(C_{\text{PIV}}(s_i^{\text{max}})) + \ln(C_{\text{PIV}}(s_i^{\text{max}} + 1))}, \quad (2.2)$$

where  $i = x, y$ . This measure then gives the bacterial flow  $\mathbf{u}(\mathbf{x}, t) = \tilde{\mathbf{s}}/dt$ , at the position  $\mathbf{x}$  in the centre of the subwindow.

Bacterial motion is often turbulent with a short time correlation, typically less than 1 s [135, 136]. In the case of flattened drops however, the circulation was stable until oxygen depletion, slowing down over time but without changing direction. To improve the accuracy of the measurement, the correlation function  $C_{\text{PIV}}$  was averaged over the 250 frames (2 seconds) of a movie [137]. PIV calculations were performed on a customised version of mPIV [134], a MATLAB (The MathWorks) toolbox. All modifications were done in collaboration with Aurelia Honerkamp-Smith, post-doc in the group, who used the same algorithm to measure the motion of fluorescent beads inside and around vesicles.

## Cell orientation

Akin to nematic liquid crystals, dense rod-like bacteria align locally. The suspension is too dense to distinguish individual cells. However bacteria form a striated pattern, indicating the mean local orientation.

To measure this orientation, I adapted an ImageJ plugin, *OrientationJ* [138], on MATLAB. The algorithm computes the local orientation tensor

$$J(\mathbf{n}) = \begin{pmatrix} \langle I_x \cdot I_x \rangle & \langle I_x \cdot I_y \rangle \\ \langle I_x \cdot I_y \rangle & \langle I_y \cdot I_y \rangle \end{pmatrix}, \quad (2.3)$$

where  $I$  is the pixel intensity,  $I_x$  and  $I_y$  its derivatives along each direction and  $\langle \cdot \rangle$  a weighted average around pixel position  $\mathbf{n}$ . The eigenvector of  $J$  of lowest eigenvalue indicates the local orientation  $\theta$  (figure 2.5a). Calculation gives [138]

$$\theta = \frac{1}{2} \arctan \left( \frac{2\langle I_x \cdot I_y \rangle}{\langle I_x \cdot I_x \rangle \langle I_y \cdot I_y \rangle} \right). \quad (2.4)$$

## 2.2.2 Results

### Circulation

While the dynamics of dense bacterial suspension in unconfined environments is quasi-turbulent, displaying transitory swirls and jets, confining the suspension into a flattened drop can stabilise its motion into a vortex state (figure 2.5b). To quantify this effect, I measured the vortex order parameter  $\Phi$ , defined as

$$\Phi = \frac{\frac{\sum_{\mathbf{x}} |\mathbf{u}(\mathbf{x}) \cdot \mathbf{t}(\mathbf{x})|}{\sum_{\mathbf{x}} \|\mathbf{u}(\mathbf{x})\|} - \pi/2}{1 - \pi/2}}, \quad (2.5)$$

where  $\mathbf{u}$  is the bacterial flow measured by PIV at all positions  $\mathbf{x}$  inside the drop, and  $\mathbf{t}$  the local azimuthal unit vector (figure 2.5a). The parameter  $\Phi$  measures how well the bacterial circulation orders into a vortex. If all cells move along the azimuthal direction with a constant speed,  $\mathbf{u} = u\mathbf{t}$ ,  $\Phi = 1$ . Instead, if the direction of motion is uncorrelated with the azimuthal direction,

$$\frac{\sum_{\mathbf{x}} |\mathbf{u}(\mathbf{x}) \cdot \mathbf{t}(\mathbf{x})|}{\sum_{\mathbf{x}} \|\mathbf{u}(\mathbf{x})\|} = \pi/2, \quad (2.6)$$

and  $\Phi = 0$ . Finally, if the flow is purely radial,  $\mathbf{u} \cdot \mathbf{t} = 0$  and  $\Phi = \frac{-\pi/2}{1-\pi/2} < 0$ .

Since the setup has a top/bottom symmetry (gravity is negligible), the suspension should circulate CW or CCW with equal probability. To test this hypothesis, I measured the circulation direction on all 29 drops forming a steady vortex on a given day. I obtained 14 movies with CCW circulation and 15, CW.

I measured  $\Phi$  over drops of different diameters  $d$  (figure 2.5d) and found three different circulation states. If the chamber is  $25\ \mu\text{m}$  high, drops between  $d_- \approx 30\ \mu\text{m}$

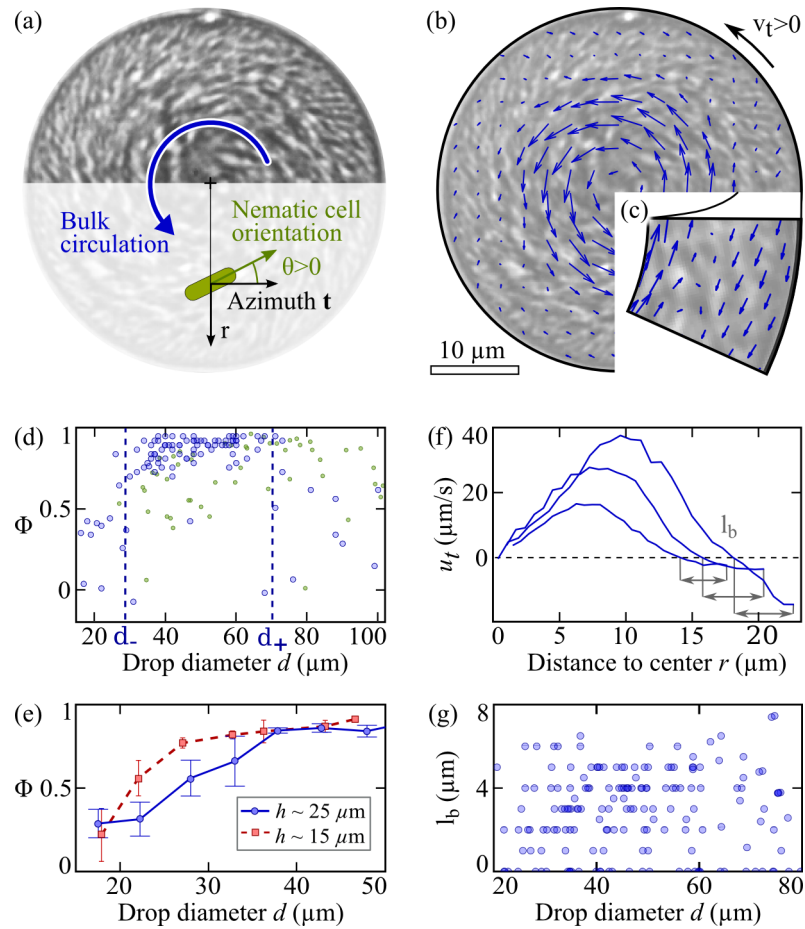


Figure 2.5: Circulation of dense suspensions of *B. subtilis* in flattened drops. (a) Bright field image of a drop and definitions of  $r$ ,  $\mathbf{t}$  and  $\theta$ . (b) Bacterial flow measured by PIV. Not all PIV arrows are shown. (c) Enlarged region showing the boundary layer to move in opposite direction to the bulk. (d) Vortex order parameter  $\Phi$  in  $25 \mu\text{m}$  high chambers. Each dot is a measurement over a two seconds long movie. Dense suspensions (large blue dots) form a stable vortex state between  $d_-$  and  $d_+$  (dotted lines). Semi-dilute suspensions (smaller green dots) still exhibit a vortex-like circulation at large diameter. (e)  $\Phi$  for two chamber heights  $h$ . The vortex is maintained in small drops by lowering  $h$ . Each point is an average over a  $5 \mu\text{m}$  bin. Error bars indicate standard deviation. (f) Averaged azimuthal flow  $u_t(r)$ . The region of negative circulation indicates the counterrotating boundary layer. (g) Boundary layer thickness  $l_b$ , as defined in (f), depending on the drop diameter  $d$ . Each dot is a measurement over a two seconds long movie. While data present a large spread due to measurement inaccuracy, no significant dependence on the drop diameter is observed. Adapted from [1]

and  $d_+ \approx 70\mu\text{m}$  exhibit a single vortex state,  $\Phi > 0.7$  (figure 2.6b). The suspension reaches a steady state in less than a minute (the transition was not captured in these experiments), the circulation is stable for  $\approx 10$  minutes until oxygen depletion, and does not change its direction.

For drops slightly larger than  $d_+$ , bacteria located less than  $30\mu\text{m}$  away from the oil interface still circulate along the azimuthal direction but some turbulence arises in the centre of the drop. For the largest drops,  $d \sim 100\mu\text{m}$ , the suspension forms a turbulent state similar to observations in unconfined chambers (figure 2.6c).

In drops smaller than  $d_-$ , the diameter is comparable to or smaller than the chamber height and the drop is not flattened anymore. Bacteria circulate in all three directions equally, in an unstable motion (figure 2.6a). The steady vortex state can be restored by lowering the top coverslip: in  $15\mu\text{m}$  high chambers, drops that are  $25\mu\text{m}$  in diameter still exhibit a stable circulation,  $\Phi > 0.7$  (figure 2.5e). Similarly if the chamber height is increased to  $40\mu\text{m}$ , no stable flow can be observed.

### Flow patterns of stable vortices

I now focus on drops that self-organise into stable vortices,  $d_- < d < d_+$  and  $h \approx 25\mu\text{m}$ . I first studied in more detail the bacterial flow by measuring the azimuthal flow profile for each drop

$$u_t(r) = \langle \mathbf{u}(\mathbf{x}) \cdot \mathbf{t}(\mathbf{x}) \rangle_{\|\mathbf{x}-\mathbf{x}_0\|=r}, \quad (2.7)$$

where  $\mathbf{x}_0$  is the centre of the drop,  $r$  the distance from the centre and  $\mathbf{t}$ , the local azimuthal unit vector, is chosen such that  $u_t$  is on average positive (figure 2.5b,f).

The azimuthal flow  $u_t$  is by definition antisymmetric (equation 2.7) and should thus go to zero at the centre of the drop,  $r = 0$ . Figure 2.5f shows that experimental estimates of  $u_t$  seem to originate from  $u_t(0) = 0$ , before increasing to reach a maximum value about mid-way to the oil interface,  $r \sim 10\mu\text{m}$ . The maximum velocity depends on the drop size (the larger, the faster) and on the oxygen concentration (the later in the experiment, the slower). The suspension could reach more than  $50\mu\text{m/s}$ , an order of magnitude faster than the single cell swimming speed  $v_0 \sim 5\mu\text{m/s}$ .

The azimuthal velocity  $u_t$  then decreases and reaches negative values: bacteria close to the oil interface move in opposite direction to the bulk circulation. This counterrotating layer was not a visual effect or a PIV artefact as confirmed by imaging the

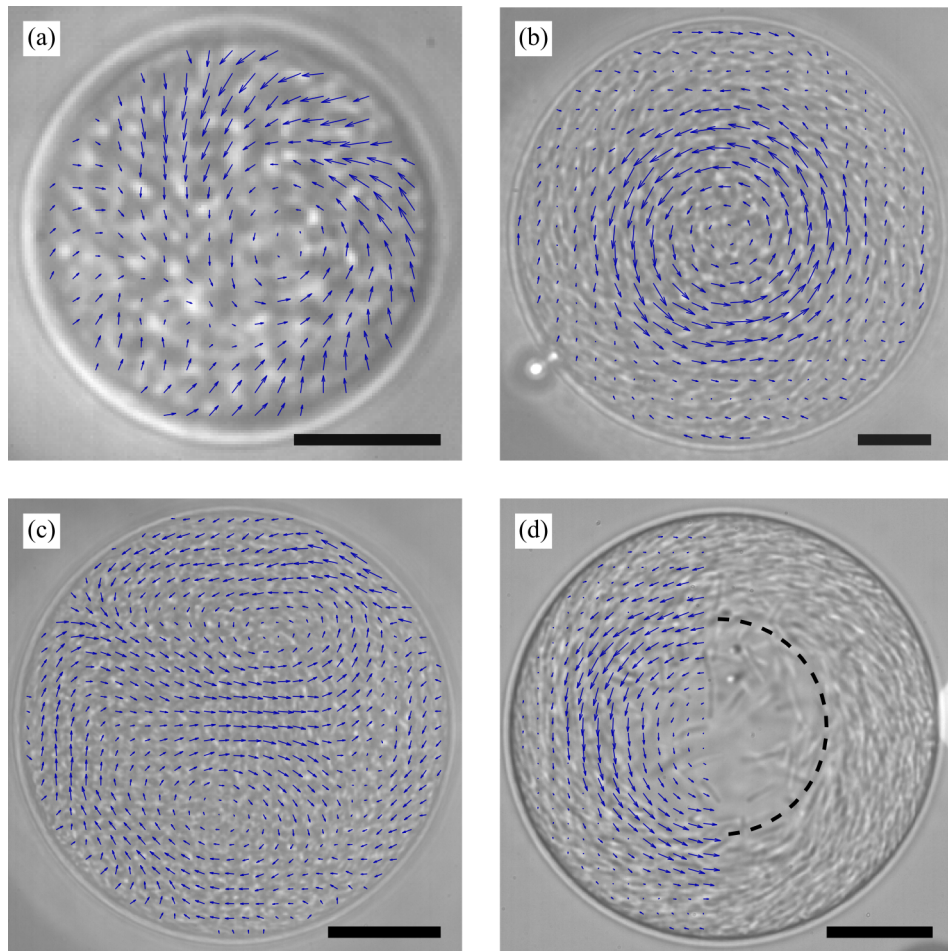


Figure 2.6: Circulation in drops of different diameter  $d$  and bacterial density. (a)  $d < d_-$ , bacteria circulate in all three dimensions, as indicated by the strong radial flow in the bottom left quadrant. (b)  $d_- < d < d_+$ , single stable vortex. (c)  $d > d_+$ , the suspension becomes turbulent, here forming two vortices. (d) Semi-diluted suspension. The centre of the drop is almost depleted in cells (dotted line). (a-d) arrows: bacterial flow measured by PIV, only a fourth of the measurements are shown for clarity, except in (a). Scale bars:  $10\mu\text{m}$  (a,b) and  $20\mu\text{m}$  (c,d).

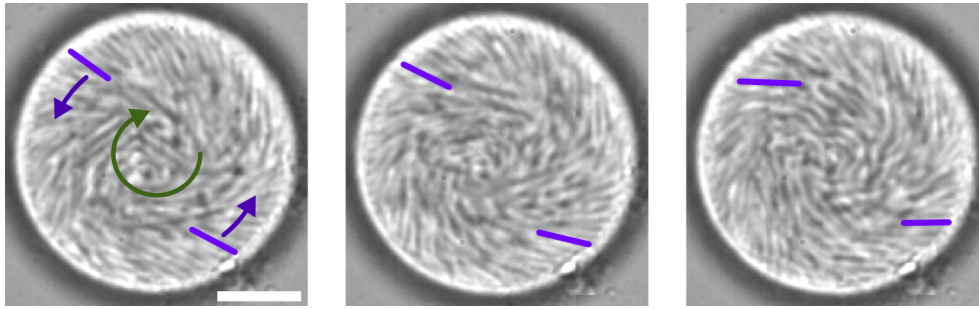


Figure 2.7: Single individual bacteria can be distinguished when imaging the bottom of the drop. Arrows: bacterial circulation direction. Rods: two bacteria tracked at the oil interface, moving against the bulk circulation. Bar:  $10\mu\text{m}$ . Images are taken every 0.2 second.

bottom of the drop where individual bacteria can be distinguished (figure 2.7).

I then estimated the thickness of the boundary layer  $l_b$  from  $u_t$  (figure 2.5f,g). For a given drop diameter,  $l_b$  can take values from 0 to  $8\mu\text{m}$ . This large spread is mostly due to inaccuracies in the measurement method: PIV subwindows are  $\approx 2\mu\text{m}$  in size, limiting the resolution, drops are not perfectly circular and the oil interface is often difficult to accurately detect. However the average thickness of the boundary layer  $\tilde{l}_b$  did not vary with the drop diameter (figure 2.5g). Moreover  $\tilde{l}_b \approx 4\mu\text{m}$  is smaller than the single cell length, 5 to  $8\mu\text{m}$  for these *B. subtilis* [7], indicating that only cells in contact with the oil interface move against the bulk circulation. Imaging at the bottom of the chamber also confirmed this observation (figure 2.7).

Moreover, I measured the maximum velocity in the boundary layer. Bacteria move at  $\sim 5\mu\text{m/s}$ , independently of the drop diameter.

Occasionally I also observed microdrops in the oil phase, moving with the boundary layer and against the bulk circulation. The oil is most certainly dragged at the drop edge by the bacteria and water circulation. This motion was much slower than that of the bacteria. Unfortunately I was not able to quantify this motion. I tried to add microbeads but this operation is quite challenging as most beads end up in the water phase.

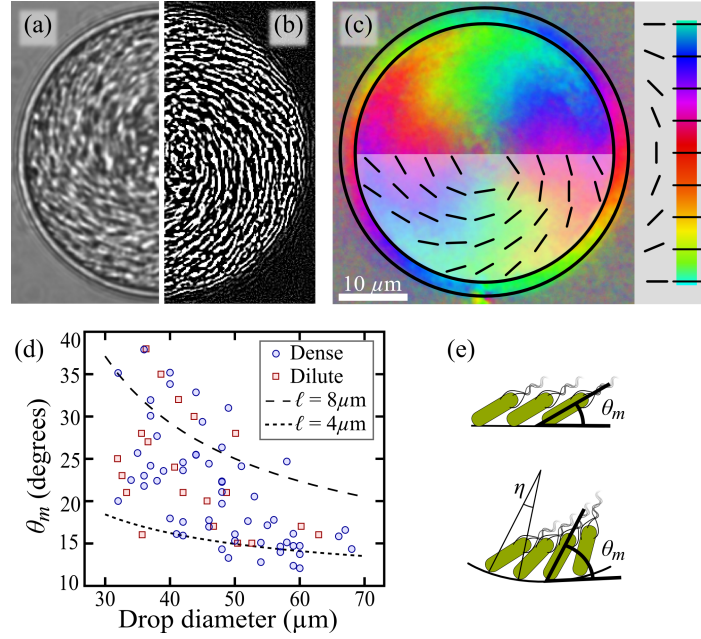


Figure 2.8: Bacteria form a spiral vortex pattern. (a) Bright field image of a drop shows the bacterial suspension to be oriented along a spiral pattern. (b) Right-side of the same drop after processing with an edge detection filter (ImageJ function 'Convolve'). (c) Local orientation, averaged over 2 seconds. The outer ring is located at the oil interface and colour coding indicates the local azimuthal direction. (d) Angle of the cells at the interfaces. Dots: experiments with dense (circles) and diluted (squares) suspensions. Lines: theoretical angle for 4 and 8  $\mu\text{m}$  long rectangles. (e) Model: at constant cell length and concentration,  $\theta_m$  increases with the curvature (decreases with the drop diameter). Adapted from [1].

## Bacterial orientation

On a static viewpoint, bacteria form a spiral pattern (figure 2.8a). I measured the mean local orientation as the eigenvector of lower value of the orientation tensor computed from the bacterial speckle. I then calculated the mean angle  $\theta(r)$  between this orientation and the azimuthal direction  $\mathbf{t}$  (figure 2.5a) depending on the distance to centre (figure 2.8). Bacteria mostly appear parallel to  $\mathbf{t}$  in the centre of the drop,  $\theta(0) = 0$ , and diverge from  $\mathbf{t}$ , to reach a maximum angle  $\theta_m$  at the oil interface (figure 2.8c). Plotted against the drop diameter,  $\theta_m$  is smaller for larger drops,  $\theta_m(d = 30 \mu\text{m}) \approx 30^\circ$ ,  $\theta_m(d = 70 \mu\text{m}) \approx 15^\circ$  (figure 2.8d).

To gain insights into this dependence, I calculated the smallest angle  $\theta_{\text{th}}$  that a set of

rectangles, the size of bacteria, can make at a curved interface (figure 2.8e).  $\theta_{\text{th}}$  depends on the rectangle size, density and on the interface curvature. At low density, rectangles can align with the interface,  $\theta_{\text{th}} = 0$ , and at highest density they align perpendicularly,  $\theta_{\text{th}} = \pi/2$ . Likewise, the larger the curvature, i.e. the smaller the drop, the larger the angle  $\theta_{\text{th}}$  (figure 2.8e). Finally, longer rectangles yield a larger angle to the interface. I calculated  $\theta_{\text{th}}$  by solving on MATLAB the set of following equations

$$\tan(\theta_{\text{th}} + \eta) = \frac{\ell_1 \sin \theta_{\text{th}} - d(1 - \cos(\eta))/2 - \ell_2 \cos(\theta_{\text{th}} + \eta)}{\ell_1 \cos \theta_{\text{th}} - d \sin(\eta)/2 + \ell_2 \sin(\theta_{\text{th}} + \eta)}, \quad (2.8)$$

$$\eta = \frac{\ell_1 \ell_2}{V_f (\ell_1 \sin(\theta_{\text{th}}) + \ell_2 \cos(\theta_{\text{th}})) (d - \ell_1 \sin(\theta_{\text{th}}) - \ell_2 \cos(\theta_{\text{th}})) / 2}, \quad (2.9)$$

where  $\ell_1$  is the cell length,  $\ell_2$  its width,  $d$  the drop diameter,  $\eta$  the angle between the end of two neighbouring cells, seen from the drop centre (figure 2.8e). The volume fraction  $V_f$  is the only parameter that I cannot measure accurately in experiments. I set the cell length  $\ell_1 = 4$  or  $8 \mu\text{m}$ , the cell width  $\ell_2 = 1 \mu\text{m}$  and manually fit  $V_f$  with experimental data (figure 2.8d). If  $V_f = 40\%$ ,  $\theta_{\text{th}}$  matches the trend observed in experiments. This volume fraction appears much larger than my measurements (I estimate the overall suspension volume fraction around 10%) but not unrealistic: first, my experiment measurement is quite inaccurate and could underestimate the actual volume fraction. Then, flagella which are invisible under bright field illumination, take up space around bacteria and could increase their effective volume fraction.

### Semi-dilute suspensions

In addition, I performed experiments with semi-dilute suspensions: bacteria are diluted after centrifugation but still exhibit collective motion in unconfined chambers. For these experiments, I mixed the pellet with supernatant (TB) at ratio 1/4 to 3/4, to reach a volume fraction between 1 to 10%. When placed inside flattened drops, the suspension still forms a single vortex, except for bacteria accumulating at the edge of the drop, leaving the centre empty (or with a few non-motile cells, figure 2.6d). The thick layer enriched in cells seems homogeneous. Visually, the cell density depending on the distance to the centre then appears as a step function: zero in the centre and constant closer to the edge (figure 2.6d). Diluting the bacterial suspension prevents the transition for a stable vortex to a turbulent state: the net flow  $\Phi$  stays larger than 0.5 for

drops around  $100\mu\text{m}$  in diameter. This result is not in contradiction with those from the dense suspension as the turbulence first arises in the centre of the drop, which here is depleted in cells.

Furthermore, the cell orientation at the oil interface, as quantified by the angle  $\theta_m$ , is unchanged (figure 2.8d). This result shows that this angle only depends on local properties (cell concentration, interface curvature) but not on the bulk organisation.

A year after we published this result, Vladescu *et al.* presented measurements in spherical drops filled with *E. coli* and found that, in this setup, the concentration profile is not a step function but instead peaks at the oil interface and is constant in the bulk, increasing with the overall bacterial concentration [139]. This difference may arise from the shape of the drops which are not flattened in their experiment and from the use of a different bacterial species.

### 2.2.3 Discussion

#### Active matter under circular confinement

Even though I am not aware of any other experiment that confined a dense bacterial suspension, circular confinement has already been shown to affect the self-organisation of other active systems. Here, I give a few examples, briefly summarising the interaction mechanisms and the resulting motion:

**Bristle-bots** Centimetre-sized objects are set into motion by the vibration of a table [39, 40, 41]. They have either elongated or circular shapes but are always polar: the motion direction is set by the shape of the bristles in contact with the table (figure 2.9a). Bristle-bots organise only by direct steric interaction and through circular confinement. Under some conditions, these objects self-organise into a single vortex state, without a boundary layer. Remarkably, the elongated shape is not necessary to obtain this circulation [39]. Furthermore, Kumar *et al.* [41] have filled the chamber with mm-large beads (figure 2.9b). Bristle-bots there interact through indirect long-range forces, transmitted by this granular medium, and still managed to form a similar vortex state.

**Eukaryotic cells on patterned surfaces** A large circular pattern is filled with a monolayer of crawling cells. Cells are constantly in direct contact with their neigh-

bours and show an initial random motion direction (figure 2.9c). They spontaneously start moving in a common direction, again without a countercirculating boundary layer [125].

**Rotating cell nucleus** A single fibroblast cell is placed on a small circular pattern. The actin cytoskeleton grows from the outer edge of the cell, and thus shows a net motion towards the nucleus at the centre. Active stresses in the cytoskeleton spontaneously break the cell symmetry, resulting in the rotation of the nucleus (figure 2.9d). Once again, no double circulation was observed [126].

**Chara vesicles** As presented at the beginning of this chapter, when the cytoplasm of a *Chara* cell is manually extracted, tens of microns sized vesicles form, containing actin bundles and myosin motors. Some of these vesicles spontaneously create a vortex state with edges moving in opposite direction to the bulk, as also observed with dense bacterial suspensions [129, 131]. In *Chara* vesicles, the behaviour is probably due to the motion of actin filaments at the edge, against myosins which haul the bulk. In comparison, flattened drops of *B. subtilis* have similar swimming bacteria at the oil interface and in the bulk.

## Boundary layer

Even though all these active systems can self-organise into a vortex state, the flow pattern in dense bacterial suspensions differs significantly: in all flattened drops, irrespective of their diameter, a single layer of bacteria ( $\sim 4\mu\text{m}$ ) moves in the opposite direction to the main bulk circulation.

Bristle-bots are probably the system closest to swimming bacteria: both can exhibit elongated shapes with similar aspect ratio, are self-propelled and interact through direct steric repulsion. The major difference comes from the fluid flows that bacteria generate which can affect the organisation of the suspension at long-range. The boundary layer then probably arises from these hydrodynamic interactions or from microscopic effects. Moreover, when bristle-bots are placed in a granular medium, even though they generate granular flows, all objects still move in the same direction. The exact details of the fluid flow patterns around swimming bacteria is thus important to understand their self-organisation. This question will be studied in the next chapter.

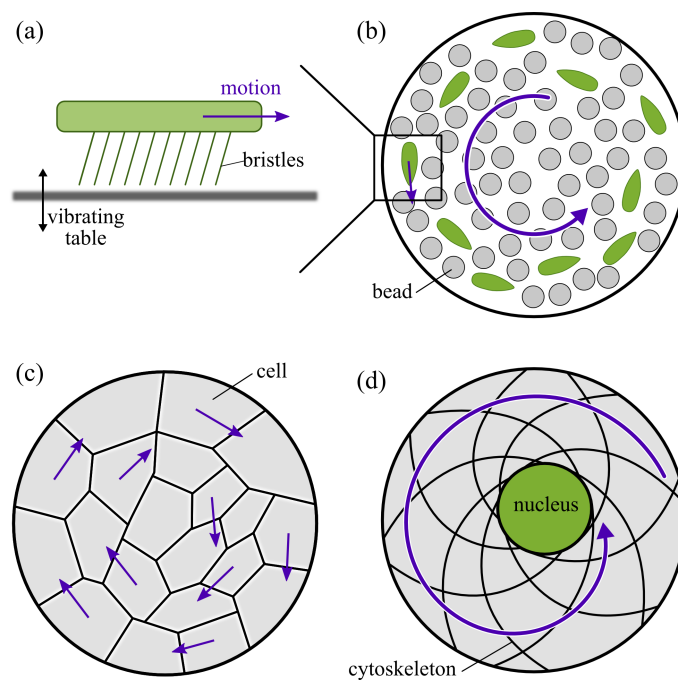


Figure 2.9: Vortex states in different active systems. (a,b) Bristle-bots, are set into motion by the vibration of a table [39, 40, 41] and can interact either by direct repulsion or through a granular medium [41]. Bots are typically 5 mm long and beads 1 mm in diameter. (c) Monolayer of crawling cells on a circular pattern [125]. (d) Flow of the cytoskeleton and nucleus of a single cell on a small circular pattern [126].

## Length scales

Turbulent vortices have been commonly observed in unconfined suspensions, with lifetimes less than 1s [135, 136]. Confining the suspension into a flattened drop stabilises such a vortex for more than 10 minutes, until oxygen depletion. I found two critical diameters,  $d_- \approx 30\mu\text{m}$  that ensures the quasi-2D confinement and  $d_+ \approx 70\mu\text{m}$  after which the suspension recovers its turbulent behaviour.

Notably  $d_+$  is comparable to the swirl diameter measured in quasi-2D chambers. Patterns in unconfined suspensions are usually studied by their spatial correlation which gives a typical length scale of  $40\mu\text{m}$  as the radius of the turbulent swirls [7, 31, 32]. Measurements in racetracks (section 2.3) revealed a swirl diameter of  $90\mu\text{m}$ . These measurements indicate that confinement stabilises the suspension but does not increase its typical length scale.

## 3-dimensional flow

A common interrogation is whether bacteria move in the vertical direction. When the drop diameter is smaller than  $30\mu\text{m}$ , of comparable length to the chambers height  $h \approx 25\mu\text{m}$ , bacteria circulate randomly and unsteadily in all three directions. When the drop diameter is increased, most of the flow seems to be confined to the horizontal plane. I tried to observe remaining vertical flow by adding  $1\mu\text{m}$  fluorescent beads which are advected by the fluid flows but also pushed by the bacteria. I imaged them using a confocal spinning disc illumination, which highly restricts the thickness of the focal plane (better z-resolution). I observed beads to move in the same direction as the bacteria and to mostly stay in the focal plane, suggesting that the vertical flow was negligible compared to the in-plane motion:  $u_z \ll u_{x,y}$ .

## 2.3 Racetracks

Bacteria and other microswimmers have often been studied in microchannels, in which they have been shown to accumulate at surfaces [113, 114] and, in the presence of an external fluid flow, to move in a common direction [122, 123, 124]. Yet, there has been no experimental realisations of dense bacterial suspensions in channels and only

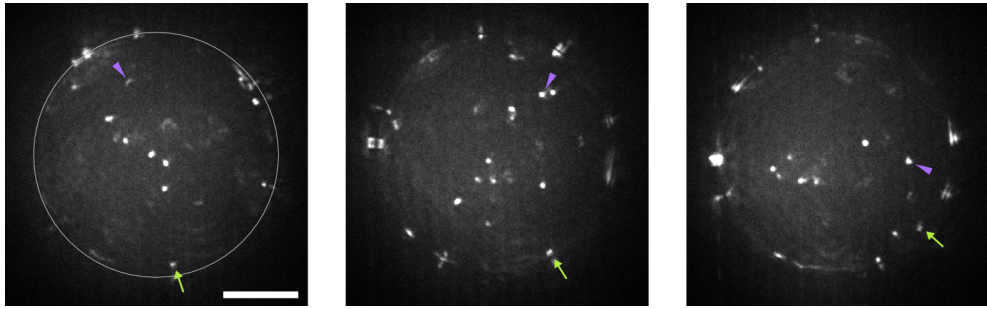


Figure 2.10: Fluorescent  $0.5\mu\text{m}$  beads, imaged in a drops of *B.subtilis*. Beads in the bulk (purple triangle) circulate CW while beads at the oil interface (green arrow, grey circle) move CCW, both are going in the same direction as the bacteria. Bar:  $10\mu\text{m}$ . 1.2 second between images.

a few simulations and theoretical studies have considered this case, with contradictory results [103, 105, 140].

Instead of using linear microchannels, I designed periodic racetracks, tens of  $\mu\text{m}$  high and wide (as in flattened drops) but more than 1 mm long. In these microchambers, bacteria are able to quickly self-organise into a persistent stream, stable for tens of minutes. In this section, I quantitatively study the flow characteristics, show surfaces to play a critical role and present a model of pattern formation.

### 2.3.1 Protocol

#### PDMS microchamber

The main difference between racetrack and flattened drop experiments is the design of the microchambers. I fabricated racetracks in the laboratory with polydimethylsiloxane (PDMS) following a standard microlithography protocol (figure 2.11). Channels were drawn on computer and printed on a plastic sheet (mask) at high resolution by an external company (Microlitho). I then spin-coated a thin layer of SU-8 (Microchem) on a silicon wafer at 1500 to 2000rpm. SU-8 is a light-sensitive material that solidifies under UV exposure. The wafer was prebaked at  $95^\circ$  for 5 min and placed beneath a UV lamp for  $3 \times 8\text{s}$ , with the mask place on top such that SU-8 solidifies only at the location of channels. After baking a second time at  $95^\circ$  for 6 min, the uncurrred SU-8 was removed in a bath of solvent (PGMEA, 4min), such that only the negative

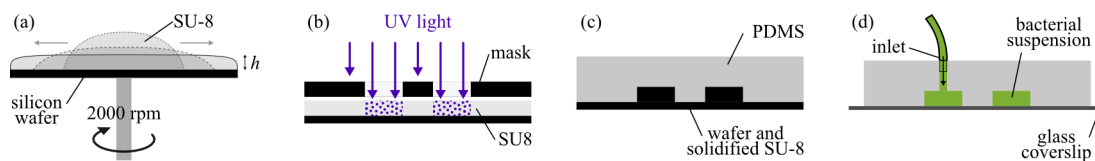


Figure 2.11: Protocol for PDMS chambers preparation. (a) A silicon wafer is coated with a thin layer of SU-8. (b) Exposure to UV light through a mask solidifies negative patterns in the SU-8 layer. (c) PDMS is then poured on the cleaned wafer to form the microchannels. (d) PDMS is then bound to a coverslip and the bacterial suspension is injected through hand-made inlets.

of the microchannels was left on the silicon wafer. A 5 mm thick layer of PDMS (Sylgard 184, Dow Corning), was then poured onto the patterns. PDMS is a polymer that solidifies when mixed with a curing agent (at 10% w/w). After baking to accelerate the solidification ( $70^\circ$  for at least 3 h), individual chambers were cut and punctured at inlets and outlets. PDMS and a glass coverslip were washed with ethanol and dried with pressurised nitrogen. PDMS was finally bound to the glass coverslip using an oxygen plasma ( $2 \times 10$  s exposure). Surface binding after this oxygen treatment is irreversible and the chamber could sustain high pressure.

### Racetracks

Microchannels were shaped into racetracks,  $20 \mu\text{m}$  in height,  $20 - 120 \mu\text{m}$  in width and more than a millimetre in length. To simplify the analysis, racetracks had two straight parts, rather than being perfectly circular (figure 2.12b). They were linked by thinner channels ( $\sim 10 \mu\text{m}$  wide), into a chain of racetracks ended by inlets (figure 2.12a). Connecting channels were thin,  $\approx 10 \mu\text{m}$ , and long,  $\gg 200 \mu\text{m}$ , avoiding interactions between adjacent racetracks.

### Suspension preparation and imaging

Wild type *B. subtilis* were grown in TB and concentrated by centrifugation following the same protocol used for flattened drops (section 2.2.1). They were manually injected using a syringe. To stop external flows, inlets were sealed with a broken and closed syringe needle. The system reached steady state in less than 2 minutes, before I took any movie. Five second long movies were acquired and analysed with the same

method. I used a 63× oil-immersion objective and recorded at 60 or 125 frames/s. PIV measurements were not averaged over time and computed every 10 frames only. No evaporation was observed as I used the microfluidic chamber for less than 15 minutes.

### 2.3.2 Results

As in drops, confining a dense suspension into a racetrack stabilises the suspension motion but this time into a stream. Bacteria at interfaces also move in opposite direction to the bulk (figure 2.13). However due to the lower magnification and the roughness of PDMS surfaces, PIV measurements could not catch this feature. I analysed racetrack experiments by measuring the net flow, correlation lengths and flow profiles, depending on the channel width.

#### Net flow

In thin channels the suspension exhibits a directed stream, going either CW or CCW. To quantify this motion, I measured the normalised net flow  $\Psi$ , defined as

$$\Psi = \left| \frac{\sum \mathbf{u} \cdot \mathbf{e}_x}{\sum \|\mathbf{u}\|} \right|, \quad (2.10)$$

where  $\mathbf{u}$  is the bacterial flow as measured by PIV,  $\mathbf{e}_x$  the local unit vector along the channel main direction (figure 2.12c). Both sums span over all PIV subwindows inside the channel and over  $\approx 70$  frames of a 5 second long movie.  $\Psi = 1$  denotes a purely longitudinal flow, e.g.  $\mathbf{u} = \|\mathbf{u}\|\mathbf{e}_x$ , and  $\Psi = 0$  an overall stationary suspension.

$\Psi$  is further averaged over all movies for a given channel width  $w$  (figure 2.14).  $\Psi$  shows a clear dependence on  $w$ , with strong streaming for thin racetracks and no large scale circulation for wide ones (figure 2.14). The critical width  $w^* \approx 70\mu\text{m}$  at which streaming ceases,  $\Psi < 0.2$ , is comparable to the critical diameter in flattened drops  $d_+ \approx 70\mu\text{m}$ .

#### Flow patterns

In order to understand this transition from a stable circulation to the stationary state, I now describe the different flow patterns occurring depending on the channel width (figure 2.15a), which I quantitatively study in the next subsections.

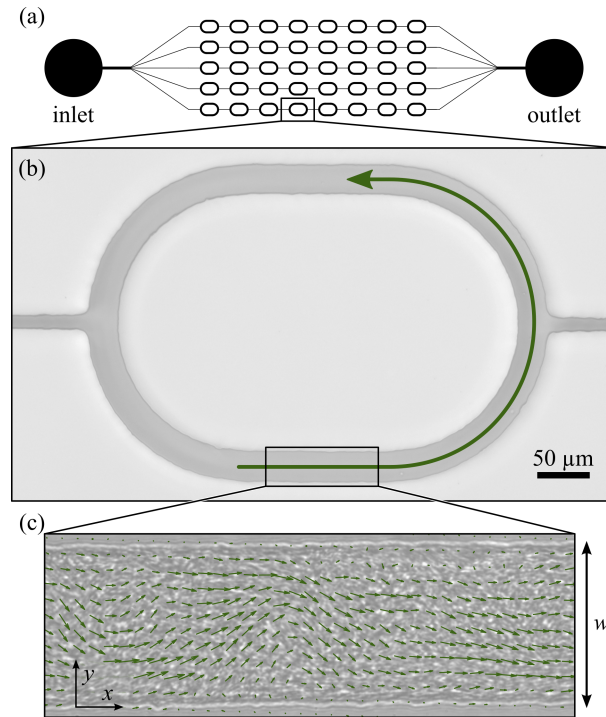


Figure 2.12: Spontaneous circulation in a periodic channel. (a) Design of the microfluidic chamber. Bacteria are injected through the inlet which is then closed to avoid external flows. (b) Close up on one racetrack. Arrow: net circulation. (c) Close up on the straight section of the racetrack where all measurements are performed. The x-axis is set along the channel length, in the main streaming direction. Arrows: bacterial flow measured by PIV. Adapted from [3].

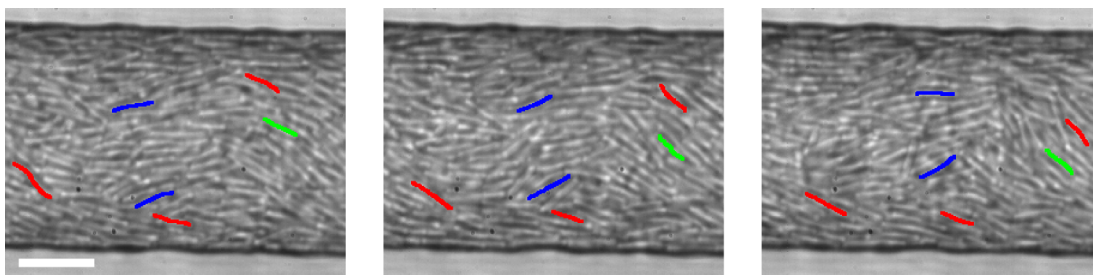


Figure 2.13: Individual bacteria can be distinguished when imaging the bottom of the channel. The bulk is moving from the right to the left side, while bacteria at the glass interface (coloured lines) swim to the right side. Bacteria were tracked and coloured by hand. Bar: 10 μm. Time between frames: 0.16 s

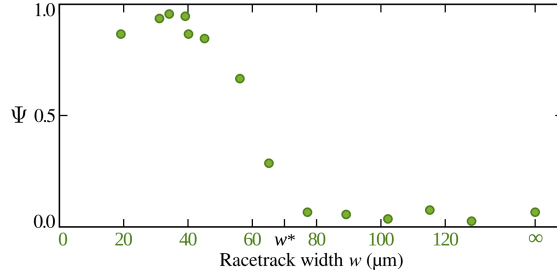


Figure 2.14: Normalised net flow  $\Psi$  depending on the channel width  $w$ .  $\Psi$  shows a clear transition from a strong stream to a stationary motion. The net flow ceases around  $w^* \approx 70 \mu\text{m}$ . Each point is an average taken over at least five movies, on at least 2 different days.  $\infty$ : unconfined quasi-2D chambers. Standard error  $< 0.1$  (not shown). Adapted from [3].

For channels thinner than the critical width  $w^* \approx 70 \mu\text{m}$ , nearly all bacteria in the bulk move in the same direction. Confinement dampens the turbulence such that the suspension solely creates partial swirls. The flow pattern then appears as a wave.

Around the critical width,  $w \approx w^*$ , the suspension is able to form full vortices. Each side of the channel moves in opposite direction to the other, resulting in no net flow. Moreover, vortices have a preferred direction, CW or CCW depending on the circulation direction at the PDMS interface.

For the largest channels, the suspension recovers its turbulent behaviour, with little or no correlation between opposite sides.

### Correlation lengths

A classical approach to characterise flow patterns in dense bacterial suspensions is to measure the spatial correlation. I adapted the usual isotropic formulation to take advantage of the linear geometry of the racetracks:

$$C(s) = \frac{\sum u_y(x, y, t) \cdot u_y(x + s, y, t)}{\sum \|u_y(x, y, t)\|^2} \quad (2.11)$$

where  $u_y = \mathbf{u} \cdot \mathbf{e}_y$  is the flow perpendicular to the channel main direction. The sum runs over all PIV sub-windows in the bulk of the channel, and over  $\approx 70$  frames of a 5 second long movie. Note that this formulation only correlates flow along the  $\mathbf{e}_x$  direction.

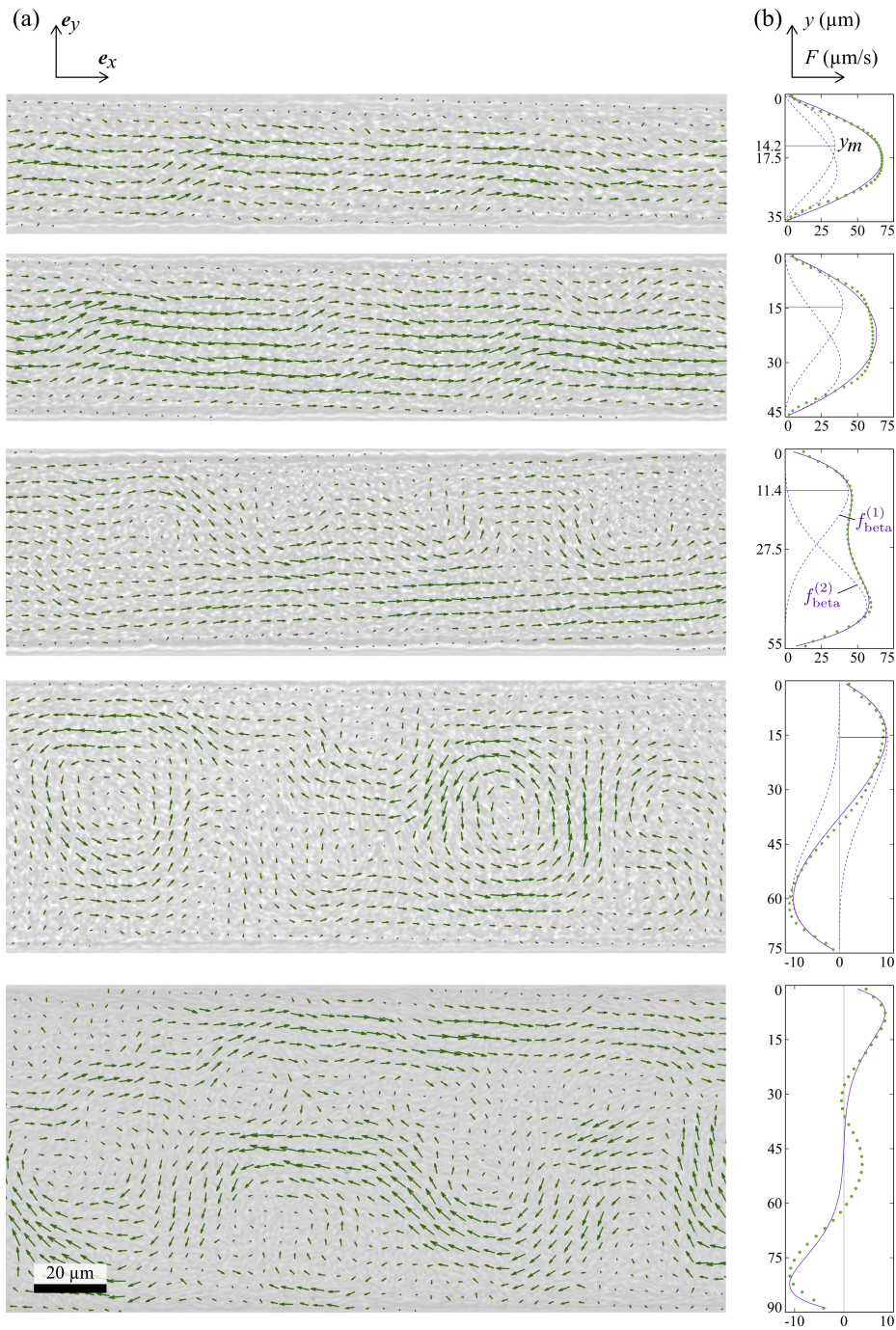


Figure 2.15: Bacterial flow patterns depending on the channel width. (a) Bacterial flow measured by PIV. Channel width 35, 45, 55, 75 and 90 μm. (b) Flow cross section  $F(y)$  in experiments. Dots: measurements. Solid line:  $F_{\text{fit}}$ . Dotted lines:  $f_{\text{beta}}^{(1)}$  and  $f_{\text{beta}}^{(2)}$ . Adapted from [3].

For all channels,  $C$  initially decreases from  $C(0) = 1$  to negative values, oscillates and fades at large distances,  $C(s \rightarrow \infty) = 0$  (figure 2.16b). Such correlation behaviour which includes oscillations, has been observed for unconfined suspension, using an isotropic definition of the correlation function, but has never been fully analysed. Two standard approaches have been used to extract the correlation length: fitting with a decaying exponential or measuring the first zero or minimum of  $C$ . I combined the two techniques to fit  $C$  with the function

$$C_{\text{fit}} = \left[ A e^{-s/L_e} + (1 - A) \right] \cdot \cos(2\pi s/L_c), \quad (2.12)$$

where the first and second term capture the amplitude decay and oscillations, respectively.  $L_c$  is first estimated as the maximum of the Fourier transform of  $C$ .  $L_e$  and  $A$  are both estimated, knowing  $L_c$ , using the Matlab function *fit*.

$L_c$  reflects the swirl size (the pattern spacial periodicity) and  $L_e$  the decay length scale (persistence length). They share a similar dependence on the channel width  $w$  (figure 2.16a), increasing with  $w$  to reach a plateau around  $w \approx 80\mu\text{m}$ , shortly after streaming ceases,  $w^* \approx 70\mu\text{m}$ , and when the suspension is able to form full vortices. Values at the plateau,  $L_c \approx 90\mu\text{m}$  and  $L_e \approx 50\mu\text{m}$ , are comparable to measurements in unconfined chambers (noted  $\infty$  on figure 2.16a)

### Flow cross section

I then quantitatively measured the averaged flow along the channel direction

$$F(y) = \langle \mathbf{u}(x, y, t) \cdot \mathbf{e}_x \rangle_{(x,t)}, \quad (2.13)$$

where  $\mathbf{e}_x$  is chosen such that  $F$  is on average positive. In the case of a passive Newtonian fluid driven by a pressure gradient, this profile should appear parabolic or flat [141]. Instead, bacteria forming partial or full swirls, exhibit complex flow profiles, highlighting the interplay between boundaries and bacterial collective motion.

Figure 2.15b shows different profiles depending on the channel width. For the thinnest channels,  $w \sim 30\mu\text{m}$ ,  $F$  is quasi parabolic.  $F$  then flattens and splits into a double peak function, at  $w \sim 50\mu\text{m}$ . When the channel is large enough for the suspension to form full vortices,  $F$  takes a sinusoidal shape, and finally gets multiple extrema

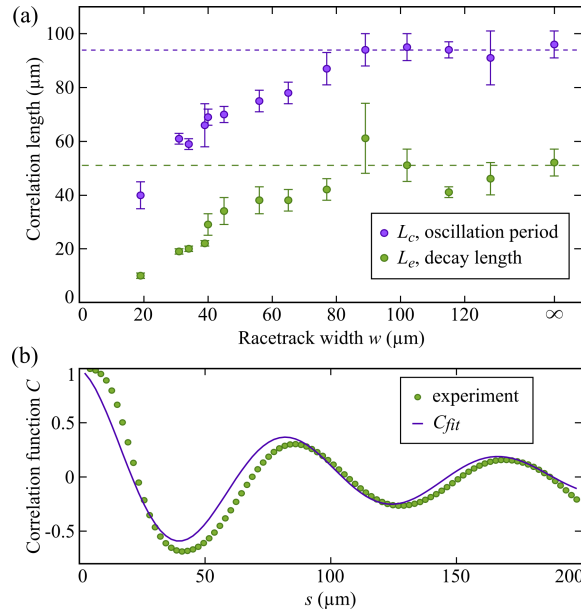


Figure 2.16: Spatial flow correlation. (a) Flow correlation lengths depending on the channel width  $w$ . Dots indicate experimental measurements averaged over at least five movies, taken on at least two different days. Bars: standard error. Dotted lines: value at plateau.  $\infty$ : unconfined quasi-2D chambers. (b) Example of a correlation function  $C$  (dots) and its fitting function  $C_{fit}$ . Adapted from [3].

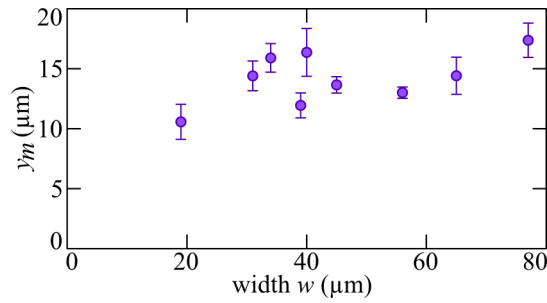


Figure 2.17: Distance  $y_m$  between the PDMS interface and the maximum of  $f_{\text{beta}}^{(1)}$ , as indicated in figure 2.15b by a thin black line. Each point is an average taken over at least five movies, recorded on at least two different days. Error bars: standard error. Adapted from [3].

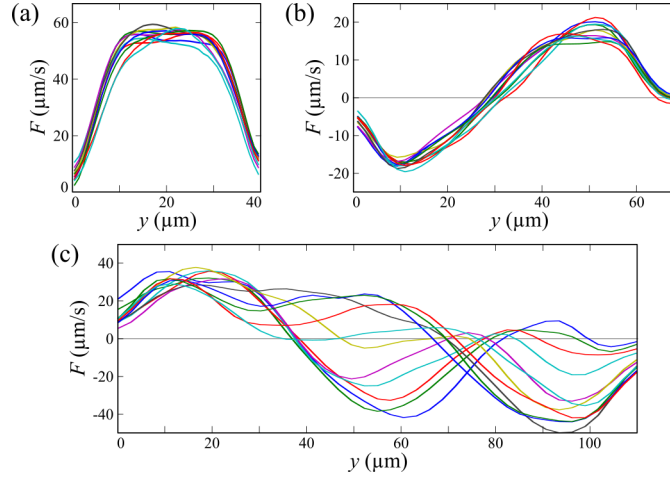


Figure 2.18: Bacterial flow cross section  $F^1(y, t)$  becomes unstable at large channel width. (a) Flat and (b) sinusoidal profiles slightly change between frames. (c) For large channel width, the suspension as well as the flow cross section become turbulent. Each line represents the flow cross section calculated over a single frame of a five seconds long movie.

in the largest channels,  $w \sim 100\mu\text{m}$ .

To assess the stability of the bacterial circulation I then studied the flow profile over time. I calculated the flow cross section on a single frame

$$F^1(y, t) = \langle \mathbf{u}(x, y, t) \cdot \mathbf{e}_x \rangle_{(x)}. \quad (2.14)$$

For thin channels,  $w < w^*$ , the suspension produces a stable net circulation.  $F^1$  does not change significantly with time and I never observe the overall circulation to switch direction (figure 2.18a). For intermediate channel width,  $w \approx w^*$ , the suspension presents a stable sinusoidal profile (figure 2.18b). The net flow is here negligible since each half of the channel moves in opposite direction to the other. For the largest channels instead,  $F^1$  quickly changes, highlighting the quasi-turbulent behaviour of the suspension (figure 2.18c).

In order to get insights into the transition from a parabolic to a double peak profile, I measured the distance  $y_m$  between the PDMS interface and the first maximum of  $F$ .  $y_m$  is straight forward to measure when  $F$  has two maxima. For parabolic and flat

profiles,  $F$  is fitted using two beta distribution functions,

$$\begin{aligned} F_{\text{fit}}(y) &= f_{\text{beta}}^{(1)} + f_{\text{beta}}^{(2)} \\ &= A_1 \left(\frac{y}{w}\right)^{\alpha-1} \left(1 - \frac{y}{w}\right)^{\beta-1} + A_2 \left(1 - \frac{y}{w}\right)^{\alpha-1} \left(\frac{y}{w}\right)^{\beta-1}, \end{aligned} \quad (2.15)$$

where  $A_1$  and  $A_2$  are the amplitude of each beta distribution function, and  $\alpha$  and  $\beta$  two parameters setting their shape. The functions  $f_{\text{beta}}^{(1)}$  and  $f_{\text{beta}}^{(2)}$  are symmetric, except for the amplitude:  $f_{\text{beta}}^{(2)}(y) = A_2/A_1 f_{\text{beta}}^{(1)}(w-y)$ . I also set  $\alpha = 2$  to ensure that  $f_{\text{beta}}^{(1)}$  (resp.  $f_{\text{beta}}^{(2)}$ ) has a non-zero finite derivative at  $y = 0$  (resp.  $y = w$ ). I used beta distribution functions for convenience, as they possess a single maximum and go to 0 at  $y = 0, w$ .  $F_{\text{fit}}$  has no physical basis to bacterial suspensions or fluid mechanics, except when  $\beta = 2$  which gives a parabolic profile, as expected for a passive fluid [141].

The beta distribution functions fit the different behaviours: for the smallest channels,  $f_{\text{beta}}^{(1)}$  and  $f_{\text{beta}}^{(2)}$  mostly overlap; they then come apart to form the double peak profile and adopt opposite signs ( $A_1 A_2 < 0$ ) when  $F$  is sinusoidal. At the largest width,  $F_{\text{fit}}$  only captures the first and last extrema.

I then calculated  $y_m$ , the distance at which  $f_{\text{beta}}^{(1)}$  reaches its maximum.  $y_m$  solely depends on  $\beta$  and  $w$ . Figure 2.15d shows that  $y_m$  does not depend on the channel width but rather stays at a fixed distance  $\approx 15 \mu\text{m}$  from the PDMS edge (with the exception of the thinnest channels where  $y_m = w/2$ ). Each beta distribution function then appears as pinned to opposite edges and to move apart as the channel gets wider. The overall cross section flow is here described as the sum of two main streams, driven close to the PDMS interface with a constant length scale  $y_m$ . This result emphasises the role played by boundaries in the overall circulation. As in flattened drops, bacteria at the surfaces move against the bulk and may be essential for the suspension self-organisation.

### Flow pattern motion

As bacteria move in the channel, the flow patterns they form do not stay static. I measured the motion of the partial swirls in thin channels ( $w < w^*$ ) by computing the spatial correlation function  $C_{\text{swirl}}$  between consecutive frames of a movie, defined as

$$C_{\text{swirl}}(s) = \frac{\sum u_y(x, y, t) \cdot u_y(x + s, y, t + \Delta t)}{\sum \|u_y(x, y, t)\|^2}, \quad (2.16)$$

where  $u_y = \mathbf{u} \cdot \mathbf{e}_y$  and  $\Delta t$  the time between consecutive frames. Sums run over all PIV subwindows inside the channel, and over  $\approx 70$  frames of a 5 second long movie. The distance  $s_m$  at which  $C_{\text{swirl}}$  reaches its maximum value indicates the average displacement of the pattern between two consecutive frames and the velocity of the swirl motion,  $V_{\text{swirl}} = s_m/\Delta t$ .

I compared this velocity with the average bacterial flow along the main channel direction:  $V_{\text{bacteria}} = \langle u_x \rangle_{x,y,t}$ . I found that  $V_{\text{swirl}}$  and  $V_{\text{bacteria}}$  had the same direction and the swirls seem to move faster. The ratio  $V_{\text{swirl}}/V_{\text{bacteria}}$  has a median of 1.2 with a standard error of 0.1. However the measurement of  $V_{\text{swirl}}$  is still rudimentary and can be biased or inaccurate. It is difficult to conclude whether the swirls are moving faster than the bacteria. Studying the dynamics of formation and motion of these partial swirls could nevertheless be an interesting approach to understand bacterial suspension behaviour.

This measurement could be improved by tracking single cells (as in Chapter 3) and following singularities in the flow pattern, such as a vortex centre. The relative motion would indicate whether the flow pattern moves faster or at the same speed as the swimmers.

### 2.3.3 Discussion

In both racetracks and flattened drops, the bacterial suspension shows a similar behaviour in which confinement stabilises the turbulent dynamics into a persistent stream or vortex, respectively. Both display bacteria swimming at interfaces moving in opposite direction to the bulk. The racetrack experiment can then be understood as a simple extension of the drops: in drops the suspension is confined in all three dimensions, whereas racetracks can be more than a millimetre long. Yet, racetracks also give valuable information on the general suspension behaviour. Two particular points discussed below are the length scale of the flow patterns and how interfaces drive the local organisation. I finally present a macroscopic model of the bacterial pattern formation depending on the channel width.

## Flow length scales

I have extracted three length scales, two from the correlation function and one from the flow cross section. The bacterial circulation stabilised in racetracks leads to a new picture of the correlation function, as the combination of an oscillating term and a decaying one. In previous studies, the latter dominates and few or no oscillations were observed, sometimes leading to a confusion between the persistence length (decay length) and the swirl size (oscillation period). I have computed both of these values depending on the channel width and showed that they reach a plateau value shortly after streaming ceases.

These lengths have been measured depending on other parameters, such as the oxygen concentration or the bacterial density. Of particular interest is the study by Gachelin *et al.* of diluted to dense unconfined suspensions of *E. coli*. They showed that the persistence length (decay length) increased with the cell concentration, quantifying the appearance of collective motion. Additionally, with the added insight from racetrack analysis, one can estimate the swirl size from the first zero of the correlation function. Interestingly, all correlation functions in Gachelin's article reach zero at the same distance,  $s \approx 55 \mu\text{m}$ , indicating that the swirl size does not depend on the bacterial concentration but is rather an intrinsic length associated with the swimmers. Cell-driven fluid flows, which generate long-range hydrodynamic interactions, are probably controlling this typical length [89].

I also measured the typical length scale between the PDMS interface and the maximum longitudinal velocity,  $y_m \approx 15 \mu\text{m}$ . This distance can be linked back to the swirl size  $L_c$ . Consider a typical vortex, with zero flow at the edge and in the centre. The maximum azimuthal velocity is roughly half way between the centre and the edge, as I found in flattened drops. If the edge of the vortex is placed at the PDMS interface, then the vortex diameter is typically  $4y_m \approx 60 \mu\text{m}$  (figure 2.19b), smaller but comparable with  $L_c^{\text{inf}} \approx 90 \mu\text{m}$ , the vortex size in unconfined chambers.

## Model of pattern formation

From the experimental observations, I now propose a model for the flow pattern formation (figure 2.19). As a starting point, it considers the turbulent dynamics of bacterial suspensions, which form swirls typically  $\sim 90 \mu\text{m}$  in diameter (figure 2.19a).

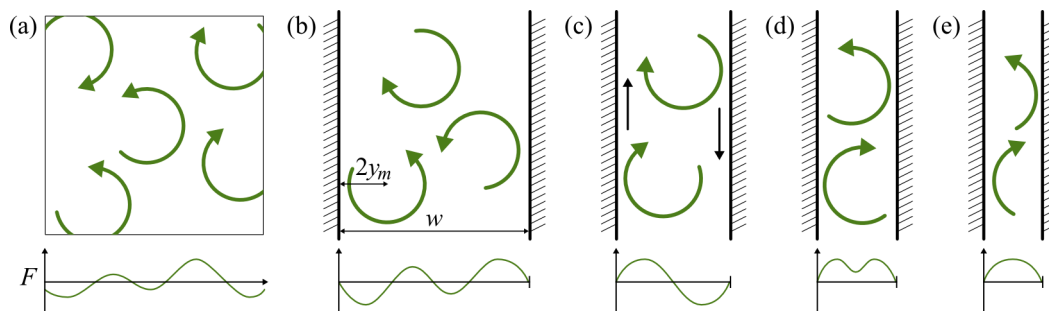


Figure 2.19: Model of pattern formation. The bacterial suspension forms swirls (green arrows), whose organisation depends on confinement. Plots indicate the cross section flow  $F$ . (a) Unconfined state. (b-e) Self-organisation in channels of decreasing width  $w$ .

In the presence of interfaces, these swirls are initiated at the boundaries with their centre located at about  $2y_m$  in the bulk (figure 2.19b). If the opposite wall is close enough,  $w < w^*$ , only partial truncated swirls are generated. The continuity and incompressibility of the flow then imposes neighbouring swirls to be placed on opposite sides, with inverse rotation directions, leading to the parabolic and double peaked flow cross section (figure 2.19d,e). However, when the channel width is large enough for a full vortex to form, continuity of the flow along the PDMS interface imposes the vortices to share the same rotation direction, leading to the sinusoidal profiles (figure 2.19c). At even larger width, vortices are free to form and the suspension recovers its turbulence, akin to that in unconfined chambers (figure 2.19a,b).

## Bacteria and interfaces

PDMS and glass surfaces appear to play a central role in the formation of the stream. Rather than confinement only, it is the combination of the two, interfaces and confinement, that leads to the suspension behaviour.

In particular, the fact that bacteria close to the PDMS interface generate a strong flow as revealed by the beta distribution functions, can be linked back to previous experiments in which bacteria bound to surfaces generate bulk fluid flow [142, 143]. Similarly, bacteria in racetracks, even though sliding along the PDMS interface, can generate fluid flows that reorganise cells in the bulk. A full analysis of fluid flow in experiments and simulations is presented in the next chapter.

## 2.4 Cross channels

Bacteria like *B. subtilis* often live in porous habitats created by the environment, like sand particles in soil, or by the bacteria themselves. For example, *B. subtilis* biofilms have been shown to form channels, 90 $\mu\text{m}$  in diameter [16]. Motile populations can then frequently encounter interfaces and confinement that affect their behaviour. However these environments are more complex than drops and racetracks and could consist of a network of such structures. In the fourth chapter of this thesis, I show how a bacterial suspension orders inside a lattice of vortices. Here, I briefly present results for 8-shaped channels and show how the circulation at the junction depends on its geometry.

### Setup

The bacterial suspension and the microchannels were prepared as in racetrack experiments (figure 2.11). Channels were 50 $\mu\text{m}$  in width, less than the critical width  $w^*$ , and were shaped in a figure of 8. The only changing parameter was the angle  $\varphi$  of incoming channels at the  $\times$ -junction (figure 2.20).

### Results

As in circular racetracks, the suspension quickly starts circulating and reaches steady state in about a minute. Bacteria can circulate in each branch either CW or CCW. The flow pattern at the junction is of particular interest.

If the circulation in each branch is in opposite direction, bacteria simply pass the junction without changing side (figure 2.20a).

If both branches circulate in the same direction, CCW for example, bacteria approach the junction from opposite sides, bottom left and top right on figure 2.20b,c. Depending on the angle  $\varphi$ , bacteria can follow different paths through the junction. If cells are moving from the bottom left channel,

- $\varphi = \pi/2$ : cells split equally to the top left and bottom right channels,
- $\varphi < \pi/2$ : cells predominantly go to the bottom right channel,
- $\varphi > \pi/2$ : cells predominantly go to the top left channel.

Thus, the path followed by the suspension is only dictated by the initial large scale circulation and by the angle  $\varphi$ , such that cells follow the steeper corner. Moreover, I observed that for the smallest angles  $\varphi$ , a stable vortex could form in the centre of the junction

Cachile *et al.* have studied the same setup in the case of a passive Newtonian fluid driven by pressure [144]. They came to the same conclusion: fluid predominantly follows the steeper angle (figure 2.20d-f). They also observed vortex formation at the centre of the junction but appearing at smaller angles than for bacteria:  $\varphi_{\text{fluid}} = 30^\circ$ ,  $\varphi_{\text{bacteria}} = 50^\circ$ . I have reproduced some of Cachile *et al.* results, as shown on the figure 2.20d-f, on FreeFem++, in collaboration with Pierre Haas, a PhD student in the group.

## Discussion

Measuring the flow cross section in racetracks has shown that bacteria diverge from the behaviour of passive fluids by generating various flow profiles from parabolic, double-peaked, to sinusoidal. This difference appears to depend on the way flows are generated, arising from the interfaces in the case of dense bacterial suspensions.

Yet, active and passive fluids display comparable streamlines at the junction of an 8-shaped channel, suggesting that flows are transmitted in the bulk in a similar fashion. This result indicates that the bacterial circulation might here be driven by the fluid flow they generate. Further experiments are necessary, measuring the fluid streamlines for different angles  $\varphi$  and channel width  $w$ , in order to reveal all bacterial flow states.

## 2.5 Conclusion

In this chapter, I have presented how confinement modifies the spontaneous motion of a dense suspension of *B. subtilis*. I have used an experimental approach and measured bacterial flow on a mesoscopic scale.

This approach has already given us valuable information on the suspension dynamics, the role of interfaces and how bacteria self-organise and can be stabilised by confinement in flattened drops, racetracks and 8-shaped channels. On one hand, previous experiments on dense bacterial suspensions have only considered unconfined 3D or quasi-2D chambers. On the other hand, simulations that have studied circular and

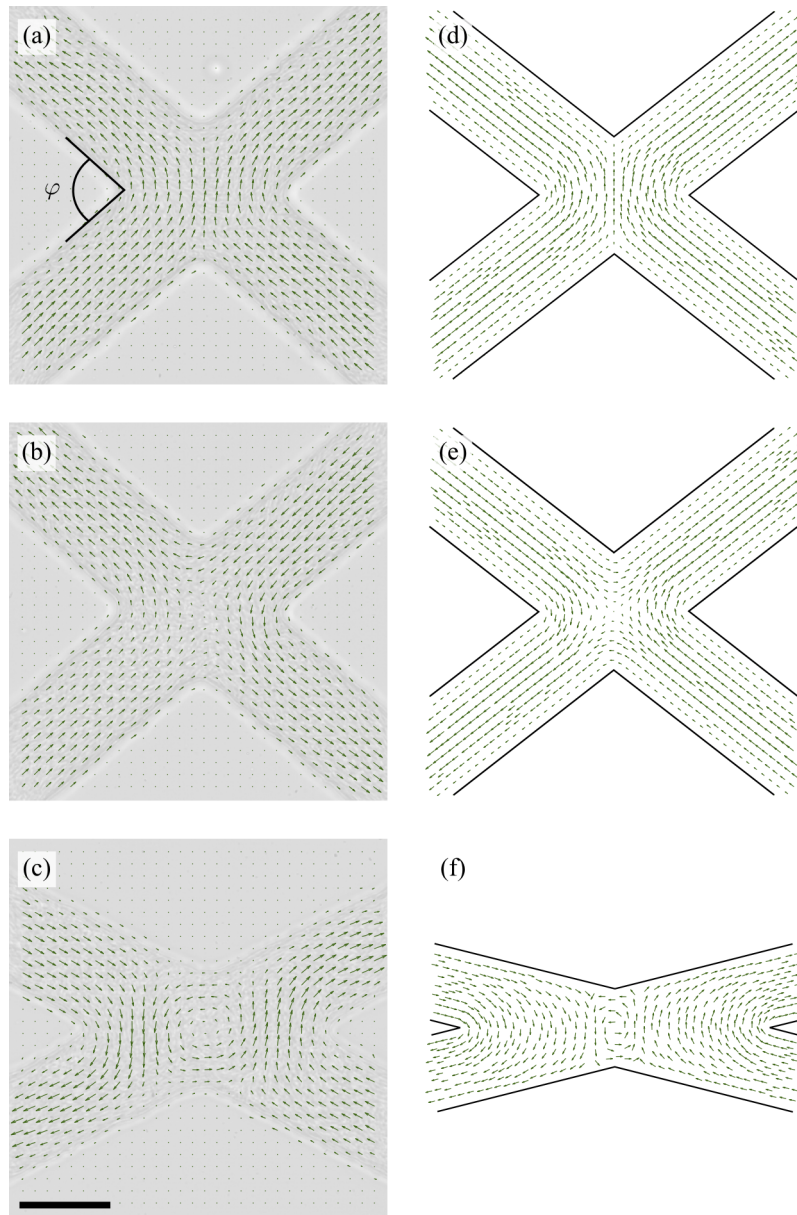


Figure 2.20: Flow at an  $\times$ -junction depending on the angle  $\varphi$ , (a-c) of a dense bacterial suspension and (d-f) of a passive Newtonian fluid. (a,d) Flow coming from bottom branches simply goes through the junction without changing side. (b,e)  $\varphi = 80^\circ$ , flow coming from opposite inlets and split almost equally between outlets. (c)  $\varphi = 50^\circ$  and (f)  $\varphi = 30^\circ$ , flow coming from opposite inlets follow the steeper corner, and forms a vortex in the centre of the junction. Bar and channel width:  $50\mu\text{m}$ . Arrows: bacterial and fluid flow, averaged over 10s in experiments. Arrow length is proportionnal to the velocity except in (f) where it is constant.

linear confinement have failed to predict the suspension dynamics.

My results thus bring fresh information on bacterial behaviour and more generally for the field of active matter. However, I have not explained yet how these organisations arise and in particular how the combined interactions between bacteria with one another and with the fluid leads to the observed flows.



## Chapter 3

# Bacterial Self-Organisation Mechanisms and the Role of Fluid Flows

### 3.1 Introduction

Active matter is a field dominated by theoreticians. They have proposed many approaches to model these systems and yet none has been able to predict countercirculating bacteria at interfaces or streaming patterns in racetracks. How is it possible that theories that claim to reproduce bacterial population dynamics without confinement, break down in the presence of interfaces?

An open question in the field is the role of fluid flows on the self-organisation of bacterial suspensions. Many models, mostly particle-based, still do not include them, arguing that they play a minor role. These models managed to reproduce most bacterial states (dilute, turbulent, jammed...) but also revealed behaviours that are not observed in large chambers (swarms). These simulations are actually more likely to reproduce the behaviour on agar plates, where fluid streams are limited to thin surface layer [44, 46]. On the other hand simulations that directly or indirectly include hydrodynamic interactions have neglected other aspects, such as steric interactions, self-propulsion, or boundary conditions. Finally no experiment has simultaneously measured the bacterial and fluid flows, and directly compared them (Wensink *et al.* have only looked at the

velocity distributions), most probably due to experimental limitations. We are therefore placed in a situation in which studies are not able to prove but merely suggest the mechanisms behind bacterial self-organisation.

This chapter is divided into two main sections. First, I will present a new method to experimentally estimate the local fluid flow direction and velocity, directly from the displacement of single bacteria. These results show that bacteria self-organise by the action of fluid flows that they generate.

In the second section, I will present a simulation method, proposed and mainly carried out by my collaborator Enkeleida Lushi. This model takes into account both direct steric and long-range hydrodynamic interactions, as well as the effect of interfaces. Results from the simulations give us a detailed description of the bacterial organisation from the microscopic to the macroscopic scale.

## **3.2 Experimental Observation of Fluid Flows**

### **3.2.1 Introduction**

Different groups (including Ray Goldstein's) have claimed that micron sized colloids, placed in dense bacterial suspensions, reflect the fluid rather than the bacterial flow. Yet no proof, that I am aware of, for such assertions has been given so far (for example, the bacterial flow and bead motion have not been simultaneously measured).

To measure fluid flows, beads has to be diluted compared with the bacterial concentration in order to limit the disturbance. Bead diameter then has to be at least  $0.5\ \mu\text{m}$  in size to avoid strong Brownian motion. However, this is also the typical size of bacteria (*E. coli* and *B. subtilis* are  $0.5$  and  $1\ \mu\text{m}$  in width, respectively). At high cell density, beads can thus be trapped between bacteria, if not directly sticking to one, in which case their motion would reflect predominantly the bacterial flow.

As I will show later, bacteria and the surrounding fluid can locally move in the same direction and at similar velocities. The error in measurement can be larger than the difference between flows, affecting the results' interpretation.

To avoid these issues I have developed a new method that allows me to simultaneously measure the motion (displacement) and the orientation (swimming direction) of single cells. Given that the motion of one bacterium results from swimming, advection

by the fluid, and direct steric interactions with other cells, one can deduce the local fluid flow direction and estimate its velocity.

### 3.2.2 Protocol

I used the mutant strain amyE::hag(T204C) DS1919 3610, grown in TB, under the same conditions as wild type bacteria (section 2.2.1). This mutant has been constructed in Daniel Kearns' lab [145] and is a gift from Linda Turner Stern. The gene *hag* that encodes the protein Flagellin, the main building block of the flagella, has been replaced by a version with a similar sequence except for a cysteine taking the place of a thiamine. This mutation does not affect the motility but allows for an efficient fluorescent labelling. I followed the protocol by Guttenplan *et al.* to label cells [48]: 1 ml of the suspension was centrifuged (1000 g, 2 min) and resuspended in 50  $\mu$ L of phosphate buffered saline (PBS) containing 5  $\mu$ g/mL Alexa Fluor 488 C5 Maleimide (Molecular Probes) and incubated at room temperature for 5 min. This fluorophore binds to the cysteine added to the flagella protein Flagellin. Bacteria were then washed in 1 mL PBS and resuspended in PBS containing 5  $\mu$ g/mL FM4-64 (Molecular Probes). This fluorophore incorporates itself into lipid bilayers and labels cell membranes. The excess of fluorophore was removed in a final wash and the suspension was resuspended into 50  $\mu$ L PBS. A fraction of the labelled mutants was then gently mixed with unlabelled wild type bacteria. *B. subtilis* does not swim in PBS because it lacks a carbon source. Once transferred back into TB, they quickly recover their motility.

Images were acquired on a spinning disc confocal microscope (Zeiss Axio Observer Z1) at 6 fps. Both fluorophores were excited at 488 nm and the emission was filtered using a GFP emission filter (barrier filter 500-550 nm, Zeiss) for Alexa Fluor 488 C5 Maleimide and a DsRed emission filter (barrier filter 570-640 nm, Zeiss) for FM4-64. I changed the filter between frames to alternatively visualise the cell body and the flagella. The frame rate is limited to 6 fps by the time it takes to switch between filters. Results are presented as a sequence of three frames: membrane (false coloured red), flagella (false coloured green) and again membrane (false coloured blue). Red and blue correspond to the same fluorophore, FM4-64, and reflect different time points.

### 3.2.3 Results

#### Low Density

The mutant amyE::hag(T204C) has been previously used to study the motility phenotypes [48]. Here, I propose and show that imaging flagella and body successively allows measurement of the orientation and motion of cells. I started with low density bacteria which weakly interact and are set into motion by swimming only. *B. subtilis* which are rod shaped, do not have permanent anterior (front) or posterior (back). The rear is defined as the rod-end where flagella form a bundle. Bacteria can revert this polarity, for example when hitting a surface [68].

I successively imaged the body (false coloured red in figures), flagella (false coloured green) and body again (false coloured blue). The motion of bacteria is deduced from the displacement of the body between the first and third frames. The orientation can be inferred from the bundling at the rear of the cell or from the average position of the body to the flagella.

As expected for a dilute suspension, the motion results from the self propulsion and cells exhibit a forward motion (figure 3.1).

#### Flattened Drops

I then mixed labelled bacteria into a dense suspension of wild-type cells and performed experiments in drops and racetracks as described in the previous chapter.

In the case of drops, I have already shown that the suspension self-organises into a spiral pattern, which indicates the orientation (geometric angle) but not the direction of the bacteria (position of the front and back). Two main hypothesis then arise (figure 3.2):

- Self-propulsion driven motion: cells in the bulk and at the interface swim in opposite direction, both with a forward motion.
- Advection driven motion: all cells are swimming in the same direction but advection by the fluid moves cells in the bulk against the boundary layer.

Due to the high cell density and the diffraction that results from it, fluorescent bacteria are more difficult to image in drops than in dilute suspensions. Yet, I managed

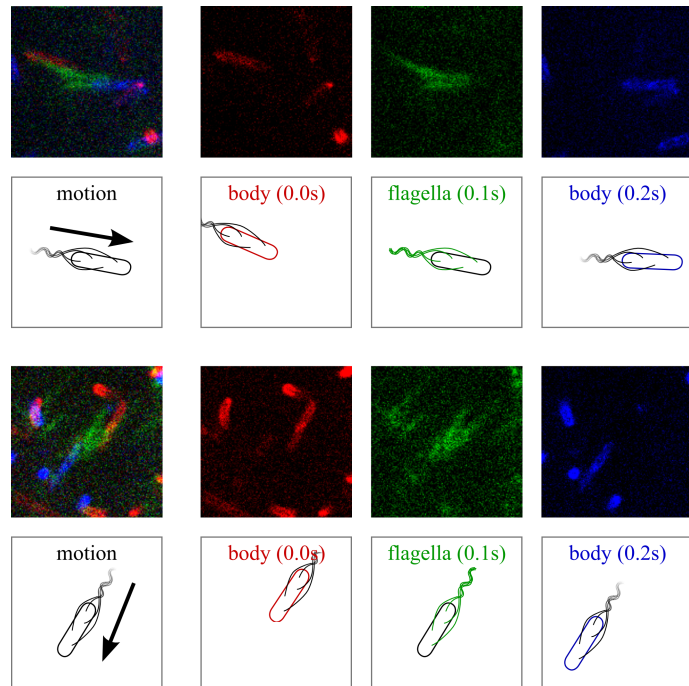


Figure 3.1: Forward motion of two fluorescent bacteria in a dilute suspension. Left-most: superimposed images of body (FM4-64, false coloured red), flagella (Alexa Fluor 488, false coloured green) and body again (false coloured blue). Top: bacteria moving from the left to the right side of the image. Bottom: bacteria moving from the top right corner to the bottom left. In both cases flagella bundle indicates the same swimming direction as the motion.

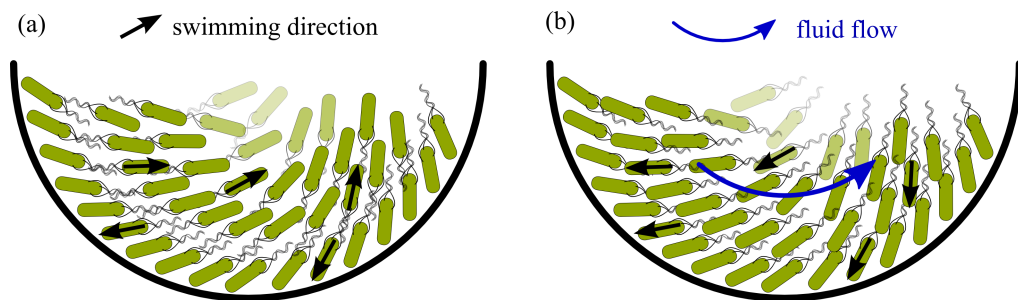


Figure 3.2: Two hypothesis for the drop organisation. (a) Cells in the bulk and at the boundary swim in opposite direction. (b) All cells swim in the same direction but cells are advected against their swim.

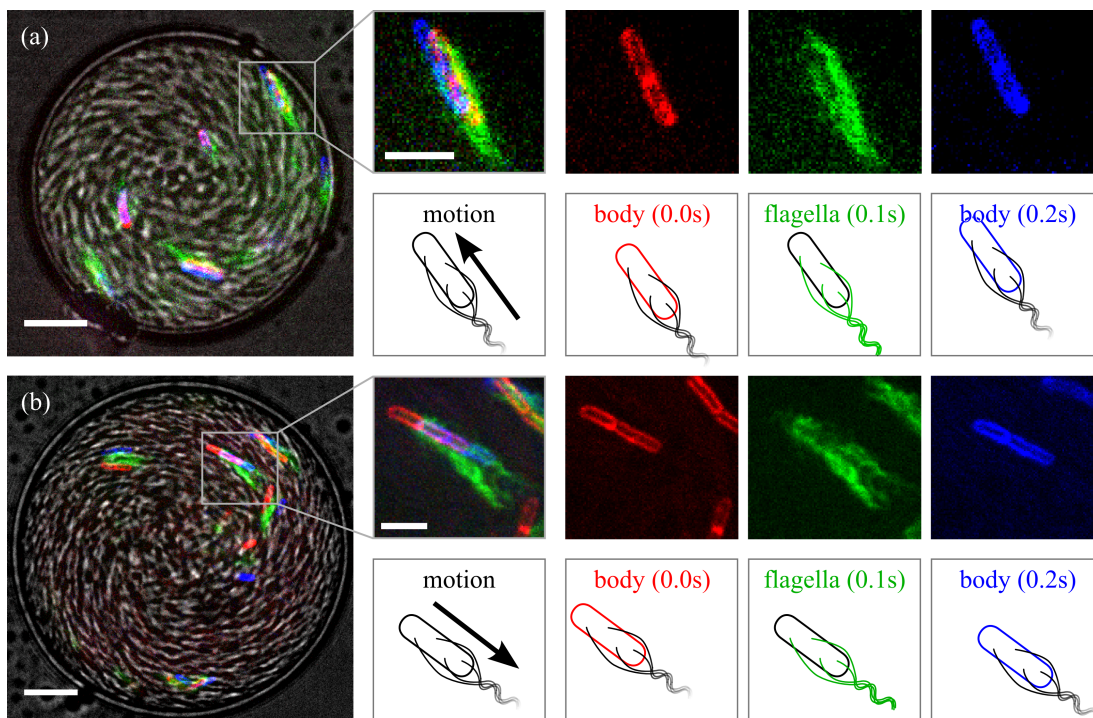


Figure 3.3: Fluorescent bacteria tracking in dense flattened drops. Leftmost image: superimposed images of body (false coloured red and blue), flagella (false coloured green) and bright field image (grey scale). (a) Cell at the oil interface has a forward motion, moving and swimming to the top left corner. (b) Cell in the bulk exhibit a backward motion, displacement of the body indicates that the cell move to the bottom right corner, while bundling reveals a swimming direction to the top left corner. Adapted from [2].

to track 24 cells, 16 of which were located in the bulk and 8 at the oil interface (which is resolved from bright field images, figure 3.3).

I found that all cells at the interface perform a forward motion, moving in the same direction as their swimming. In contrast, cells in the bulk travel against their swimming direction showing that the fluid flow generated by the suspension was responsible for the bulk circulation. Collisions between cells might also contribute to the overall motion. However, since all cells are swimming in the same direction, steric interactions are most probably responsible for the local alignment and cell density, but cannot explain the macroscopic forward or backward motion.

Therefore, these results support the second hypothesis: all cells are swimming in

the same direction but long-range hydrodynamic interactions advect cells in the bulk against the boundary layer. In the bulk, the fluid flows can then be estimated as the sum of the bacterial flow and the single cell swimming speed  $\approx 5\mu\text{m/s}$ . The azimuthal flow profiles measured in the previous chapter showed bacterial flows up to  $50\mu\text{m/s}$  and I measured local flows up to  $100\mu\text{m/s}$ , showing that, except close to the oil interface, the flow is hugely dominated by advection.

### **Racetracks**

I then performed the same experiment in racetracks, which equally exhibit a layer of bacteria at the PDMS interface moving against the bulk circulation. I used 35 to  $45\mu\text{m}$  wide channels, displaying a strong stream (normalised net flow  $\Psi > 0.7$ ) with limited perpendicular flow  $u_y$ .

I tracked 26 cells, 2 at the interface and 24 in the bulk. Both cells at the interface moved against the bulk circulation, as indicated by bright field images (figure 2.13), and performed a forward motion (identical swimming and motion directions). Among cells in the bulk, 4 were aligned perpendicular to the flow, 4 were swimming with the flow and a large majority of cells, 16, were swimming against the flow (backward motion, figure 3.4). Suspensions in racetracks are more turbulent than in flattened drops, which would explain why not all cells are swimming in the same direction.

### **3.2.4 Discussion**

Results in flattened drops and racetrack chambers are consistent: while cells share a common biased direction, they generate fluid flows, up to an order of magnitude faster than the single cell swimming speed, advecting cells in the bulk against the suspension swimming direction, leading to the formation of the countercirculating boundary layer.

Sokolov *et al.* [31] have previously measured the orientation, but not the direction, of cells without confinement. They imaged the suspension in bright field but could not visualise flagella. In dense suspensions, they found the cell orientation to be isotropic and independent of the flow direction. This result already showed that self-propulsion was not the main contribution to the cell motion. Indeed, steric repulsion between swimmers could also play a strong role. However, in racetracks and even more so in flattened drops, cells locally share the same swimming direction. Steric interaction

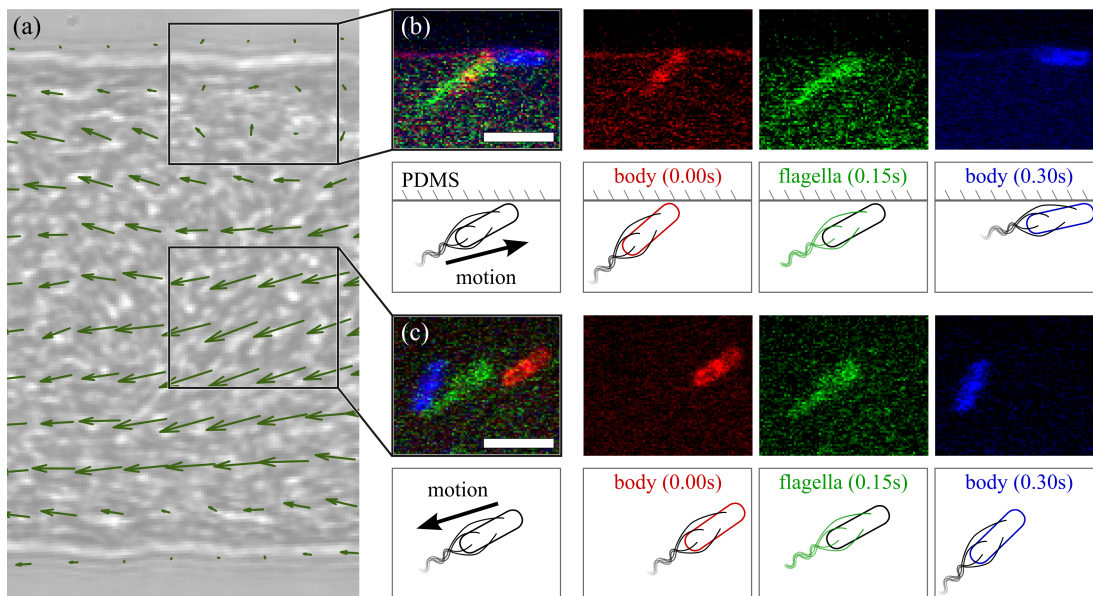


Figure 3.4: Fluorescent bacteria tracking in dense racetracks. (a) Bright field image of a racetracks. Arrows: bacterial flow measured by PIV, not all measurements are shown. (b) Forward motion at the PDMS interface. Both swim and motion are directed to the right side. (c) Backward motion in the bulk. The cell moves to the left side of the image, while bundle indicates a swimming direction to the top right corner. Adapted from [3].

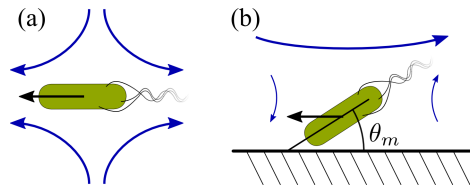


Figure 3.5: Effect of an interface on the bacteria generated fluid flow. (a) Unconfined bacteria: the stresslet creates a 'pusher' disturbance, fluid is symmetric, coming from the side and propelled at the front and back. (b) No-slip boundary condition breaks the symmetry to generate a net fluid flow against the swimmer direction. Black arrows: bacteria motion. Blue arrows: fluid flow.

then mostly appears to align cells, akin to nematic liquid crystals. This phenomenon might as well ensures that all cells locally move at the same speed but is unlikely to substantially contribute to the overall motion.

Advection then seems to be leading bacterial flow. Left to be understood is how bacteria generate fluid flows against their swimming direction, when stresslet disturbance is symmetric. Figure 3.5 presents a diagram of a cell at an interface, at an angle  $\theta_m$  (as also defined in drops). The interface breaks the symmetry, producing a net flow in the bulk, moving against the cell swimming direction.

Finally, many simulations that aimed to reproduce dense bacterial suspensions have neglected hydrodynamic interactions [7, 90, 99]. My results show that the fluid plays a major role in the suspension circulation and that circulation in drops and racetracks cannot be understood without considering the fluid flows. To understand in more details how the suspension self-organises, I now present a simulation model that includes self-propulsion, steric as well as hydrodynamic interactions.

## 3.3 Simulation

### 3.3.1 Model

Bacteria are represented as elongated ellipsoids, of centre of mass  $\mathbf{X}_i(t)$  and orientation  $\mathbf{P}_i(t)$ . Each swimmer moves by self-propulsion, direct repulsion and torque with neighbours, advection and reorientation by the fluid flow. Fluid is set into motion by the bacteria only, through a classical stresslet model. Finally, we take into account boundary conditions using a system of images.

## Bacterial Motion

The motion and reorientation of a swimmer is dictated by the following equations

$$\partial_t \mathbf{X}_i = U_0 \mathbf{P}_i + \mathbf{v} + \Xi_i^{-1} \sum_{j \neq i} \mathbf{F}_{ij}^e, \quad (3.1)$$

$$\partial_t \mathbf{P}_i = (\mathbf{I} - \mathbf{P}_i \mathbf{P}_i^T) (\gamma \mathbf{E} + \mathbf{W}) \mathbf{P}_i + k \sum_{j \neq i} (\mathbf{T}_{ij}^e \times \mathbf{P}_i), \quad (3.2)$$

where  $U_0 \mathbf{P}_i$  denotes the self-propulsion with constant speed  $U_0$  in the swimming direction  $\mathbf{P}_i$ ,  $\mathbf{v}$  the advection by the fluid flow and  $\mathbf{F}_{ij}^e$  the steric repulsion between swimmers. Cells are then reoriented by shear flow [82], with  $2\mathbf{E} = \nabla \mathbf{v} + \nabla \mathbf{v}^T$ ,  $2\mathbf{W} = \nabla \mathbf{v} - \nabla \mathbf{v}^T$  and  $\gamma \approx 0.9$  for ellipses with aspect ratio 4, and by steric interactions with torque  $\mathbf{T}_{ij}^e$ .

To estimate the steric interactions  $\mathbf{F}_{ij}^e$  and  $\mathbf{T}_{ij}^e$ , swimmers are represented as a set of circular beads, which interact with neighbouring swimmers through a Lennard-Jones potential [140].  $\Xi = m_{\parallel} \mathbf{P}_i \mathbf{P}_i^T + m_{\perp} (\mathbf{I} - \mathbf{P}_i \mathbf{P}_i^T)$  with the mobility parameters  $m_{\perp} = 2m_{\parallel} \approx 2$ , and  $k \approx 5$  for ellipses.

There is no noise term and neither Brownian motion nor run-and-tumble behaviour are taken into account.

## Fluid Flow

The fluid flow is estimated by summing the contribution of each single swimmer into a classical Stokes equation,

$$-\nabla^2 \mathbf{v} + \nabla q = \nabla \cdot \sum_i \mathbf{S}_i^a \delta(\mathbf{x} - \mathbf{X}_i), \quad (3.3)$$

$$\nabla \cdot \mathbf{v} = 0, \quad (3.4)$$

where  $q$  is the fluid pressure to account for the fluid incompressibility and  $\mathbf{S}_i^a = \alpha \mathbf{P}_i \mathbf{P}_i^T$  the active stress tensor resulting from the swimmer locomotion in 2D with non-dimensional stresslet strength  $\alpha \approx -1$  for a pusher swimmer of normalised length  $\ell = 1$  and velocity  $U_0 = 1$  [146].

These equations do not take into account the presence of a dense suspension: the overall fluid flow generated by bacteria is simply the sum of the fluid flow created by each single swimmer in an empty medium, as if the medium could move through

neighbouring bacteria. Computing the fluid flow  $\mathbf{v}$  around a suspension of bacteria would require much larger computation power and probably would not be achievable in a reasonable time. Yet we expect the result to be at least qualitatively similar, as swimmers occupy 5 to 20% of the volume in experiments.

### Domain and Boundary Conditions

Simulations are performed in 2D domains for two reasons. First, experimental chambers are usually low enough to have a predominantly horizontal motion (with the notable exception of the smallest drops). Secondly, computing in 2D significantly reduces the computation time.

Interfaces are reproduced using a system of images, mirrored on the other side of the interface. In the case of circular confinement of radius  $R$ , if a swimmer is placed at a distance less than  $3\ell$  from the interface, an image is added, at a distance  $R^2/|\mathbf{X}_i - \mathbf{X}_{\text{centre}}|$  from the centre and with orientation  $\mathbf{P}_i - 2(\mathbf{X}_i - \mathbf{X}_{\text{centre}})/|\mathbf{X}_i - \mathbf{X}_{\text{centre}}|$  [120].

Periodic channels that reproduce the straight part of racetracks are made into a periodic domain  $(x, y) \in ([0, L], [-w, w])$ , with mirrors at  $y = 0, w$ . Images of all swimmers are placed at position  $\mathbf{X}_i - 2(\mathbf{X}_i \cdot \mathbf{e}_y)\mathbf{e}_y$ , with orientation  $\mathbf{P}_i - 2(\mathbf{P}_i \cdot \mathbf{e}_y)\mathbf{e}_y$ , creating the boundary condition for both PDMS interfaces simultaneously.

Steric interactions and fluid flows are computed by taking into account these swimmers. Through direct repulsion, the system of images ensures that bacteria do not cross interfaces and approximates a free-slip boundary condition for the fluid. This condition is not perfectly suitable to model oil and PDMS interfaces. The latter requires a no-slip boundary condition. Given its large viscosity, oil has a strong resistance to motion under such confinement (the motion of oil around drops is much slower than that of the suspension). Computing more realistic boundary conditions necessitate to use a more complex image system [77] and a greater computation power. However, I do not expect this approximation to qualitatively change the result of the simulation, except for the boundary layer thickness, as explained below.

### 3.3.2 Results

Enkeleida Lushi performed simulations in unconfined circular and straight periodic channels. She managed to reproduce the different behaviours observed experimen-

tally. These results help in understanding how the bacteria self-organise and in particular confirm the mechanism forcing bulk bacteria to move against the boundary layer. Note that we have not done any parameter fitting and all values (swimmer aspect ratio, generated flows...) are either normalised or taken from the literature.

## Reproducing Experimental Results

Before we actually analysed the simulation in order to understand the bacterial self-organisation, we made sure they could reproduce the different bacterial motions observed *in vitro*.

Lushi first simulated bacteria under circular confinement. She was able to obtain the double circulation, peripheral bacteria moving in opposite direction to the centre (figure 3.6). She measured the vortex order parameter  $\Phi$  and found as in experiments that swimmers stop forming a single vortex state around  $d_+^{\text{simu}} \sim 17\ell$ .  $d_+^{\text{simu}}$  can be matched to experimental measurements by choosing  $\ell \approx 4\mu\text{m}$ , which is slightly shorter than the actual *B. subtilis* length of 5 to 7  $\mu\text{m}$ . Likewise she also found that the vortex order parameter remains high in semi-dilute suspensions, even for diameters larger than  $d_+^{\text{simu}}$  (figure 3.6).

For the smallest diameters, less than  $d_-$ , the unstable 3D circulation observed *in vitro* could not be reproduced since simulations are performed in 2D. Instead,  $\Phi$  decreases when the diameter is less than  $6\ell$  and bacteria do not have enough space to move.

The main difference between simulations and experiments appears in the thickness of the counterrotating boundary layer. In experiments, I measured a constant boundary width  $l_b \approx 4\mu\text{m}$ , consisting of a single layer of bacteria. In simulations, we found up to three layers of swimmers, moving against the central circulation (figure 3.7). This discrepancy may be due to the inaccuracy of parameters which we did not fit. Another likely explanation comes from the inaccurate boundary condition. Simulations assume no-slip at the oil interface, allowing for the fluid flow direction to revert at the edge of the drop (figure 3.6): bacteria are advected with their swimming direction over a few layers. Instead if a no-slip boundary condition was used, the fluid flow would be negligible at the oil interface, reducing the number of cells moving against the bulk.

Furthermore, confinement in straight periodic channels reproduced the overall race-

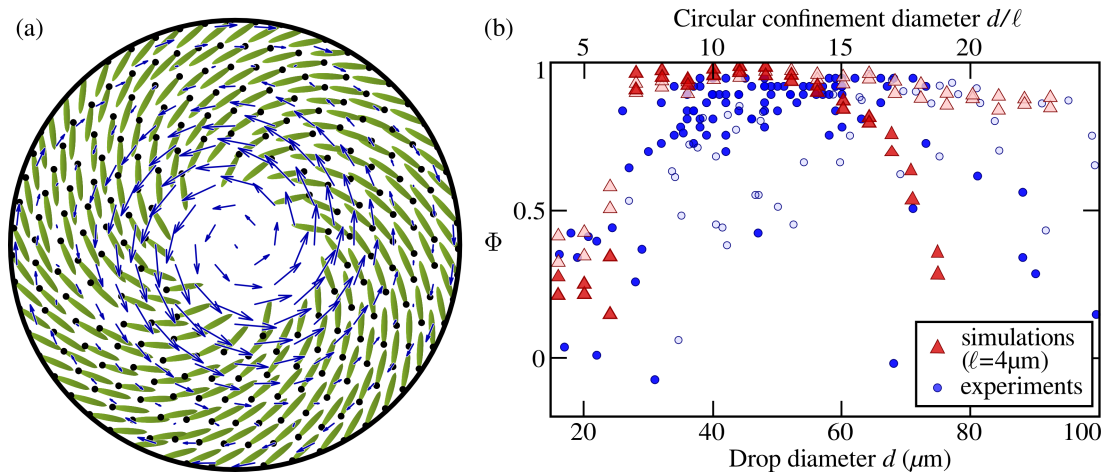


Figure 3.6: Simulations reproduce the bacterial motion under circular confinement. (a) Simulation steady state. Arrows: fluid flow. (b) Vortex order parameter  $\Phi$  in simulations (triangles) and experiments (circles) with dense (full symbols) and semi-dilute suspensions (empty symbols). Adapted from [2]

track circulation. In this geometry, boundary bacteria moving against the bulk formed a single layer of swimmers, in agreement with experiments. Lushi measured the net flow and obtained a transition from streaming to an overall stationary behaviour, for  $w_{\text{simu}}^* \approx 17\ell$  (figure 3.7).  $w_{\text{simu}}^*$  can be matched to experimental measurements by setting  $\ell \approx 4 \mu\text{m}$ , which as in drops, is smaller but still comparable to *B. subtilis* length, 5 to  $7 \mu\text{m}$ .

In addition, Lushi also measured the bacterial flow cross section  $F(y)$  for varying channel width and reproduced the different behaviours, from parabolic to sinusoidal profiles (figure 3.7). Remarkably, since bacteria at the boundary move against the bulk, she obtained negative flows at  $y = 0, w$ . This result is also expected for experiments but the PIV resolution was here too low to capture the bacterial motion at the interface.

### Self-Organisation and Hydrodynamics

We then studied in more detail how fluid flows affect and drive the suspension motion. Over experiments, simulations have the advantage that we can easily add or exclude hydrodynamic interactions and directly measure their effect. Before studying the confined state, Lushi simulated bacteria in a periodic domain. As described in previous publication without fluid flow [7], bacteria form swarms: aggregates that travel in a

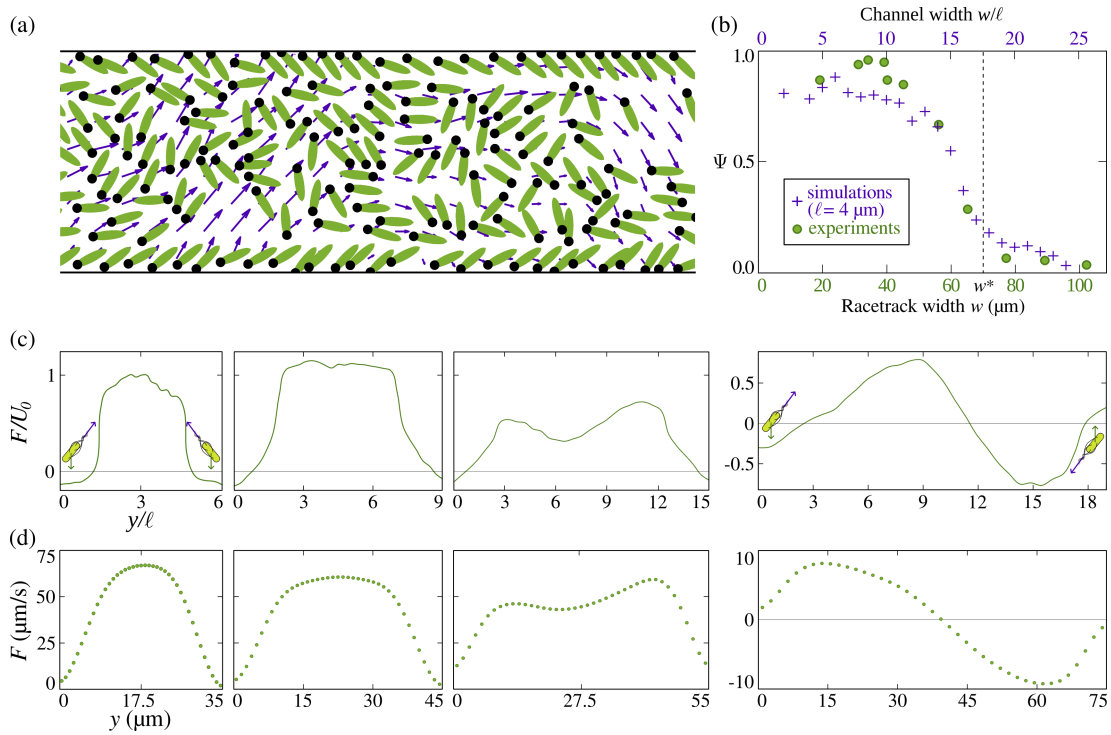


Figure 3.7: Swimmer self-organisation in periodic channels. (a) Simulation steady state. Swimmers (green ellipses, black circles indicate the front) generate fluid flows (purple arrow) which advect bulk swimmers against the boundary layer. (b) Normalised net flow  $\Psi$  depending on the channel width  $w$  in simulations and experiments. Simulations are averaged over a time  $5U_0/\ell$  and experiment over at least 5 movies.  $\ell$ : swimmer length.  $U_0$ : single cell swimming speed. (c,d) Averaged bacterial flow profile in simulations and experiments. All three plots on the left share the same y-axis. Sketches of swimmers indicate the cell orientation and swimming direction at the boundary (green arrows), as well as the fluid flow they generate (purple arrows).

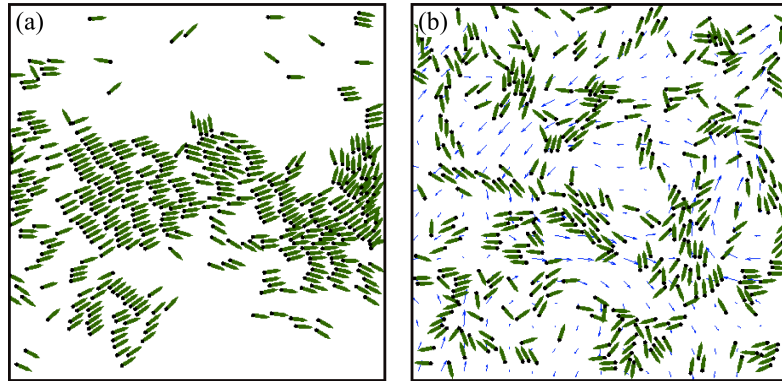


Figure 3.8: Swimmer self-organisation in simulations with periodic boundary conditions. (a) Without hydrodynamic interactions, swimmers collectively move in a large swarm. (b) Adding fluid flows (blue arrows) generated by swimmers, disassemble the swarm and leads to the formation of a turbulent state. Adapted from [2].

collective fashion. This behaviour has been observed experimentally for *swarming* bacteria on agar plates (as opposed to *swimming* bacteria). Yet such an organisation has not been found in 3D or quasi-2D chambers. Adding hydrodynamic interactions in Lushi’s simulations disrupts these aggregates to form a more homogeneous suspension (figure 3.8).

To fully understand the self-organisation of bacteria under circular confinement, Lushi not only included or excluded hydrodynamic interactions but also changed the swimmers’ shape (figure 3.9). In the following, I list the different parameters and results we tried:

- Elongated swimmers with fluid flow: the most realistic case, which reproduced the circulation as observed *in vitro* (figure 3.9a).
- Elongated swimmers without fluid flow ( $\alpha = 0$ ): bacteria assemble into a single vortex but fail to form the counterrotating layer (figure 3.9b). This motion matches that of elongated robots [39, 40].
- Circular swimmers with fluid flow ( $\gamma = 0$ ,  $\mathbf{T}_{ij}^e = 0$ ): bacteria are fully circular and do not align by steric or hydrodynamic interactions (figure 3.9c). Few transient circulation was observed.
- Semi-circular swimmers with fluid flow ( $\gamma \approx 0.9$ ,  $\mathbf{T}_{ij}^e = 0$ ): swimmers react dif-

ferently depending on the interaction type. They are circular for steric (they do not align like liquid crystals) but elongated for hydrodynamic interactions (they are reoriented along shear flow). This case may correspond to spherical bacteria whose flagella act as a ghostly tail. Such species have been shown to exhibit collective motion similar to rod-like bacteria, such as *E. coli* and *B. subtilis*, but have not been studied under confinement [136]. Simulations under circular confinement show clear circulation, with counterrotating boundary layer (figure 3.9d). Hydrodynamics are here sufficient to organise and drive the bacteria motion.

These different cases show that fluid flows are not only necessary but they are also sufficient to reproduce and understand the bacterial circulation.

Figure 3.10 presents the evolution of a bacterial suspension over time from a random disordered state to a single vortex. Swimmers were found to first organise at the boundary from which they create a strong bulk fluid flow, moving in the opposite direction to their swimming. This flow advects bacteria in the bulk before they organise into a spiral pattern. Eventually, all cells share the same swimming direction but due to advection, the bulk moves against the boundary layer. Moreover, simulations of semi-dilute suspensions show that forces generated by the boundary layer are sufficient to generate strong bulk fluid flow (figure 3.9e).

I also reproduced the emergence of order in flattened drops by exposing bacteria to a blue light, to which they react by switching to a tumbling state, disorganising the suspension [147].<sup>1</sup> Once the light is switched off, cells recover their swimming behaviour. As in simulations, bacteria first organise at the oil interface, setting into motion the bulk before it is fully ordered (figure 3.10).

Finally, Lushi studied swimmers under linear periodic confinement, this time only adding or excluding hydrodynamic interactions. She came to the same conclusion: bacteria at the interface drive the bulk circulation through strong fluid flows. Swimmers likewise possess a biased swimming direction against the fluid flow, as found with fluorescent bacteria. Yet, swimmers in the bulk are much less ordered than in drops, in contrast to those at the boundary which generate most of the fluid flow.

<sup>1</sup>I discovered this effect when imaging fluorescent mutants. It has been reported previously [147] but I am not aware of any other paper using this method in dense bacterial suspensions. Lu *et al.* instead used a photosensitiser that produces reactive oxygen species and alter bacterial motion [148].

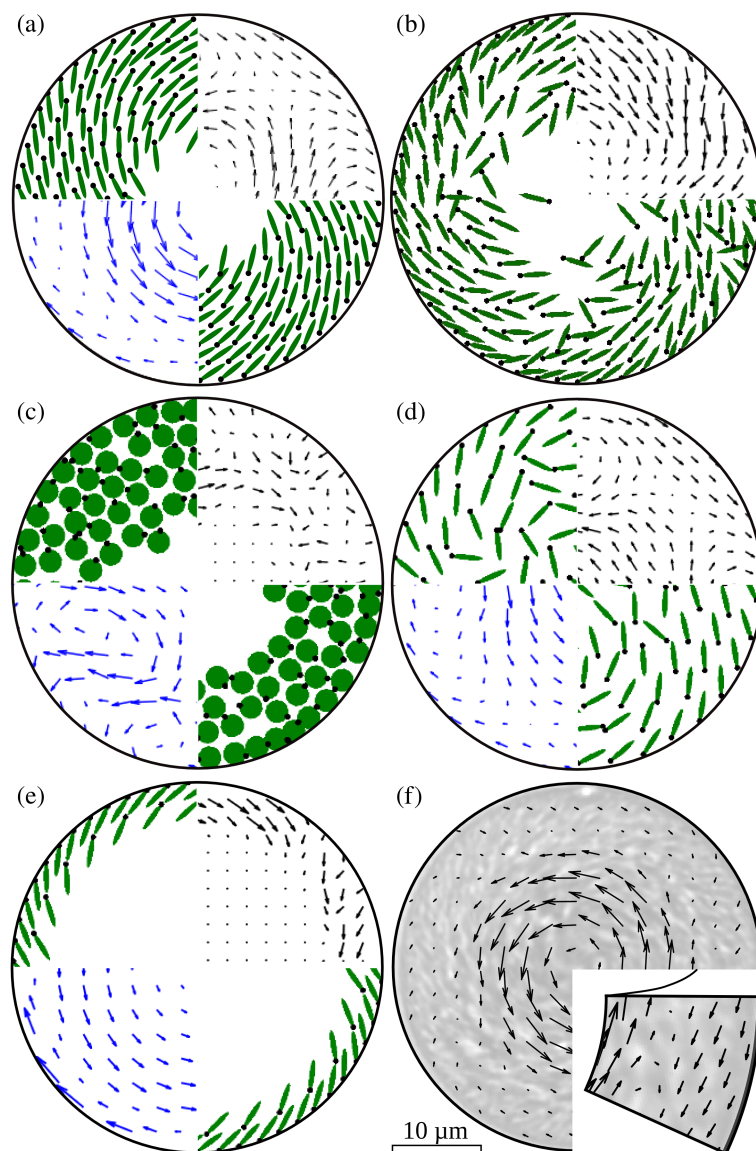


Figure 3.9: Self-organisation under circular confinement depending on interactions, shape and density of swimmers. (a) Elongated swimmers with hydrodynamic interactions. (b) Elongated swimmers without fluid flow. (c) Circular swimmers. (d) Circular swimmers for steric interactions but align with shear flow. (e) Dilute suspension of elongated swimmers. (f) Bacterial flow as measured in experiments. (a, c-e) Blue arrows, lower-left quadrant: fluid flow. Arrows are magnified 1, 5, 1, 2 fold respectively. (a-e) Black arrows, top-right quadrant: bacterial flow. Arrows are magnified 1.2, 4, 13, 1.2, 1.2 fold respectively. Adapted from [2].

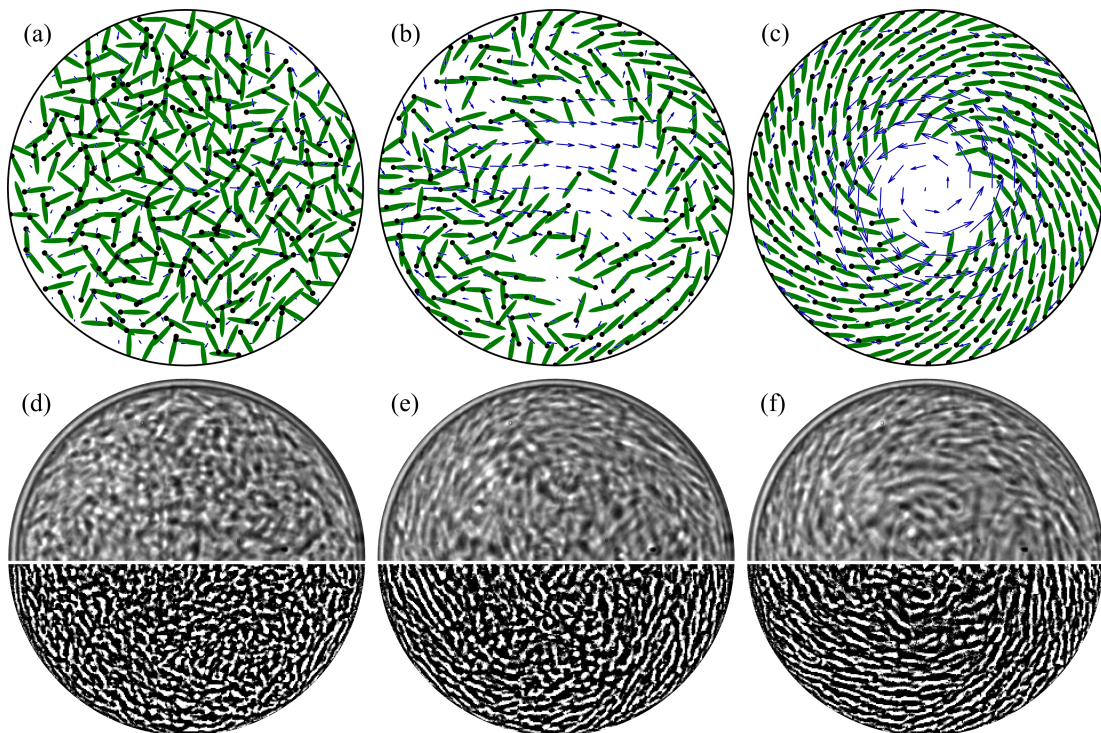


Figure 3.10: Self-organisation in flattened drops from a disordered state. (a-c) Simulations. Blue arrows: fluid flow. (d-e) Experiment. The lower half is obtained by an edge detection filter and contrast improvement. Adapted from [2].

### 3.3.3 Discussion

#### Simulations vs. Experiments

Simulations were in strong agreement with experimental results, reproducing the bacterial motion with and without confinement and validating the model of fluid flow driven circulation. Flattened drops and racetracks are set into motion by the same mechanism, in which most bacteria point in a common direction and generate backward fluid flows. Due to the boundary condition, these flows are faster in the bulk where advection becomes stronger than the single cell swimming speed, resulting in the countercirculating layer observed in both flattened drops and racetracks.

Hydrodynamic interactions also had a strong effect on unconfined suspensions. Simulations without fluid dynamics predicted a phase separation with dense bacterial clusters, 'swarms', and very dilute regions. This state has not been observed experimentally in large chambers and disappears when hydrodynamics are added to simulations. Fluid flows break apart clusters, resulting in a more homogeneous suspension. We have not quantitatively studied this effect - since we wanted to focus on drops and racetracks - but it has also been reported in the context of squirmers by Matas *et al.* [91]. This effect appears universal among microswimmers.

#### When Can Hydrodynamics Be Neglected?

Numerous continuum models and particle-based simulations have aimed to reproduce the motion of microswimmers. Even though several studies have shown hydrodynamics to strongly modify population-level behaviour, they are still neglected in many articles. In particular a phase diagram of bacterial motion state has been proposed depending on the cell volume fraction and aspect ratio. Wensink *et al.* for example have identified swarming and laning phases, appearing without fluid. Yet these states have not been observed in 3D or quasi-2D chambers, which they aim to model.

Among all motility mechanisms, biologists have described distinctively swimming and swarming [44]. They are both actuated by flagella but swimming refers to a motion in a 3D volume ('suspension'), while swarming, that on agar plates. In the latter case, bacteria produce surfactants that create a liquid film on the agar surface [46]. The layer of fluid at the surfaces can be very thin, strongly dampening fluid flows. Furthermore, surface tension at the edge of each swarm can promote their aggregation. Swimming

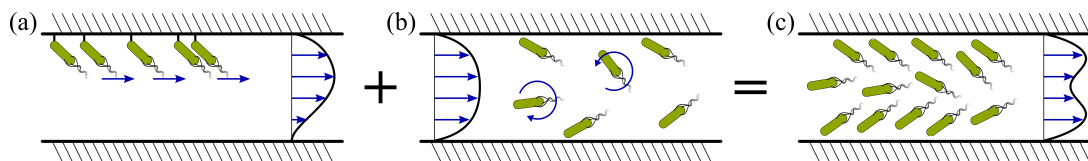


Figure 3.11: Mechanism for bacterial circulation decomposed into two previous experiments. (a) Bacteria glued to a surface generate flows into the bulk, against their swimming direction. (b) Swimming bacteria reorient and accumulate at the surfaces by the action of a shear flow. (c) Self-organisation in racetracks, through long-range hydrodynamic interactions. Blue arrows: fluid flow.

and swarming bacteria are then quite different systems which should be distinguished and modelled carefully.

### Previous Experiments

I am not aware of any publication reporting the arrangement of bacteria observed in flattened drops and racetracks, in which the self-propulsion and advection create the mentioned double circulation pattern. However, my experimental results can be understood as a combination of previous experiments (figure 3.11).

First, different teams have attached swimming bacteria to surfaces, coordinating their orientation and producing overall motion. Darnton *et al.* showed that these bacteria create fluid flows in the surrounding medium and when attached to small particles, would propel them [142]. Likewise Kim *et al.* covered walls of microfluidic channels with swimming bacteria and managed to use swimmers to generate a pump [143]. Cells push fluid in and out of the channel, setting up a net stream comparable to that in thin racetracks.

Secondly, bacteria have often been studied in microchannels, but in a dilute regime. Experiments showed that bacteria accumulate at the surfaces. When a shear flow is then imposed, bacteria are not only advected but also reoriented against the fluid flow, leading to upstream motion, as observed in flattened drops and racetracks.

### Previous Simulations

Several previous theoretical studies have considered confinement, either circular or in periodic channels, but none has been able to predict the behaviour I observed, and in

particular the boundary layer moving against the bulk flow.

As an inspiration for my experiments, Francis Woodhouse's simulations of *Chara* extracts, predicted a single vortex state with a spiral pattern, yet without the countercirculating boundary layer [131]. Indeed, he simulated an active system driven by stresslet perturbations but did not include self-propulsion. He then correctly modelled the orientation of bacteria and the fluid flows they generate. The double circulation can then be restored by adding a swimming term, directed against the fluid circulation. At the edge, the fluid flow becomes weaker than the cell velocity, creating the boundary layer.

Several continuum models have studied periodic channels, yet without predicting the circulation and flow patterns in the bulk. The following two models used active nematics (Q-tensor) theory to represent the active matter. Ravnik *et al.* [103] analysed short periodic channels and thus could not capture the formation of partial swirls. Instead, they predicted vortex-like circulation with the axis of rotation along  $\mathbf{e}_x$ . Unfortunately these flows were 1-2% the magnitude of the overall stream. Such a weak component is overcome by noise and turbulence in experiments and cannot be measured. Fielding *et al.* [105] studied the circulation depending on the size of the swirls relative to the channel width. Surprisingly they found opposite results to my experiments: streaming appears only when the channel is much larger than the vortex size.

Likewise, Costanzo *et al.* simulated dense suspensions of swimmers in periodic channels, using a particle-based model [140]. They considered the system with and without added external fluid flow, and showed that this flow is necessary to obtain a collective motion of the suspension, in contradiction to simulations presented in this thesis. This difference may arise from the fact that Costanzo *et al.* did not take into account the interface to compute the fluid flow (there are only steric boundary conditions in their model), suggesting that mirror swimmers in Lushi's simulations increase the hydrodynamic interactions, leading to the suspension organisation.

### 3.4 Conclusion

Physical sciences is a domain built around universal laws and minimal models. Theoreticians working on active matter are almost exclusively physicists or applied mathematicians and imported this approach to study these systems. Yet active matter is ex-

tremely diverse, in particular concerning interaction mechanisms, such as direct steric repulsion, long-range fluid flows, and more complex behaviours including visual clues in birds.

As a result, the most common model, Vicsek's, and its coarse-grained counterpart, Toner-Tu, seek to study active matter simply by assuming a local alignment mechanism between its constituents. In the quest for minimality, the complexity of active systems has been left behind and these models only capture few experimental behaviours. Regarding dense bacterial suspensions for example, many simulations have neglected fluid flows. Yet such an approach is only relevant for some swarming bacteria or for vibrated objects.

To disprove this model in the case of confined and unconfined suspensions, I have shown using fluorescently labelled bacteria, that fluid flows are crucial to understand cell motion. Enkeleida Lushi's simulation is not the first, but still one of few, to fully take into account self-propulsion, steric interactions between ellipsoid swimmers and the fluid flow they create. Moreover, she includes boundary conditions for both fluid and swimmers, through a system of images.

She then presented a minimal model that can still reproduce all particularities of this active suspension. We obtained a detailed understanding of the dense bacterial suspensions under confinement, confirming that fluid flows, predominantly generated next to interfaces, drive the overall motion.

# Chapter 4

## Lattice of Vortices

### 4.1 Introduction

Swimming bacteria are a powerful model system for active matter theories. *B. subtilis* are easy to prepare and use: cells grow quickly, are resistant to centrifugation and chemical treatment, and the large variety of species and mutants allows to vary experimental parameters.

Despite the apparent simplicity, the various behaviours they exhibit can be quite complex, due to the combination of direct steric and long-range interactions. Experiments in confined chambers have shown unexpected dynamics and more are likely to be discovered. In this chapter, I present a setup that differs from natural habitats but brings new ideas to active matter theories.

When a dense suspension of swimming bacteria is confined to a flattened drop, it spontaneously forms a single stable vortex, spinning CW or CCW with equal probability. If such vortices are brought close to one another, one can expect some interaction to couple the directions of these vortices.

In the simplest case of two vortices, interacting through a given region called *gap* (figure 4.1b), bacteria can be expected to move in the same direction in this gap, leading to opposite vortices.

Experiments are performed in three different arrays of vortices (lines, square and triangular lattices, figure 4.1c,d). Calculations of the mean absolute spin and of the spin-spin correlation reveal four distinct states (random, antiferromagnetic, ferromag-

netic and disordered) that depend on the lattice topology and on the cavities geometry. Finally, I present an Ising model that describes the network order and gives insights into the mechanism driving the bacterial dynamics.

## 4.2 Experiments

### 4.2.1 Protocol

Wild type *B. subtilis* were grown in TB, as for flattened drops and racetracks (section 2.2.1), and concentrated by centrifugation. Chambers were prepared in PDMS (section 2.3.1), their design probably being the most challenging part of these experiments.

#### Microchambers

Chambers were about  $18\mu\text{m}$  in height, and formed a lattice of flat circular cavities connected by gaps (figure 4.1b). The distance between cavity centres was set to  $60\mu\text{m}$  (cavities were about  $50\mu\text{m}$  in diameter) and I varied the topology of the lattice (line, triangular, square, figure 4.1c,d) as well as the gap size (4 to  $20\mu\text{m}$ ).

All plots shown here have been obtained using these geometries. I also tried numerous other lattice sizes (smaller and larger cavity diameters, gap depths, chamber heights, etc), which behaved in a qualitatively similar way.

#### Imaging

The suspension was injected into the lattice and both inlets were sealed to prevent external flows. I imaged the suspension using a  $40\times$  oil-immersion objective on an inverted microscope (Zeiss Axio Observer Z1), recording at 60fps for 10s (Photron Fastcam), 4 and 8 minutes after injection. The lattices were typically 15 cavities large, but I only imaged a  $6\times 6$  cavities region, taken in the centre of the chamber to avoid boundary effects. I also avoided recording ill-filled cavities which could be semi-diluted or in a jammed state. However, I did not choose specifically well-ordered lattices.

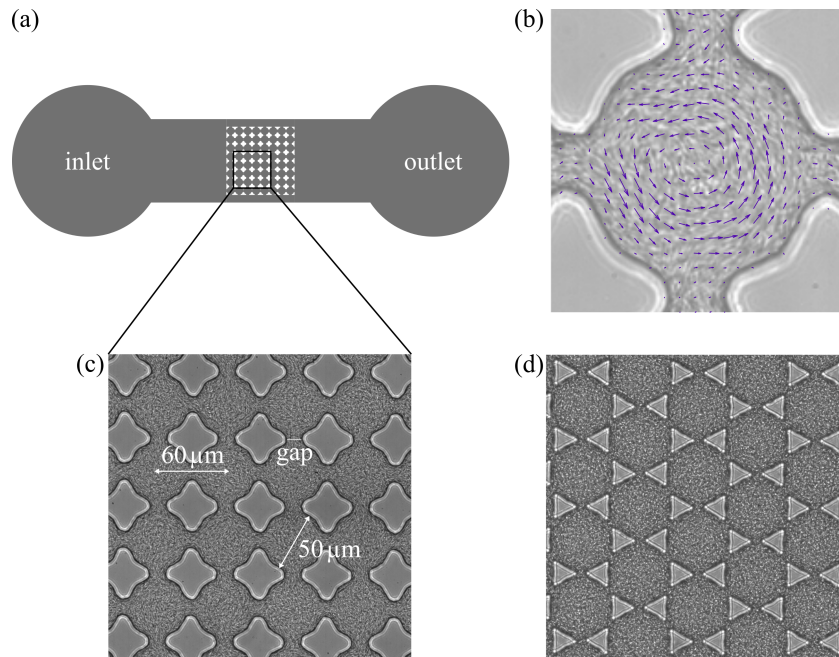


Figure 4.1: Lattice of vortices setup. (a) Sketch of the full microfluidic chamber. Bacteria are injected in the inlet and fill up the central lattice of cavities. For clarity, only a  $8 \times 8$  lattice is shown. (b) Bacterial flow inside a cavity. The suspension forms an unstable vortex. Due to a lower magnification than in experiments in flattened drops, the motion of bacteria at the PDMS interface against the bulk is here difficult to image but is still present. Arrows: flow measured by PIV. The cavity is  $\approx 50 \mu\text{m}$  in diameter. (c) Square lattice. (d) Triangular lattice.

## 4.2.2 Analysis

### Notations

I analysed the lattice behaviour by computing the state of each vortex and around each pillar. The sets of vortices and pillars in a given lattice are denoted by  $V$  and  $P$  respectively. The symbol  $\sim$  denotes adjacent vortices or pillars.  $E_V = \{v, v' \in V | v \sim v'\}$  and  $E_P = \{v \in V, p \in P | v \sim p\}$  are the sets of pairs of vortices and pairs of vortex/pillars that are adjacent. Finally  $\partial_i$  denotes the set of all adjacent sites to the vortex or pillar  $i$ , such that  $\partial_i^V = \{v \in V | i \sim v\}$  and  $\partial_i^P = \{p \in P | i \sim p\}$ .

### Flow Measurement

Bacterial flow  $\mathbf{u}(x, y, t)$  was measured by the same PIV method presented earlier (section 2.2.1), without time averaging. Subwindows were  $16 \times 16$  pixels large (16 pixels =  $6.7 \mu\text{m}$ ), with 50% overlap, yielding about  $15 \times 15$  measurements per cavity.

### Spins Estimates

I assigned a spin  $\sigma_v(t)$  to each cavity  $v \in V$ , defined as the normalised angular momentum

$$\sigma_v(t) = \frac{\sum \mathbf{u}(x, y, t) \times \mathbf{r}(x, y)}{\langle \|\mathbf{u}\| \rangle_{x, y, t} \sum \|\mathbf{r}(x, y)\|}, \quad (4.1)$$

where sums are taken over all subwindows of coordinates  $\{x, y\}$  inside the cavity  $v$ ,  $\mathbf{u}$  is the bacterial flow measured by PIV,  $\mathbf{r}$  is the radial vector from the cavity centre to  $\{x, y\}$ , and  $\langle \|\mathbf{u}\| \rangle_{x, y, t}$  is the averaged bacterial velocity taken over all cavities of a movie.

If the suspension forms vortices of consistent speed in each cavity,  $\sigma_v$  goes to  $\pm 1$  depending on the vortex direction, CW ( $\sigma_v > 0$ ) or CCW ( $\sigma_v < 0$ ). If the bacteria do not form vortices,  $\sigma_v \approx 0$ . To quantify how well vortices form, I also computed the average absolute spin for each movie:  $S = \langle |\sigma_v| \rangle_{v, t}$ .

For square lattices, I also computed a similar spin around each pillar  $p \in P$ ,

$$\sigma_p(t) = \frac{\sum \mathbf{u}(x, y, t) \cdot \mathbf{t}(x, y)}{\langle \|\mathbf{u}\| \rangle \sum 1}, \quad (4.2)$$

where  $\mathbf{t}$  is the unit vector, tangential to the interface, and the sum runs over PIV subwindows closer than  $5 \mu\text{m}$  from the PDMS surface.

## Spin-Spin Correlation

To quantify the interactions between adjacent vortices, the spin-spin correlation  $C$  was measured over each movie, defined as

$$C = \frac{\sum_{\{v,v'\} \in E_V} \sigma_v \sigma_{v'}}{\sum_{\{v,v'\} \in E_V} 1/2(\sigma_v^2 + \sigma_{v'}^2)}. \quad (4.3)$$

Thus  $C = 1$  if all vortices experience the same direction (*ferromagnetism*) and  $C = -1$  if the circulation direction alternates between adjacent cavities (*antiferromagnetism*).

## 4.2.3 Results

### Lines of Vortices

I first injected the dense suspension into chains of cavities. The suspension forms reasonably stable vortices, with  $S = \langle |\sigma_v| \rangle_{v,t} > 0.6$  (figure 4.2c), in agreement with measurements in flattened drops (for a similar diameter in a flattened drop, the vortex order parameter yields  $\Phi \approx 0.8$ ).

Each vortex interacts through a gap, yielding different lattice states depending on the gap size. For the smallest gaps, 5 to 10  $\mu\text{m}$ , interactions are too weak and no correlation was measured between vortices. For larger gaps, 10 to 40  $\mu\text{m}$ , bacteria on each side of the gap locally move in the same direction, yielding adjacent vortices of opposite spins (figure 4.2a). The correlation then oscillates around  $C \approx -0.6$ , such that the bacterial suspension forms an antiferromagnetic state (figure 4.2b). For even larger gaps, the cavity walls become almost straight and form a channel. In such cases, the suspension moves in a persistent stream, like in racetracks (not shown).

### Triangular Lattices

Bacteria are then injected into triangular lattices, in which each cavity is connected to its six neighbours (figure 4.1c) [149]. Due to the cavities distribution, the suspension cannot form a perfect antiferromagnetic state in which each vortex circulates in opposite direction to its six neighbours. A state of lowest energy can still be calculated for an antiferromagnetic triangular Ising net [149]. One solution is to have a frustrated

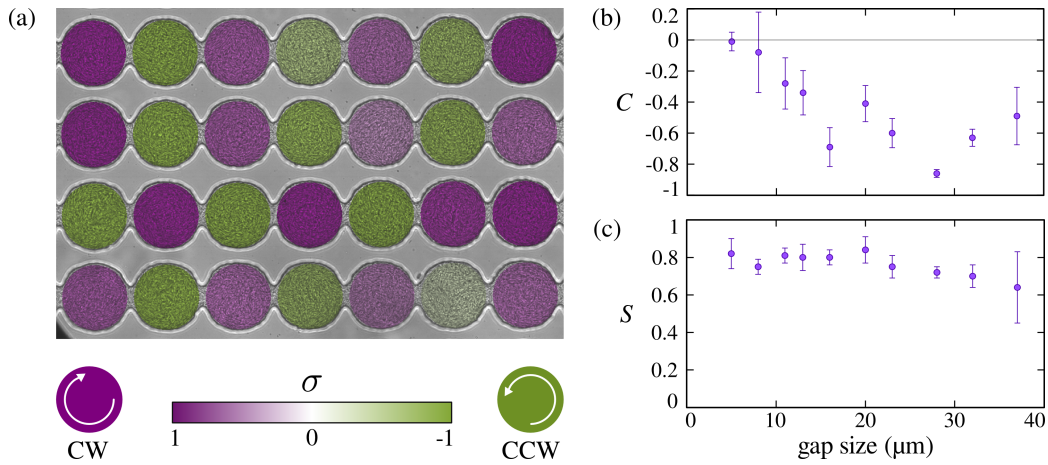


Figure 4.2: Self-organisation in chains of vortices. (a) Example of four lines. Vortices are colour-coded according to the spin direction, purple for CW and green for CCW. Cavity diameter:  $50\mu\text{m}$ . Gap:  $16\mu\text{m}$ . (b) Spin-spin correlation  $C$  depending on the gap size. (c) Mean absolute spin  $S$ . Each point is averaged over at least four moves. Bars: standard error.

arrangement with two thirds of the pairs of vortices in opposite direction (figure 4.3). The resulting spin-spin correlation is then  $C_{\text{th}} = -1/3$ .

However, experiments with bacteria show that a ferromagnetic state in which all vortices share the same direction is hugely favourable (figure 4.4a,b). For gaps between 9 to  $17\mu\text{m}$ ,  $C > 0.6$  (figure 4.4c). When considered over all movies, the vortices did not have a preferred direction: the mean spin over 88 movies what  $\langle \sigma_v \rangle = 0.053$ , less than the estimated standard deviation for a normal distribution around 0.076 (given  $S = 0.71$ ). Thus, spin-spin interactions only are responsible for the ferromagnetic state,

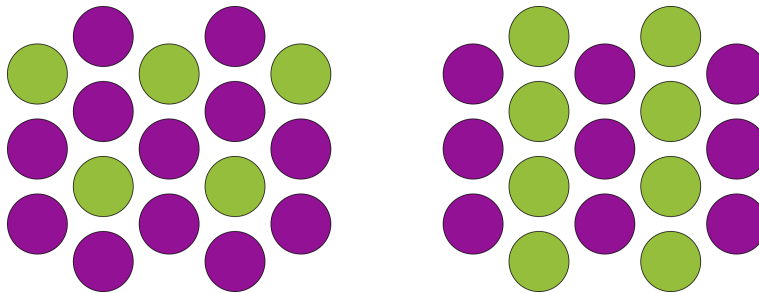


Figure 4.3: Two examples of antiferromagnetic triangular lattices of lowest energy. The spin-spin correlation  $C_{\text{th}} = -1/3$ .

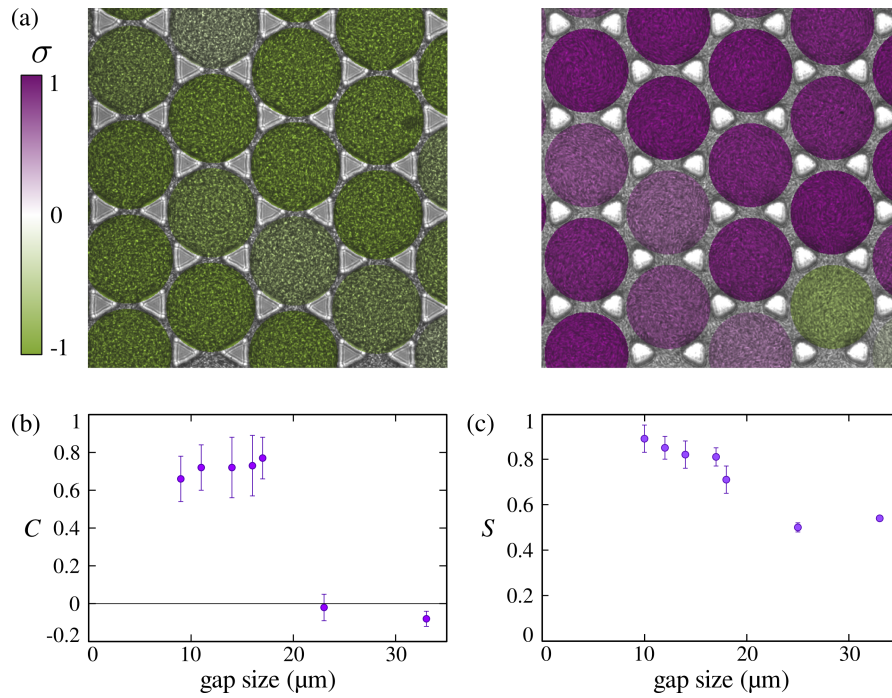


Figure 4.4: Self-organisation in triangular lattices. (a) Examples of two chambers. Vortices are colour-coded according to the spin direction, purple for CW and green for CCW. Cavity diameter:  $55\mu\text{m}$ . Gap:  $16$  and  $20\mu\text{m}$ . (b) Spin-spin correlation  $C$  depending on the gap size. (c) Mean absolute spin  $S$ . Each point is averaged over at least four movies. Bars: standard error.

and not an intrinsic spin associated with the cavities. I also observed that bacteria at the PDMS interfaces would swim around pillars. Such a circulation is likely to promote the ferromagnetic state.

The lattice then transitions for gaps  $\approx 20\mu\text{m}$  to a random state: the absolute spin decreases from  $S \approx 0.7$  to  $S \approx 0.5$ , indicating a modest disorganisation of the vortices, and the correlation becomes negligible,  $C \approx 0$  at gaps  $23$  and  $33\mu\text{m}$ . At such gap sizes, pillars become relatively small, their confinement effect being too weak to stabilise vortices, thus the suspension enters a turbulent state.

### Square Lattices

Square lattices are of particular interest as they exhibit both ferromagnetic and anti-ferromagnetic states, even though they do not present a frustrated topology. I study

the spin-spin correlation and the mean absolute spin depending on the gap width and identify four states (figure 4.5):

**Random state** For the smallest gaps, less than  $2\mu\text{m}$ , the suspension self-organises into stable vortices,  $S > 0.7$ , with independent orientations,  $C \approx 0$ . This state is difficult to obtain experimentally as bacteria get blocked in the gaps during the injection process, resulting in either half-concentrated or jammed cavities. Yet this state is simple to understand theoretically: small gaps prevent interactions between vortices, resulting in spins of random sign. It is equivalent to flattened drops experiments in which vortices are disconnected.

**Antiferromagnetic state** For small intermediate gaps, between  $4$  and  $7.5\mu\text{m}$ , spins are still high,  $S > 0.6$ , but their correlation becomes negative,  $C \approx -0.2$ . The bacterial suspension self-organises into vortices of alternating direction, as also found in chains of cavities.

**Ferromagnetic state** For large intermediate gaps, between  $7.5$  and  $18\mu\text{m}$ , the spins decrease in magnitude,  $S \approx 0.5$ , but most importantly the correlation changes sign,  $C \approx +0.1$ . The suspension is ordered into domains where vortices share the same direction, as in triangular lattices.

**Turbulent state** For the largest gaps, more than  $20\mu\text{m}$ , the confinement is not strong enough to stabilise vortices,  $S \approx 0.2$ , and the suspension recovers its turbulent state, as observed in unconfined chambers. The correlation between cavities is also lost,  $C \approx 0$ .

#### 4.2.4 Discussion

Experiments show that the bacterial circulation can be simply controlled by changing the topology of the lattice and the opening between cavities. Yet a serious paradox appears: how can the small geometrical differences modify the bacterial interaction to yield opposite behaviours? Two criteria appear central: the gap size and the topology of the lattice (i.e. the number of adjacent vortices). Here, I present some clues to understand bacterial self-organisation, focusing in particular on the interaction between bacteria in the bulk or at the PDMS interface.

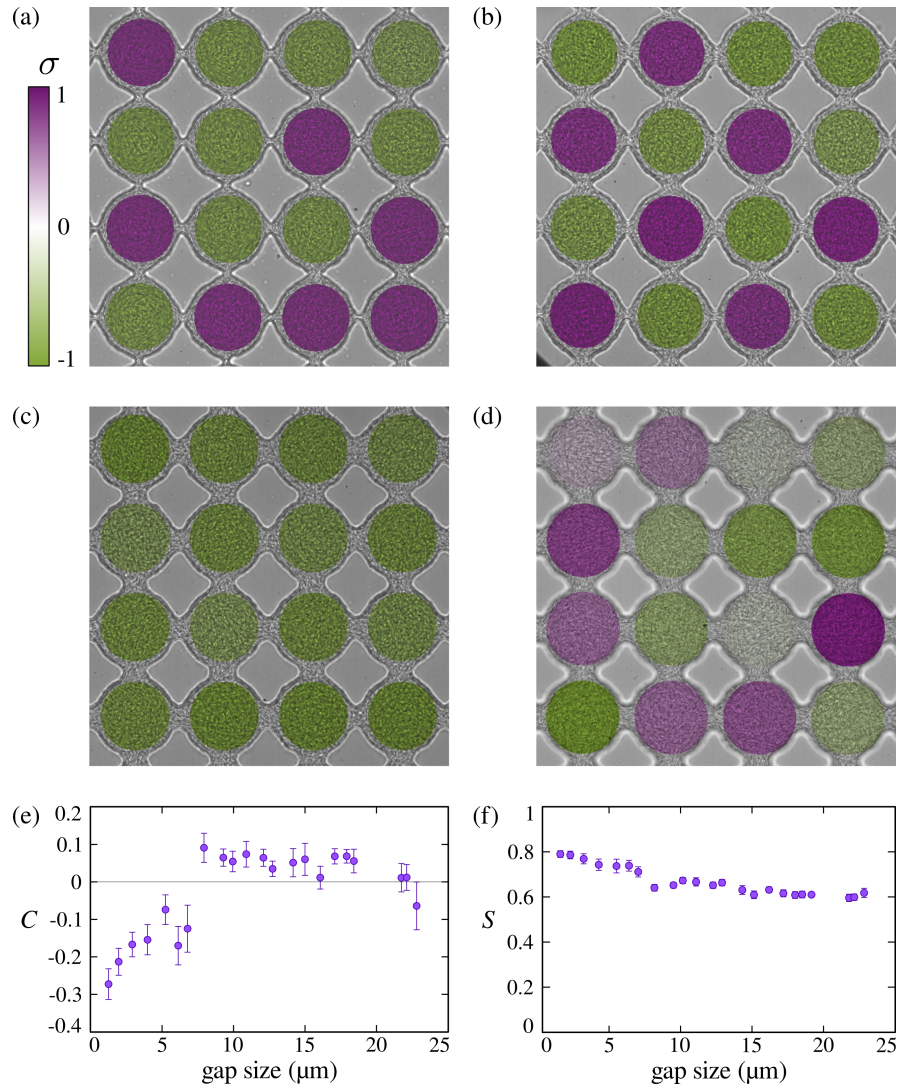


Figure 4.5: Self-organisation in square lattices. (a-d) Four lattice states, for increasing gap sizes. Vortices are colour-coded, purple for CW and green for CCW. (a) Random state. (b) Antiferromagnetic state. (c) Ferromagnetic state. (d) Turbulent state. Brighter vortices indicate smaller spin magnitude. (e) Spin-spin correlation  $C$  and (f) average absolute spin  $S$  depending on the gap size. Each point is averaged over at least seven movies. Bars: standard error.

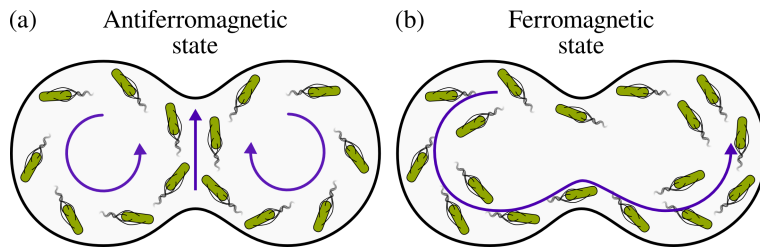


Figure 4.6: Model for the vortex interaction. (a) Bacteria in the bulk move in the same direction on either side of the gap, resulting in opposite spins. (b) Bacteria swim along the PDMS surface, leading to spins of same sign.

### Bulk and Interface Bacteria

The antiferromagnetic state seems to be driven by bacteria in the bulk of each cavity, interacting through long-range fluid flows across the gap, forcing bacteria close to the gap to move in the same direction, resulting in opposite spins (figure 4.6a). One would expect this mechanism to become stronger for wider gaps. Instead, the antiferromagnetic state in square lattices is only dominant in small gap chambers.

*Au contraire* the ferromagnetic state is probably driven by bacteria circulating around pillars (figure 4.6b). This interaction also weakens for small gaps, as bacteria from neighbouring pillars have to cross the gap in opposite directions, thus resulting in a strong shear along the gap width.

The resulting lattice ordering can be understood as the competition between bacteria in the bulk and at interfaces. The former dominate at small gaps and the latter at larger ones, as shown in the transition from an antiferromagnetic to a ferromagnetic state in square lattices.

Likewise these interactions could also be favoured depending on the lattice topology: for example small pillars in triangular lattices may promote the circulation of bacteria at the PDMS interface. Furthermore, the more neighbours, the more pillars around which bacteria can swim, possibly explaining why antiferromagnetic state was only observed in lines of cavities and ferromagnetic state, in triangular lattices.

### Chamber Geometry

I show that the vortex state can be controlled in square lattices by varying the gap size. Obviously other parameters can affect the bacterial circulation. I tried numerous

shapes during preliminary experiments and here report some of their effects:

**Gap thickness** This is the distance between cavity edges i.e. the difference of distance between centres and their diameter. Experiments presented here have a gap thickness around  $10\mu\text{m}$ . I also tried chambers with a gap thickness  $\sim 5\mu\text{m}$  and only observed the ferromagnetic state. This effect can be understood from the bacteria swimming around the pillars: when the gap thickness increases, so does the total shear in the gap region, weakening the ferromagnetic interaction.

**Chamber height** I tried different microchamber heights, from  $15$  to  $30\mu\text{m}$ . Higher chambers form more stable vortices (larger  $S$  but also more persistent, see subsection on ‘Time’) and lattices with larger spin-spin correlation  $|C|$ . However higher chambers also come with a strong downside: they are likely to have a preferred vortex direction (CCW in movies). This is likely due to the asymmetry of the chamber: glass at the bottom surface and PDMS at the top. The dense suspension quickly consumes the oxygen diluted in the medium and PDMS acts as a reservoir, creating a gradient of oxygen in the chamber. Thus bacteria swim faster at the top. Moreover, single bacteria exhibit circular trajectories when swimming close to surfaces (CW). The combined effect can then result in a preferred vortex direction, which itself produces artificial ferromagnetic states. In all experiments presented here, I made sure that vortices had the same probability to spin CW or CCW.

**Cavity diameter** I set the diameter to  $50\mu\text{m}$  in experiments, in order to have stable enough vortices (the critical diameter is  $w^* = 70\mu\text{m}$ , as found in flattened drops). Changing the diameter could potentially affect the stability of the vortices as well as the interaction strength.

**Suspension density** I have only performed experiments with very dense suspensions. This is actually a limitation of my experimental protocol, as I do not control the density perfectly. The suspension density could vary by a factor of two, potentially resulting in either semi-diluted chambers (showing inhomogeneous density) or jammed cavities. I would not record any movie in such cases. When, occasionally, some cavities were not fully filled, cells do not accumulate at the

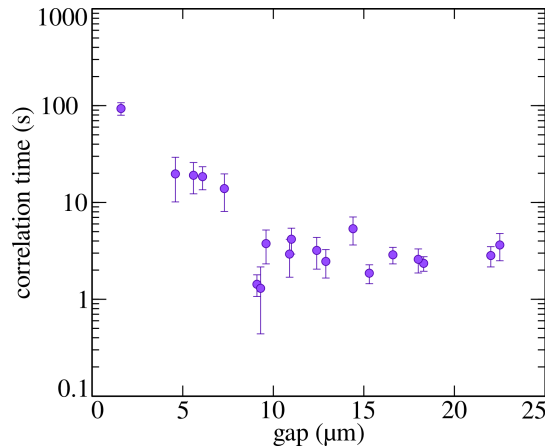


Figure 4.7: Correlation time of the vortex spins depending on the gap size. The correlation time is computed over each movie and then averaged over at least four movies. Bars: standard error.

periphery as in flattened drops, but rather form a homogeneous suspensions with little ordering.

## Time

In the entire analysis, I have neglected the effect of time. I assume that the system reaches its steady state in less than four minutes, and then average the measurements over the 10 seconds of a movie. I measured the spin correlation over time for each movie,

$$C_t(dt) = \frac{\sum_{v \in V} (\sigma(v, t) \cdot \sigma(v, t + dt))}{\sum_{v \in V} (\frac{1}{2}(\sigma(v, t)^2 + \sigma(v, t + dt)^2)}. \quad (4.4)$$

I then fitted  $C_t$  with a decaying exponential to obtain the typical correlation time. Figure 4.7 shows the variation of the correlation time with the gap size in square lattices. The persistence time  $C_t$  decreases with the gap size, from more than a minute with gaps  $\approx 2 \mu\text{m}$  to a couple of seconds in the largest chambers.

I took ten second long movies, four and eight minutes after injection. The correlation time shows that the suspension has most probably reached its steady state at this stage. Moreover, for the smallest gaps  $g < 8 \mu\text{m}$ , the time correlation indicates that spins do not vary significantly over a single movie.

## Large and Small Correlations

Surprisingly, the correlation in lines and triangular lattices is quite strong compared with that in square lattices. I have managed to get larger  $|C|$  in square lattices but the results would not be reproducible (note that I have not selected any of the movies in the data set, they are all movies I have taken, with this particular chamber shape and height).

However, the small  $C$  in square lattices can be understood from the competition between the antiferromagnetic and the ferromagnetic interactions. While one of them strongly dominates in linear and triangular lattices, they are almost balanced in square lattices, resulting in the smaller  $|C|$ .

## 4.3 Modelling the Square Lattice as an Ising System

### 4.3.1 Model

#### Union-Jack lattice

To describe and gain insight into the self-organisation in lattices, I collaborated with Francis Woodhouse and Jörn Dunkel, former PhD student and post-doc in the group, respectively. We propose an Ising model in which each vortex is solely represented by its spin. We only consider the case of square lattices as we have significantly more experimental data and since this arrangement offers study of more varied behaviours.

We start by assuming that fundamental spin-spin interactions are negative: adjacent vortices force each other to circulate in opposite directions. This idea contradicts with the observed ferromagnetic state. This state is most probably due to bacteria swimming around pillars, and thus, to overcome this contradiction, we also model the circulation around pillar with a similar continuous spin.

We then obtain a decorated lattice, called *centred-square* or *Union-Jack* lattice [150, 151, 152]: each vortex interacts with its four adjacent pillars as well as four adjacent vortices (figure 4.8). Moreover, we start by assuming that each spin lies in a double well potential. As a basic principle, we expect that if vortex-vortex interactions dominate, the lattice will form an antiferromagnetic state, while, if vortex-pillar interactions dominate, the ferromagnetic state will be favoured.

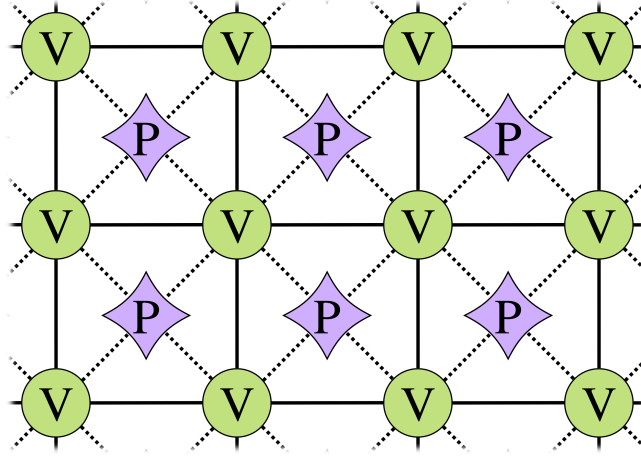


Figure 4.8: Decorated lattice used to model square lattices. Pillars (P) are placed at the centre of each four adjacent vortices (V). Vortex-vortex (solid lines) and vortex-pillar interactions (dotted lines) are included while pillar-pillar interactions are neglected.

I first present a mathematical description and the system Hamiltonian of this Ising model, before applying it to the study of experimental results.

Francis Woodhouse, Jörn Dunkel and I equally contributed to this section. Francis Woodhouse and Jörn Dunkel came up with the idea of an Ising model in a decorated lattice, we developed the model together, I performed most of the direct parameter fitting and Francis Woodhouse is currently working on the complete Hamiltonian fitting and simulations.

### Lattice Hamiltonian

We consider the statistics of vortex and pillar spins as measured experimentally. We call  $\sigma = \{\sigma_v, v \in V\} \cup \{\sigma_p, p \in P\}$ , the set of spins at a given time (equations 4.1 and 4.2). We describe the lattice by its Hamiltonian  $\mathcal{H}$  which is related to the probability  $p$  to find spins in the configuration  $\sigma$  by

$$p(\sigma) = \frac{1}{Z} \exp(-\mathcal{H}(\sigma)), \quad (4.5)$$

where  $Z = \int_{\sigma} \mathcal{H}(\sigma) d\sigma$  is the partition function. The Hamiltonian depends on vortex-vortex and vortex-pillar interactions together with single vortex and single pillar po-

tentials

$$\mathcal{H}(\sigma) = -J_V \sum_{\{v,v'\} \in E_V} \sigma_v \sigma_{v'} - J_P \sum_{\{v,p\} \in E_P} \sigma_v \sigma_p + \sum_{v \in V} \mathcal{V}_V(\sigma_v) + \sum_{p \in P} \mathcal{V}_P(\sigma_p), \quad (4.6)$$

where  $J_V$  and  $J_P$  denote the vortex-vortex and vortex-lattice interaction strengths respectively and  $\mathcal{V}_V$  and  $\mathcal{V}_P$  are the single vortex and single pillar potentials. We choose to use a double-well potential,

$$\mathcal{V}_V(\sigma) = \frac{a_V}{2} \sigma^2 + \frac{b_V}{4} \sigma^4, \quad (4.7)$$

$$\mathcal{V}_P(\sigma) = \frac{a_P}{2} \sigma^2 + \frac{b_P}{4} \sigma^4, \quad (4.8)$$

where  $a_V$ ,  $b_V$ ,  $a_P$  and  $b_P$  are constants which should depend on the lattice geometry and the suspension behaviour.

Our goal is to estimate the Hamiltonian parameters from experimental statistics, looking in particular at the role of gap size.

### 4.3.2 Direct Analysis of the Experiments

Here, I present a method to estimate, directly from the experimental measurement statistics, some effective parameters of the lattice Hamiltonian. The idea is to measure the probability to find a vortex  $v$  at a given spin  $\sigma_v$ , depending on the average spin of its adjacent vortices. We first simplify the expression of the Hamiltonian by renormalisation of the lattice, and define an effective potential associated with single vortices, from which we can estimate some parameters.

#### Pillar spin behaviour

Pillar spins  $\{\sigma_p, p \in P\}$  contribute to the lattice Hamiltonian in their single pillar potential,

$$\sum_{p \in P} \mathcal{V}_P(\sigma_p), \quad (4.9)$$

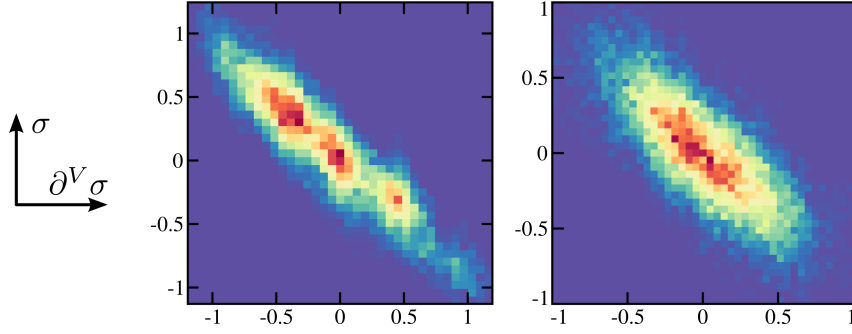


Figure 4.9: Distribution of pillar spins in two movies (a-b). Colour-coded 2D histogram of the pillar spins  $\sigma$  and averaged neighbour vortex spins  $\partial^V \sigma$  (equation 4.11). Red: highest density, Purple: lowest density. In both cases, spins are clustered around  $\sigma = -\partial^V \sigma$ .

and vortex-pillar interactions,

$$-J_P \sum_{\{v,p\} \in E_P} \sigma_v \sigma_p . \quad (4.10)$$

The spin of a given pillar then only depends on that of the four adjacent vortices. We thus study the distribution of pillar spins depending on the averaged neighbour vortex spin

$$\partial^V \sigma_p = \frac{1}{4} \sum_{\{v,p\} \in E_P} \sigma_v . \quad (4.11)$$

Figure 4.9 shows two examples of 2D histograms obtained from two different movies. While spins appear more clustered in (a) than in (b), they both show the density to be largest around  $\sigma = -\partial^V \sigma$ : each pillar spin is the opposite of the average spin of its four adjacent vortices.

### Renormalised lattice

The system Hamiltonian  $\mathcal{H}$  is too complex to directly fit from the distribution of vortex and pillar spins. We thus use the clustering of pillar spins around  $-\partial^V \sigma$  to renormalise  $\mathcal{H}$  and obtain a form that can be decomposed into effective single vortex potentials.

We first replace all instances of  $\{\sigma_p, p \in P\}$ , by  $-\partial^V \sigma_p$ . We then assume that since the value of the pillar spins is fixed, their potential  $\mathcal{V}_P(\sigma_k)$  is constant. We obtained

the simplified version of the Hamiltonian of the system

$$\begin{aligned}
\mathcal{H}(\sigma) &= -J_V \sum_{\{v,v'\} \in E_V} \sigma_v \sigma_{v'} + \frac{J_P}{4} \sum_{\{v,p\} \in E_P} \sigma_v \sum_{\{v',p\} \in E_P} \sigma_{v'} + \sum_{v \in V} \mathcal{V}_V(\sigma_v) \\
&= -\left(J_V - \frac{1}{2}J_P\right) \sum_{\{v,v'\} \in E_V} \sigma_v \sigma_{v'} + \frac{1}{4}J_P \sum_{\{v,v''\} \in E_V^2} \sigma_v \sigma_{v''} \\
&\quad + \sum_{v \in V} \left[ \left(\frac{1}{2}a_V + J_P\right) \sigma_v^2 + \frac{1}{4}b_V \sigma_v^4 \right] \\
&= -J_V^{\text{eff}} \sum_{\{v,v'\} \in E_V} \sigma_v \sigma_{v'} + \frac{1}{4}J_P \sum_{\{v,v''\} \in E_V^2} \sigma_v \sigma_{v''} + \sum_{v \in V} \left[ \frac{1}{2}a_V^{\text{eff}} \sigma_v^2 + \frac{1}{4}b_V \sigma_v^4 \right],
\end{aligned} \tag{4.12}$$

where  $E_V^2$  is the set of diagonally adjacent vortices. We further neglect interactions between diagonal pairs of vortices, as this effect is of lesser strength and bacteria are unlikely to keep their orientation from one side of a pillar to the other (going through two gaps). We end up with a classical expression for a square lattice, except that  $J_V^{\text{eff}} = J_V - \frac{1}{2}J_P$  reflects the effective interactions between vortices, through bulk and boundary bacteria. Since  $J_V, J_P < 0$ , the sign of  $J_V^{\text{eff}}$  indicates which interaction dominates.

We can now express the lattice Hamiltonian as the sum of effective vortex potentials

$$\mathcal{H}(\sigma) = \sum_{v \in V} \mathcal{V}^{\text{eff}}(\sigma_v, \partial^V \sigma_v), \tag{4.13}$$

where

$$\mathcal{V}^{\text{eff}}(\sigma_v, \partial^V \sigma_v) = -2J_V^{\text{eff}} \sigma_v \partial^V \sigma_v + \left( \frac{1}{2}a_V^{\text{eff}} \sigma_v^2 + \frac{1}{4}b_V \sigma_v^4 \right). \tag{4.14}$$

### Estimation of the effective single vortex potential

This simplified version of  $\mathcal{H}$  allows us to compute effective parameters from the spin distribution  $\sigma$ .

First of all, we need to experimentally estimate  $\mathcal{V}^{\text{eff}}$ . We assume that the spin distribution follows a Boltzmann distribution,

$$p(\sigma_v | \partial^V \sigma_v) = \frac{1}{Z_v(\partial^V \sigma_v)} \exp\left(-\mathcal{V}^{\text{eff}}(\sigma_v, \partial^V \sigma_v)\right), \tag{4.15}$$

where  $p(\sigma_v|\partial^V\sigma_v) = \frac{\#(\sigma_v,\partial^V\sigma_v)}{\#(\partial^V\sigma_v)}$ , and  $Z_v = \int_{\sigma_{v'}} \mathcal{V}(\sigma_{v'},\partial^V\sigma_v)d\sigma_{v'}$ .

Equivalently,

$$\mathcal{V}^{\text{eff}}(\sigma_v,\partial^V\sigma_v) = -\ln(p(\sigma_v|\partial^V\sigma_v)) - \ln(Z_v(\partial^V\sigma_v)). \quad (4.16)$$

So far, we can measure  $p$ , except for spins with low probability which we will not take into account in the parameter fitting and  $Z_v$  is unknown but only depends on adjacent spins  $\partial^V\sigma_v$ . In particular,  $\mathcal{V}^{\text{eff}}(0,\partial^V\sigma_v) = 0$  (equation 4.14) and we can then get  $\ln(Z_v(\partial^V\sigma_v)) = -\ln(p(0|\partial^V\sigma_v))$ . We will actually use a slightly different approach to estimate  $Z_v$ , as described below. Moreover,  $\mathcal{V}^{\text{eff}}$  is symmetric in  $\sigma_v$  and antisymmetric in  $\partial^V\sigma_v$ , we use these properties to estimate  $J_V^{\text{eff}}$ ,  $a_V^{\text{eff}}$  and  $b_V$ .

### Vortex-vortex interaction

We first study the antisymmetric part of the effective potential. On the experimental side,  $\mathcal{V}_{\text{anti}}^{\text{eff}}$  can be directly estimated from the probability distribution

$$\mathcal{V}_{\text{anti}}^{\text{eff}} = \frac{1}{2} [\mathcal{V}^{\text{eff}}(\sigma_v,\partial^V\sigma_v) - \mathcal{V}^{\text{eff}}(-\sigma_v,\partial^V\sigma_v)] \quad (4.17)$$

$$= \frac{1}{2} [-\ln(p(\sigma_v|\partial^V\sigma_v)) + \ln(p(-\sigma_v|\partial^V\sigma_v))]. \quad (4.18)$$

On the theoretical side,  $\mathcal{V}_{\text{anti}}^{\text{eff}}$  only depends on the effective vortex vortex interaction

$$\mathcal{V}_{\text{anti}}^{\text{eff}}(v) = -2J_V^{\text{eff}}\sigma_v\partial^V\sigma_v. \quad (4.19)$$

Figure 4.10 shows the estimate of  $\mathcal{V}_{\text{anti}}^{\text{eff}}$ , depending on the vortex spin (x-axis) and its neighbours spins (colour-coded). For a given mean adjacent spin  $\partial^V\sigma_v$  (colour-coded in the figure), data point are roughly aligned, with slope  $-2J_V^{\text{eff}}\partial^V\sigma_v$ .

This construction allows us to subtract the partition function  $Z_v$  and we can directly estimate the effective interaction (figure 4.10)

$$J_V^{\text{eff}} = \frac{\ln(p(\sigma_v|\partial^V\sigma_v)) - \ln(p(-\sigma_v|\partial^V\sigma_v))}{2\sigma_v\partial^V\sigma_v}. \quad (4.20)$$

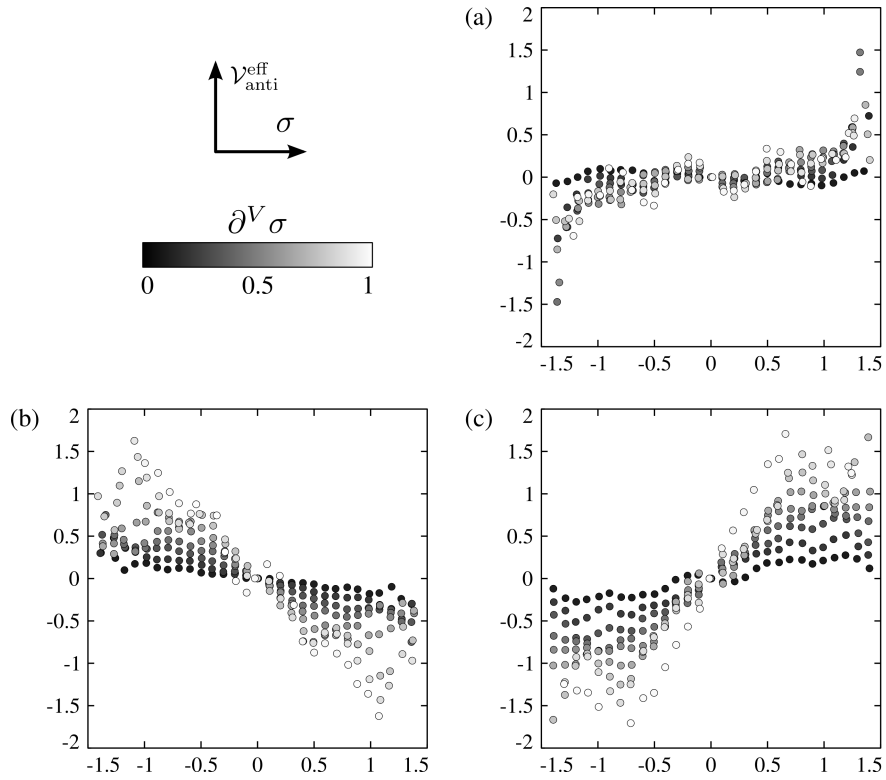


Figure 4.10: The antisymmetric part of the effective Hamiltonian, reveals the vortex-vortex interaction. (a-c)  $\mathcal{V}_{\text{anti}}^{\text{eff}}$  as a function of the vortex spin  $\sigma$ . Colour coding reflects the average neighbour spin  $\partial^V \sigma$ , the brighter the larger. Each plot shows a different interaction mode: (a) weak interaction, (b) ferromagnetic and (c) antiferromagnetic.

## Single Vortex Potential

The symmetric part of the effective potential allows us to neglect the interactions between neighbours, where

$$\mathcal{V}_{\text{sym}}^{\text{eff}} = \frac{1}{2} \left[ \mathcal{V}^{\text{eff}}(\sigma_v, \partial^V \sigma_v) + \mathcal{V}^{\text{eff}}(-\sigma_v, \partial^V \sigma_v) \right] \quad (4.21)$$

$$= \frac{1}{2} \left[ -\ln(p(\sigma_v | \partial^V \sigma_v)) - \ln(p(-\sigma_v | \partial^V \sigma_v)) \right] - \ln(Z_v(\partial^V \sigma_v)) \quad (4.22)$$

$$= \frac{1}{2} a_V^{\text{eff}} \sigma_v^2 + \frac{1}{4} b_V \sigma_v^4. \quad (4.23)$$

As explained above, one can estimate  $Z_v(\partial^V \sigma_v) = p(0 | \partial^V \sigma_v)$ . Unfortunately, there are often few data points around  $\sigma_v = 0$ , and for this reason,  $p(0 | \partial^V \sigma_v)$  can be difficult to estimate. Yet,  $Z_v$  is the only term that depends on  $\partial^V \sigma_i$  and we therefore adjust the estimated value of  $\mathcal{V}_{\text{sym}}^{\text{eff}}$  such that  $Z_v(\partial^V \sigma_v) = c$ , where  $c$  is a constant. We then fit  $a_V^{\text{eff}}$ ,  $b_V$  and  $c$ , such that (figure 4.11)

$$\mathcal{V}_{\text{sym}}^{\text{eff}} = \frac{1}{2} a_V^{\text{eff}} \sigma_v^2 + \frac{1}{4} b_V \sigma_v^4 + c \quad (4.24)$$

$$= \frac{1}{2} \left[ -\ln(p(\sigma_v | \partial^V \sigma_v)) - \ln(p(-\sigma_v | \partial^V \sigma_v)) \right]. \quad (4.25)$$

## Additional information

We aim to measure  $a_V^{\text{eff}}$ ,  $b_V$  and  $J_V^{\text{eff}}$  for each individual gap width. To improve the accuracy, we add up all statistics for chambers of similar gap size (each data point corresponds to at least six movies).

Moreover we take advantage of the symmetry of the system Hamiltonian  $\mathcal{H}$  by the transformation:  $\{\sigma, \partial^V \sigma\} \rightarrow \{-\sigma, -\partial^V \sigma\}$ . To obtain more data points and accurate estimates, we transform all data set such that  $\partial^V \sigma \geq 0$ .

Finally, all fittings have been done using the function *fit* in Matlab.

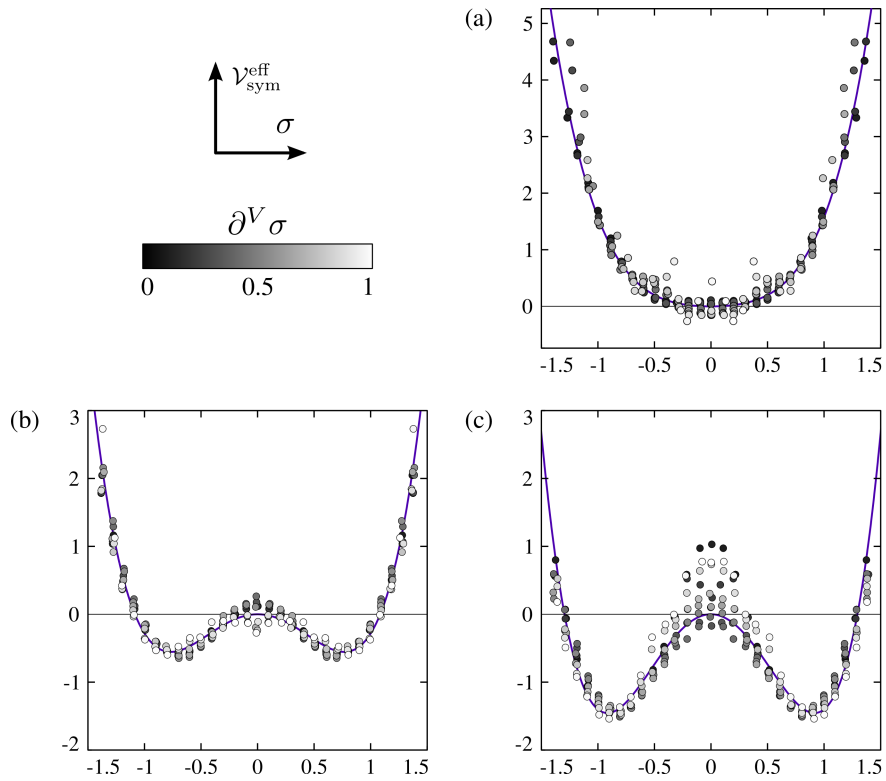


Figure 4.11: The symmetric part of the effective Hamiltonian reveals the single vortex potential. (a-c)  $\mathcal{V}_{\text{sym}}^{\text{eff}}$  depending on the vortex spin  $\sigma$ . Colour coding reflects the average neighbour spin  $\partial^V \sigma$ , the brighter the larger. between panels (a) to (c), the  $\mathcal{V}_{\text{sym}}^{\text{eff}}$  transitions from a potential with a single minimum at  $\sigma = 0$  to a double-well profile, with  $\sigma_{\text{min}} \rightarrow \pm 1$ . Lines: fitted potential.

### 4.3.3 Results

#### Four states

We first plotted the 2D distribution of spin  $\sigma$  to mean adjacent spin  $\partial^V \sigma$  for different movies (figure 4.12). We found again the four behaviours corresponding to the square lattice states identified previously. Figure 4.13 shows, for each state, an example of the estimated effective single vortex potential  $\mathcal{V}^{\text{eff}}$  (points) and fitting (surface) following the method described above.

**Random** The histogram shows two horizontal bands, revealing that spins are clustered around  $\sigma = \pm 1$  but are independent of their neighbour spins  $\partial^V \sigma$ . Fitting of the energy shows that spins sit in a deep double-well potential, stabilising the suspension into a strong vortex. Moreover the interaction strength  $J_V^{\text{eff}}$  is negligible.

**Antiferromagnetic** The two bands are still present but broader, meaning vortex states are less organised. Moreover, the distribution appears asymmetric:  $\sigma$  is more likely to be of opposite sign of  $\partial^V \sigma$ . This reflects on the energy plot in a smaller energy barrier in the double well. The interaction  $J_V^{\text{eff}}$  becomes negative, revealing that vortex-vortex interaction dominates:  $|J_V| > \frac{1}{2}|J_P|$ .

**Ferromagnetic** Spin magnitude still decreases and this time is positively correlated with  $\partial^V \sigma$ . The energy profile shows an almost flat single vortex potential  $\mathcal{V}_s^{\text{eff}}$ , in combination with a positive interaction  $J_V^{\text{eff}}$ , causing the spins to share the same direction.

**Turbulent**  $\sigma$  and  $\partial^V \sigma$  are clustered around 0 without much correlation. This results in a single well potential with weak or no interactions.

#### Dependence on the gap size

We then quantified the variation of the effective parameters depending on the gap size. To study the effective single vortex potential

$$\mathcal{V}_{\text{sym}}^{\text{eff}} = \frac{a_V^{\text{eff}}}{2} \sigma^2 + \frac{b_V}{4} \sigma^4, \quad (4.26)$$

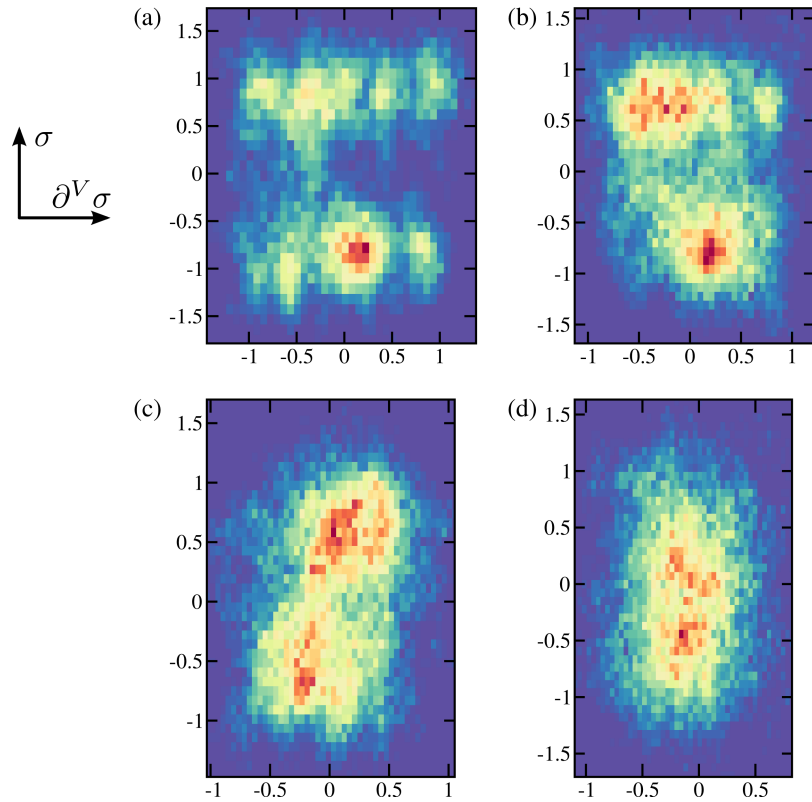


Figure 4.12: Distribution of vortex spins in four movies (a-d). Colour-coded 2D histogram of the vortex spins  $\sigma$  and mean vortices neighbour spins  $\partial^V \sigma$ . Red: highest density, Purple: lowest density. Each histogram indicates a different lattice state. (a) Random:  $\sigma$  is clustered around  $\pm 1$  and is independent of  $\partial^V \sigma$ . (b) Antiferromagnetic:  $\sigma$  is clustered around  $+0.8$  when  $\partial^V \sigma < 0$  and  $-0.8$  when  $\partial^V \sigma > 0$ . (c) Ferromagnetic:  $\sigma$  is clustered around  $+0.6$  when  $\partial^V \sigma > 0$  and  $-0.6$  when  $\partial^V \sigma < 0$ . (d) Disordered: broad distribution of  $\sigma$  and  $\partial^V \sigma$  around 0 without correlation.

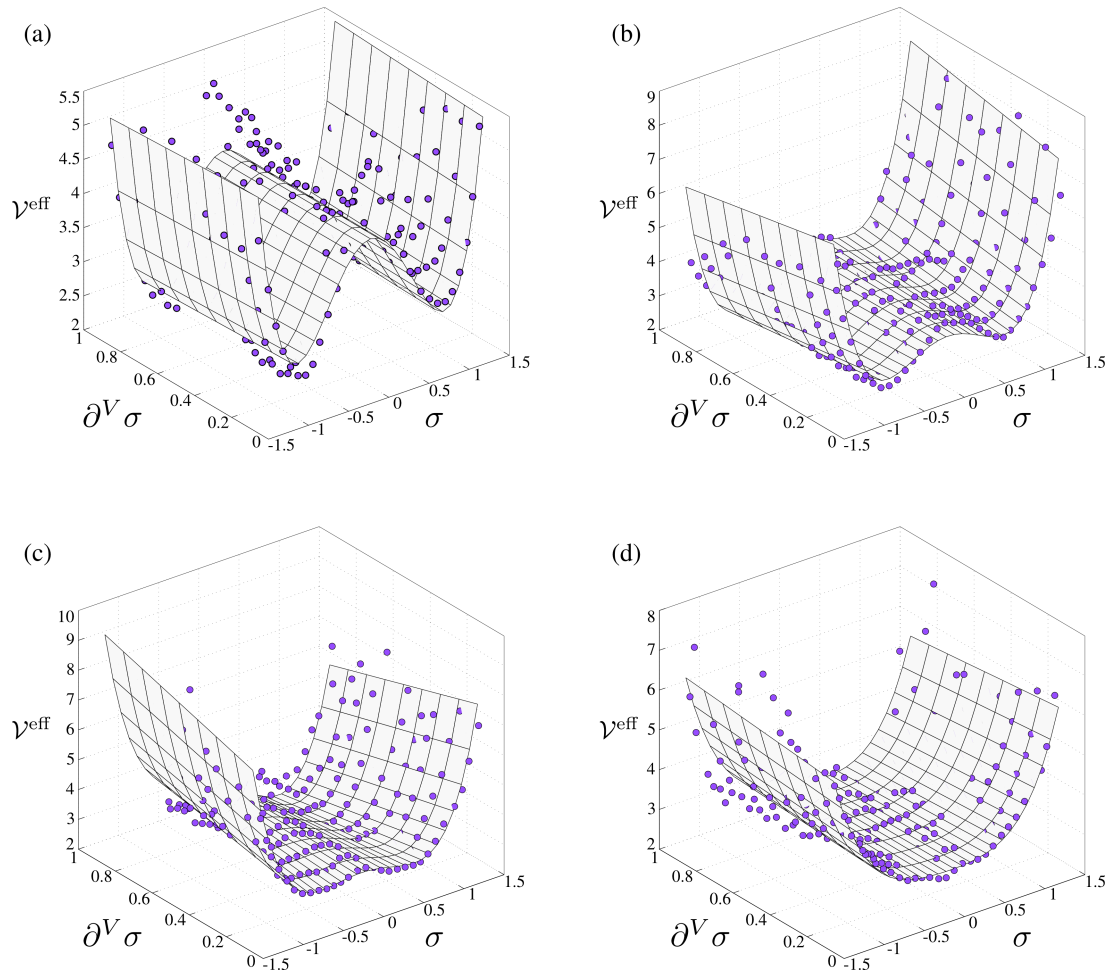


Figure 4.13: Effective vortex potential  $\mathcal{V}^{\text{eff}}$  in four movies, depending on the vortex spin  $\sigma$  and the mean neighbour spin  $\partial^V \sigma$ . Points: estimates from experiments. Surface: overall fit. Each plot represent a different lattice state. (a) Random: deep double-well potential with no interaction. (b) Antiferromagnetic: double-well potential with negative interaction  $J_V^{\text{eff}}$ . (c) Ferromagnetism: weak double-well potential with positive interaction  $J_V^{\text{eff}}$ . (d) Disordered: single-well potential with, here, a weak positive interaction.

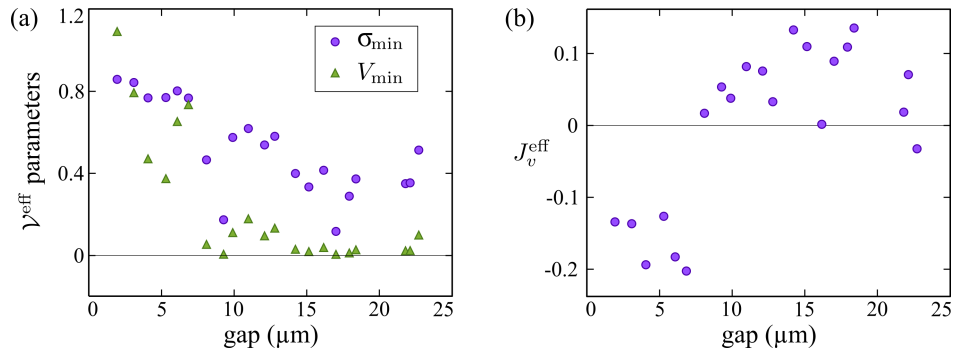


Figure 4.14: Parameter estimates for the effective potential  $V^{\text{eff}}$ , depending on the gap size. (a) Parameters of the single vortex potential:  $\sigma_{\text{min}}$ , spin of lowest energy, and  $V_{\text{min}}$ , the energy barrier. (b) Effective interaction strength  $J_V^{\text{eff}}$ . Each point is computed from the spin statistics obtained over at least six different movies.

rather than  $a_V^{\text{eff}}$  and  $b_V$ , I considered the spin of lowest energy  $\sigma_{\text{min}}$  and the energy barrier

$$\mathcal{V}_{\text{min}} = \mathcal{V}_{\text{sym}}^{\text{eff}}(0) - \mathcal{V}_{\text{sym}}^{\text{eff}}(\sigma_{\text{min}}). \quad (4.27)$$

The interaction  $J_V^{\text{eff}}$  follows the behaviour of the spin-spin correlation  $C$  (figure 4.14b). For small gaps, they are both negative, indicating that the bulk interactions  $J_V$  between bacteria dominates. When the gap increases,  $J_V^{\text{eff}}$  changes sign revealing that the interaction through the pillars  $J_P$  leads the lattice behaviour, in agreement with observations of bacteria swimming around pillars in ferromagnetic chambers. For the largest gaps, the interaction fades. This last result could not be predicted from earlier measurements. Indeed, the turbulent state could simply be due to the lack of stability of vortices. Our analysis also shows that interactions  $J_V$  and  $J_P$  either cancel each other or simply die out. Finally, I only obtained a few movies at very small gap. Although they were in a random state, they do not appear in figure 4.14.

We then found that the spin of lowest energy  $\sigma_{\text{min}}$  decreases with the gap size, from  $\approx 0.8$  to  $\approx 0.4$ . This shows that the double-well does not become a single-well at large gaps and that even in this case, pillar still have a weak stabilising effect. Yet the energy barrier  $\mathcal{V}_{\text{min}}$  quickly drops from 1.1 for the smallest gap to less than 0.2 for gaps larger than 8  $\mu\text{m}$ . Even though spins still sit in a double well, the potential profile is effectively flat. These results are in agreement with measurements of the absolute spin  $S$  (figure 4.5f).

## 4.4 Conclusion

These measurements only give a limited understanding on the self-organisation of bacterial suspensions in lattices. Francis Woodhouse is currently working on fitting the full Hamiltonian using a Langevin approach. This should allow us to have a full estimate of parameters. Of particular interest are the interactions between vortices and pillars. While I only compute  $J_V^{\text{eff}} = J_V - \frac{1}{2}J_P$ , Woodhouse's method should give us access to  $J_V$  and  $J_P$  independently.

We have so far neglected the time component of the lattice self-organisation. Indeed, the probability of finding a spin state was defined as  $p = \frac{1}{Z} \exp(-\mathcal{H}(\boldsymbol{\sigma}))$ . A more accurate description should include an effective temperature,  $\mathcal{H} = \frac{\tilde{\mathcal{H}}}{T_{\text{eff}}}$ . Note that all parameters of the system Hamiltonian are inversely proportional to the temperature:  $J_V = \frac{\tilde{J}_V}{T_{\text{eff}}}$ ,  $a_V = \frac{\tilde{a}_V}{T_{\text{eff}}}$ , etc.

Estimating  $T_{\text{eff}}$  appears to be challenging in an active suspension of bacteria. For example, the bacterial swimming speed increases with the oxygen concentration, resulting in faster variations of the lattice. Yet we do not expect the system steady state, and thus  $T_{\text{eff}}$ , to be affected by faster swimming [93, 96]. Measuring  $T_{\text{eff}}$  then requires to renormalise spins as well as time. I suspect the effective temperature to vary with the chamber geometry and the suspension state (e.g. bacterial concentration).

Nonetheless, experiments in lattice of vortices revealed unexpected complex bacterial organisation, in the form of antiferromagnetic and ferromagnetic arrangements. Interactions appear to be driven by bacteria in the bulk and at the PDMS interface, showing that confinement not only stabilises vortices but also control long-range order.

Further experiments are required to understand this system. The effect of the chambers height, cavity diameter and gap length on the stability of the circulation and on the lattice ordering would be of particular interest. Further studies could also focus on the dynamics of ferromagnetic and antiferromagnetic domain formation.

Of particular interest will be the analyses of hydrodynamic interactions and the exact role of bacteria swimming along interfaces. Simulations, as those presented in chapter 3, are probably the method of choice to study the suspension organisation at the microscopic level.

Finally we have presented an Ising model to describe the lattice order. This ap-

proach has been successful in measuring effective interactions between adjacent cavities and in estimating vortex potentials, and we expect to obtain more detailed and accurate results in the near future. This Ising model is consistent with the current trend in active matter to use statistical physics tools in order to describe self-propelled particle suspensions [153]. Examples include Boltzmann equations [154] and the definition of an active pressure [155]. This Ising model could be useful to predict lattice ordering in geometries that are currently difficult to realise experimentally. One could look at 3-dimensional square lattices with either spherical or flattened cavities for example.



# Chapter 5

## Conclusion

The number of publications on active matter has exploded in the past decade. The field has evolved from simple experiments in unconfined chambers [135, 156] to well-controlled systems in complex environments [32, 93, 127]. Likewise, theories have matured from the minimal approach taken for the Vicsek simulations [99] to models able to reproduce interactions accurately and intricate suspension behaviours [96, 154].

A guiding thread in this thesis is the role played by interfaces and confinement in the self-organisation of dense bacterial suspensions. Solid and liquid interfaces are well-known to affect the swimming behaviour of single cells, generating trapping [113, 114], modifying the bacteria-driven fluid flows [109] and cell trajectories [119, 120]. Yet dense suspensions under confinement have rarely been considered.

This thesis presented three different confining topologies: flattened drops, race-tracks and lattices of cavities. Beyond merely listing new phenomena, we have tried to explain the suspension behaviour from the microscopic level and to obtain a better understanding of bacterial motion.

### Flattened Drops

I have first proposed a novel experimental setup in which a concentrated suspension is mixed with oil to form an emulsion and then squeezed between two coverslips. In chambers that are  $25\mu\text{m}$  in height and  $30$  to  $70\mu\text{m}$  in diameter, the suspension forms a single stable vortex state. Unlike unconfined suspensions which exhibit quasi-turbulent motion, I found the bacterial flow in flattened drops to persist over several minutes, until oxygen depletion. Furthermore, while the cell orientation and direction

of motion are uncorrelated in unconfined chambers [31], bacteria in drops align in a helical pattern. Measurements of the mean cell orientation show the pattern to depend on the drop diameter and thus on the curvature at the interface with the surrounding oil.

But the most striking feature was bacteria at the edge of the drop moving against the bulk circulation. This phenomena was observed in all drops, even with smaller or larger diameters, and consisted of a single layer of cells at the very edge of the drop. This observation strongly contrasts with the classical picture of collective motion, in which all swimmers locally share a common direction of motion. Indeed, no previous experimental or theoretical work had reported or predicted such a behaviour.

### **Hydrodynamic Interactions**

To unravel the mystery of double circulation, I developed a new experimental technique which simultaneously measures the swimming and motion directions of bacteria whose flagella and body have been fluorescently labelled. Measurements reveal that all cells are aligned in the same direction, but while bacteria at the edge are moving forwards, those in the bulk are moving against their swimming direction.

To fully understand this self-organisation, Enkeleida Lushi developed a simulation method which includes steric and hydrodynamic interactions, along with realistic boundary conditions. Simulations are able to reproduce the bacterial motion and showed that cells close to the edge (and their interfacial images) generate a net fluid flow in the drop, against the common swimming direction. The motion of swimmers in the bulk is then dominated by advection, explaining the backward motion observed with fluorescent bacteria.

The role of fluid flows in the self-organisation of bacterial suspensions has been the subject of much debate. While some researchers support the idea that steric interactions drive the quasi-turbulent motion in unconfined chambers [90], others have shown the suspension to be unstable under hydrodynamic interactions only [89]. Moreover, fluid flows have been shown to disassemble bacterial swarms [91]. Additionally, dense suspensions can reach velocities an order of magnitude faster than single cells [93]. This acceleration has been attributed to short-range hydrodynamic effects, that increases the swimming efficiency [7], but could as well result from advection by long-range fluid flows. Experiments that show bacterial orientation and direction of motion

to be uncorrelated in unconfined chambers [31] and anticorrelated in drops, suggest the role of hydrodynamic interactions to be more important than often represented.

### **Simulations Improvements**

On a more technical side, simulations presented in this thesis do not propose a new method in that steric repulsion, hydrodynamic interactions, and interfaces have already been modelled, but they are the first to combine all these ingredients to obtain a more realistic representation of the suspension. Improvements of the model can take several directions. First, simulations were limited to a 2D domain. Expanding them into 3D requires significantly improving the computation efficiency and probably introducing some new approximations.

Moreover, we have only presented simple geometries, circular and linear, which are easy to model with a system of images. Including more complex boundary geometries, as in a lattice of vortices, would necessitate developing other computation methods.

Furthermore, hydrodynamic interactions are computed from the sum of fluid flows generated by isolated swimmers. Yet bacteria take up to 20% of the volume fraction and can significantly affect the flow pattern generated by neighbours. Considering the presence of the suspension, its porosity or effective viscosity [157] will certainly improve the accuracy of estimated fluid flows.

Finally, interactions at the microscopic level between flagella of different swimmers could modify the swimming mechanism. In that case, the fluid flows generated in dense suspensions could differ significantly from those predicted by the idealised stresslet model. Knowing which details are relevant to model bacterial suspensions will certainly improve the efficiency of simulations and our understanding of active matter.

### **Racetracks**

The second experimental chambers I considered were racetracks. Dimensions are comparable to those of flattened drops (height around  $20\mu\text{m}$ , width on the order of tens of microns), except for the length which could be more than several millimetres. The suspension is thus only confined in two directions, rather than three, as in the case of drops. Yet the effect of interfaces remains comparable.

If the channel width is smaller than  $70\mu\text{m}$ , the suspension forms a persistent wavy stream, comparable to jets observed in unconfined bacterial suspensions. Swimmers at the PDMS and glass interfaces move in opposite direction to the bulk circulation. Moreover fluorescent bacteria and simulations show that cells inside the channel have a biased orientation against the fluid flow. Racetrack experiments could then be solely thought of as a confirmation of the mechanism driving self-organisation in drops.

Nevertheless, these experiments brought at least two significant results. The first regards the correlation length. In order to quantify the self-organisation of active matter, researchers usually compute the spatial correlation of the flow. This function often decreases monotonically with distance. The decay then gives a typical length scale sometimes linked to the swirl radius. Confinement in racetracks shows that there are actually two length scales, that of the vortices and a persistence length. Comparison with other papers shows that the two length scales can vary independently. For example, the persistence length increases with the bacterial concentration while the swirl size remains constant from dilute to the densest suspensions [32]. Further studies which would independently measure the vortex size and persistence length, are necessary to fully understand these relations. These new results could then be compared to theoretical predictions to confirm the role of steric and hydrodynamic interactions in bacterial self-organisation.

The second important finding refers to the effect of interfaces. Not only do they stabilise the suspension motion into a vortex (in flattened drops) or a stream (in racetracks), but the flow profiles show that they also contribute significantly to the bulk circulation. The swimming of a single bacterium in the bulk generates a stresslet disturbance, but no net flow. However, when placed next to a surface, the no-slip or free-shear boundary condition yields a net fluid flow against the swimming direction. Boundary currents thus play a central role in the bulk circulation, setting the direction of bacteria and, on a larger scale, of vortices.

### **Lattices of vortices**

The last experimental chambers also rely on boundary currents, yielding unexpected circulation ordering. Bacteria were injected into a network of cavities, inside each of which they could form a more or less stable vortex, interacting with adjacent cavities through connections (*gaps*). Depending on the number of connections and on their

shape, interactions can result in an antiferromagnetic or ferromagnetic array of vortices. These two states appear to be driven by distinct circulation patterns of bacteria at PDMS surfaces. In the first case, bacteria predominantly stay in one cavity, long-range interactions dominate, so that swimmers on each side of the gap move in the same direction, yielding opposite spins. In the second, bacteria can cross the connection to move continuously around pillars, generating spins of same sign.

Interactions with surfaces have a dramatic effect on other condensed matter systems. Surface texture can for example set the orientation of liquid crystals at the boundary, affecting the organisation in the bulk [158]. Likewise, quantum Hall effect is governed by currents of electrons at edges [159]. In confined bacterial suspensions, motion at surfaces appears to dictate the overall circulation. The suspension behaviour could then be predicted from edge currents, integrated for instance into a Green's function.

We finally presented an Ising model that reproduces the four states observed in square lattices. By renormalisation of the grid, we have managed to fit simplified energy profiles and measure effective parameters. Further analysis should provide a complete estimate of the Hamiltonian of the system (interaction strength, single vortex potential, temperature, etc) and shed light on the self-organisation mechanism in lattices of vortices.

### **Future work**

Experiments under confinement have shown that many active behaviours are still to be discovered. I wish for this approach to be considered by the community. I am already aware of three groups that started looking at bacteria in drops after we published results on flattened drops [1]. These new works consider different drops shapes (larger or spherical) and other bacterial species (*E. coli*, *Pseudomonas aeruginosa*) [139]. Owing to the variety between species in shapes (e.g. aspect ratio, length) and swimming behaviours (e.g. number of flagella, run-and-tumble), the suspension could exhibit surprising behaviours unobserved with *B.subtilis*.

Likewise, after I started experiments in racetracks, Bricard *et al.* [127] presented a similar setup with rolling colloids instead of bacteria. These colloids are also subject to steric and hydrodynamic forces but present a distinct collective motion. Using different active systems allows various interactions to be examined. An other approach is to mix

active or passive material such as bacteria in liquid crystals [160] and bristle-bots in granules [41].

A final perspective will be to reproduce systems akin to natural environments. One could then focus on two aspects. First, natural environments are populated with numerous microorganisms species. Chemical and physical interactions between them could result in particular collective behaviour such as attraction or repulsion patterns, as in the case of symbiotic or competing species [161]. Moreover, in clonal populations of bacteria, individuals can present different phenotypes, swimming or vegetative for example [64]. The heterogeneity of the microbial population could then result in complex collective motion and phase transitions [91]. The second aspect will be to make realistic boundary conditions and topologies. Natural environments could be presented as a porous structure with numerous connected cavities and channels. Preliminary experiments in 8-shaped racetracks show that bacterial trajectories are determined by the precise chamber geometry. Baroque arrangements of cavities and channels could, thus, modulate and control the collective motion of microorganisms.

# References

- [1] Hugo Wioland, Francis G Woodhouse, Jörn Dunkel, John O Kessler, and Raymond E Goldstein. Confinement stabilizes a bacterial suspension into a spiral vortex. *Physical Review Letters*, 110(26):268102, 2013. [i](#), [37](#), [41](#), [119](#)
- [2] Enkeleida Lushi, Hugo Wioland, and Raymond E Goldstein. Fluid flows created by swimming bacteria drive self-organization in confined suspensions. *Proceedings of the National Academy of Sciences*, page 201405698, 2014. [ii](#), [70](#), [77](#), [79](#), [81](#), [82](#)
- [3] Hugo Wioland, Enkelaida Lushi, and Raymond E Goldstein. Spontaneous directional collective motion of swimming bacteria in racetracks. 2015. [ii](#), [50](#), [51](#), [52](#), [54](#), [72](#)
- [4] Pierre-Joseph Proudhon. *Les Confessions d'un révolutionnaire pour servir à l'histoire de la Révolution de Février*. Garnier frères, 1851. [1](#)
- [5] P Stoodley, I Dodds, JD Boyle, and HM Lappin-Scott. Influence of hydrodynamics and nutrients on biofilm structure. *Journal of Applied Microbiology*, 85(S1):19S–28S, 1998. [1](#), [2](#)
- [6] Daniel B Kearns, Frances Chu, Steven S Branda, Roberto Kolter, and Richard Losick. A master regulator for biofilm formation by *Bacillus subtilis*. *Molecular microbiology*, 55(3):739–749, 2005. [1](#), [2](#), [8](#)
- [7] Henricus H Wensink, Jörn Dunkel, Sebastian Heidenreich, Knut Drescher, Raymond E Goldstein, Hartmut Löwen, and Julia M Yeomans. Meso-scale turbulence in living fluids. *Proceedings of the National Academy of Sciences*,

- 109(36):14308–14313, 2012. [1](#), [2](#), [3](#), [15](#), [17](#), [18](#), [21](#), [23](#), [31](#), [32](#), [40](#), [46](#), [73](#), [77](#), [116](#)
- [8] Bernard J Crespi. The evolution of social behavior in microorganisms. *TRENDS in Ecology & Evolution*, 16(4):178–183, 2001. [1](#)
- [9] Eshel Ben Jacob, Israela Becker, Yoash Shapira, and Herbert Levine. Bacterial linguistic communication and social intelligence. *TRENDS in Microbiology*, 12(8):366–372, 2004. [1](#)
- [10] Stuart A West, Ashleigh S Griffin, Andy Gardner, and Stephen P Diggle. Social evolution theory for microorganisms. *Nature Reviews Microbiology*, 4(8):597–607, 2006. [1](#)
- [11] W Claiborne Fuqua, Stephen C Winans, and E Peter Greenberg. Quorum sensing in bacteria: the luxr-luxI family of cell density-responsive transcriptional regulators. *Journal of Bacteriology*, 176(2):269, 1994. [1](#), [2](#)
- [12] Dale Kaiser. Signaling in myxobacteria. *Annual Review of Microbiology*, 58:75–98, 2004. [1](#), [2](#), [3](#)
- [13] Christopher M Waters and Bonnie L Bassler. Quorum sensing: cell-to-cell communication in bacteria. *The Annual Review of Cell and Developmental Biology*, 21:319–346, 2005. [1](#)
- [14] Daniel López and Roberto Kolter. Extracellular signals that define distinct and coexisting cell fates in *Bacillus subtilis*. *FEMS Microbiology Reviews*, 34(2):134–149, 2010. [1](#), [2](#)
- [15] Daniel López, Hera Vlamakis, Richard Losick, and Roberto Kolter. Cannibalism enhances biofilm development in *Bacillus subtilis*. *Molecular Microbiology*, 74(3):609–618, 2009. [1](#), [2](#)
- [16] James N Wilking, Vasily Zaburdaev, Michael De Volder, Richard Losick, Michael P Brenner, and David A Weitz. Liquid transport facilitated by channels in *Bacillus subtilis* biofilms. *Proceedings of the National Academy of Sciences*, 110(3):848–852, 2013. [1](#), [5](#), [60](#)

- [17] Matthew AA Grant, Bartłomiej Waclaw, Rosalind J Allen, and Pietro Cicuti. The role of mechanical forces in the planar-to-bulk transition in growing *Escherichia coli* microcolonies. *Journal of The Royal Society Interface*, 2014. [1](#), [5](#)
- [18] David Dubnau. Dna uptake in bacteria. *Annual Reviews in Microbiology*, 53(1):217–244, 1999. [1](#)
- [19] Masahiro Ohgiwari, Mitsugu Matsushita, and Tohey Matsuyama. Morphological changes in growth phenomena of bacterial colony patterns. *Journal of the Physical Society of Japan*, 61(3):816–822, 1992. [1](#), [4](#)
- [20] Gil Ariel, Adi Shklarsh, Oren Kalisman, Colin Ingham, and Eshel Ben-Jacob. From organized internal traffic to collective navigation of bacterial swarms. *New Journal of Physics*, 15(12):125019, 2013. [1](#)
- [21] Jerry M Kuner and Dale Kaiser. Fruiting body morphogenesis in submerged cultures of *Myxococcus xanthus*. *Journal of bacteriology*, 151(1):458–461, 1982. [2](#), [3](#)
- [22] José Eduardo González-Pastor. Cannibalism: a social behavior in sporulating *Bacillus subtilis*. *FEMS Microbiology Reviews*, 35(3):415–424, 2011. [2](#)
- [23] JT Bonner and LJ Savage. Evidence for the formation of cell aggregates by chemotaxis in the development of the slime mold *Dictyostelium discoideum*. *Journal of Experimental Zoology*, 106(1):1–26, 1947. [2](#), [3](#)
- [24] Ralph Beckers, Jean-Louis Deneubourg, and Simon Goss. Trails and u-turns in the selection of a path by the ant *Iasius niger*. *Journal of theoretical biology*, 159(4):397–415, 1992. [2](#)
- [25] Michele Ballerini, Nicola Cabibbo, Raphael Candelier, Andrea Cavagna, Evaristo Cisbani, Irene Giardina, Alberto Orlandi, Giorgio Parisi, Andrea Procaccini, Massimiliano Viale, and Vladimir Zdravkovic. Empirical investigation of starling flocks: a benchmark study in collective animal behaviour. *Animal Behaviour*, 76(1):201–215, 2008. [2](#)

- [26] Charlotte K Hemelrijk and Hanno Hildenbrandt. Schools of fish and flocks of birds: their shape and internal structure by self-organization. *Interface Focus*, page rsfs.2012.0025, 2012. [2](#)
- [27] Sriram Ramaswamy. The mechanics and statistics of active matter. *Annual Review of Condensed Matter Physics*, 1:323–345, 2010. [2](#)
- [28] DM Hunter, L McCulloch, and PA Spurgin. Aerial detection of nymphal bands of the australian plague locust (*chortoicetes terminifera* (walker))(orthoptera: Acrididae). *Crop Protection*, 27(1):118–123, 2008. [2](#)
- [29] Jerome Buhl, David JT Sumpter, Iain D Couzin, Joe J Hale, Emma Despland, ER Miller, and Steve J Simpson. From disorder to order in marching locusts. *Science*, 312(5778):1402–1406, 2006. [2](#), [27](#)
- [30] Luis H Cisneros, Ricardo Cortez, Christopher Dombrowski, Raymond E Goldstein, and John O Kessler. Fluid dynamics of self-propelled microorganisms, from individuals to concentrated populations. *Experiments in Fluids*, 43(5):737–753, 2007. [3](#), [15](#), [17](#), [31](#)
- [31] Andrey Sokolov, Igor S Aranson, John O Kessler, and Raymond E Goldstein. Concentration dependence of the collective dynamics of swimming bacteria. *Physical Review Letters*, 98(15):158102, 2007. [3](#), [15](#), [17](#), [18](#), [31](#), [46](#), [71](#), [116](#), [117](#)
- [32] J Gachelin, A Rousselet, A Lindner, and E Clement. Collective motion in an active suspension of *Escherichia coli* bacteria. *New Journal of Physics*, 16(2):025003, 2014. [3](#), [15](#), [17](#), [18](#), [31](#), [32](#), [46](#), [115](#), [118](#)
- [33] NA Hill and TJ Pedley. Bioconvection. *Fluid Dynamics Research*, 37(1):1–20, 2005. [3](#)
- [34] Ingmar H Riedel, Karsten Kruse, and Jonathon Howard. A self-organized vortex array of hydrodynamically entrained sperm cells. *Science*, 309(5732):300–303, 2005. [3](#)

- [35] Tim Sanchez, Daniel TN Chen, Stephen J DeCamp, Michael Heymann, and Zvonimir Dogic. Spontaneous motion in hierarchically assembled active matter. *Nature*, 491(7424):431–434, 2012. [3](#), [22](#), [27](#)
- [36] Felix C Keber, Etienne Loiseau, Tim Sanchez, Stephen J DeCamp, Luca Giomi, Mark J Bowick, M Cristina Marchetti, Zvonimir Dogic, and Andreas R Bausch. Topology and dynamics of active nematic vesicles. *Science*, 345(6201):1135–1139, 2014. [3](#), [22](#)
- [37] Tariq Butt, Tabish Mufti, Ahmad Humayun, Peter B Rosenthal, Sohaib Khan, Shahid Khan, and Justin E Molloy. Myosin motors drive long range alignment of actin filaments. *Journal of Biological Chemistry*, 285(7):4964–4974, 2010. [3](#)
- [38] Volker Schaller, Christoph Weber, Christine Semmrich, Erwin Frey, and Andreas R Bausch. Polar patterns of driven filaments. *Nature*, 467(7311):73–77, 2010. [3](#)
- [39] Julien Deseigne, Sébastien Léonard, Olivier Dauchot, and Hugues Chaté. Vibrated polar disks: spontaneous motion, binary collisions, and collective dynamics. *Soft Matter*, 8(20):5629–5639, 2012. [3](#), [26](#), [43](#), [45](#), [79](#)
- [40] L Giomi, N Hawley-Weld, and L Mahadevan. Swarming, swirling and stasis in sequestered bristle-bots. *Proceedings of the Royal Society A: Mathematical, Physical and Engineering Science*, 469(2151):20120637, 2013. [3](#), [26](#), [43](#), [45](#), [79](#)
- [41] Nitin Kumar, Harsh Soni, Sriram Ramaswamy, and AK Sood. Flocking at a distance in active granular matter. *arXiv preprint arXiv:1402.4262*, 2014. [3](#), [43](#), [45](#), [120](#)
- [42] Andreas Walther and Axel HE Müller. Janus particles. *Soft Matter*, 4(4):663–668, 2008. [3](#)
- [43] Ivo Buttinoni, Julian Bialké, Felix Kümmel, Hartmut Löwen, Clemens Bechinger, and Thomas Speck. Dynamical clustering and phase separation in suspensions of self-propelled colloidal particles. *Physical Review Letters*, 110(23):238301, 2013. [3](#)

- [44] Jørgen Henriksen. Bacterial surface translocation: a survey and a classification. *Bacteriological reviews*, 36(4):478, 1972. [4](#), [65](#), [83](#)
- [45] Ken F Jarrell and Mark J McBride. The surprisingly diverse ways that prokaryotes move. *Nature Reviews Microbiology*, 6(6):466–476, 2008. [4](#)
- [46] Daniel B Kearns. A field guide to bacterial swarming motility. *Nature Reviews Microbiology*, 8(9):634–644, 2010. [4](#), [65](#), [83](#)
- [47] Saverio E Spagnolie and Eric Lauga. Comparative hydrodynamics of bacterial polymorphism. *Physical Review Letters*, 106(5):058103, 2011. [4](#), [7](#)
- [48] Sarah B Guttenplan, Sidney Shaw, and Daniel B Kearns. The cell biology of peritrichous flagella in *Bacillus subtilis*. *Molecular Microbiology*, 87(1):211–229, 2013. [4](#), [8](#), [67](#), [68](#)
- [49] Kurt M Ehlers, AD Samuel, Howard C Berg, and Richard Montgomery. Do cyanobacteria swim using traveling surface waves? *Proceedings of the National Academy of Sciences*, 93(16):8340–8343, 1996. [4](#)
- [50] Aravinthan DT Samuel, Jennifer D Petersen, and Thomas S Reese. Envelope structure of synechococcus sp. wh8113, a nonflagellated swimming cyanobacterium. *BMC Microbiology*, 1(1):4, 2001. [4](#)
- [51] Jeffrey M Skerker and Howard C Berg. Direct observation of extension and retraction of type iv pili. *Proceedings of the National Academy of Sciences*, 98(12):6901–6904, 2001. [5](#)
- [52] Mark J McBride. Bacterial gliding motility: multiple mechanisms for cell movement over surfaces. *Annual Reviews in Microbiology*, 55(1):49–75, 2001. [5](#)
- [53] Tâm Mignot, Joshua W Shaevitz, Patricia L Hartzell, and David R Zusman. Evidence that focal adhesion complexes power bacterial gliding motility. *Science*, 315(5813):853–856, 2007. [5](#)
- [54] Robert M Macnab. How bacteria assemble flagella. *Annual Reviews in Microbiology*, 57(1):77–100, 2003. [5](#), [7](#), [8](#)

- [55] Linda Turner, Alan S Stern, and Howard C Berg. Growth of flagellar filaments of *Escherichia coli* is independent of filament length. *Journal of Bacteriology*, 194(10):2437–2442, 2012. [5](#)
- [56] Koji Yonekura, Saori Maki-Yonekura, and Keiichi Namba. Complete atomic model of the bacterial flagellar filament by electron cryomicroscopy. *Nature*, 424(6949):643–650, 2003. [5](#)
- [57] CR Calladine. Change of waveform in bacterial flagella: the role of mechanics at the molecular level. *Journal of Molecular Biology*, 118(4):457–479, 1978. [7](#)
- [58] Linda Turner, William S Ryu, and Howard C Berg. Real-time imaging of fluorescent flagellar filaments. *Journal of Bacteriology*, 182(10):2793–2801, 2000. [7](#), [9](#), [10](#)
- [59] Yoshiyuki Sowa and Richard M Berry. Bacterial flagellar motor. *Quarterly Reviews of Biophysics*, 41(02):103–132, 2008. [7](#)
- [60] Howard C Berg. The rotary motor of bacterial flagella. *Biochemistry*, 72(1):19, 2003. [8](#)
- [61] Junhua Yuan, Karen A Fahrner, and Howard C Berg. Switching of the bacterial flagellar motor near zero load. *Journal of Molecular Biology*, 390(3):394–400, 2009. [8](#)
- [62] Fadel A Samatey, Hideyuki Matsunami, Katsumi Imada, Shigehiro Nagashima, Tanvir R Shaikh, Dennis R Thomas, James Z Chen, David J DeRosier, Akio Kitao, and Keiichi Namba. Structure of the bacterial flagellar hook and implication for the molecular universal joint mechanism. *Nature*, 431(7012):1062–1068, 2004. [8](#)
- [63] Robert M Macnab. Genetics and biogenesis of bacterial flagella. *Annual Review of Genetics*, 26(1):131–158, 1992. [8](#)
- [64] Daniel B Kearns and Richard Losick. Cell population heterogeneity during growth of *Bacillus subtilis*. *Genes & Development*, 19(24):3083–3094, 2005. [8](#), [32](#), [120](#)

- [65] Ali Houry, Michel Gohar, Julien Deschamps, Ekaterina Tischenko, Stéphane Aymerich, Alexandra Gruss, and Romain Briandet. Bacterial swimmers that infiltrate and take over the biofilm matrix. *Proceedings of the National Academy of Sciences*, 109(32):13088–13093, 2012. [8](#)
- [66] T Nishihara and E Freese. Motility of *Bacillus subtilis* during growth and sporulation. *Journal of Bacteriology*, 123(1):366–371, 1975. [8](#), [32](#)
- [67] Nicholas C Darnton, Linda Turner, Svetlana Rojevsky, and Howard C Berg. On torque and tumbling in swimming *Escherichia coli*. *Journal of Bacteriology*, 189(5):1756–1764, 2007. [8](#), [9](#), [10](#)
- [68] Luis Cisneros, Christopher Dombrowski, Raymond E Goldstein, and John O Kessler. Reversal of bacterial locomotion at an obstacle. *Physical Review E*, 73(3):030901, 2006. [9](#), [68](#)
- [69] Robert M Macnab. Bacterial flagella rotating in bundles: a study in helical geometry. *Proceedings of the National Academy of Sciences*, 74(1):221–225, 1977. [9](#)
- [70] Shang Yik Reigh, Roland G Winkler, and Gerhard Gompper. Synchronization and bundling of anchored bacterial flagella. *Soft Matter*, 8(16):4363–4372, 2012. [9](#)
- [71] PJA Janssen and MD Graham. Coexistence of tight and loose bundled states in a model of bacterial flagellar dynamics. *Physical Review E*, 84(1):011910, 2011. [9](#)
- [72] Howard C Berg and Douglas A Brown. Chemotaxis in *Escherichia coli* analysed by three-dimensional tracking. *Nature*, 239(5374):500–504, 1972. [10](#)
- [73] Christopher V Rao, George D Glekas, and George W Ordal. The three adaptation systems of *Bacillus subtilis* chemotaxis. *TRENDS in Microbiology*, 16(10):480–487, 2008. [10](#)
- [74] Mehdi Molaie, Michael Barry, Roman Stocker, and Jian Sheng. Failed escape: Solid surfaces prevent tumbling of *Escherichia coli*. *Physical Review Letters*, 113(6):068103, 2014. [10](#), [26](#)

- [75] Hilding Faxén. Der widerstand gegen die bewegung einer starren kugel in einer zähen flüssigkeit, die zwischen zwei parallelen ebenen wänden eingeschlossen ist. *Annalen der Physik*, 373(10):89–119, 1922. [11](#), [14](#)
- [76] GG Stokes. On the effect of fluids on the motion of pendulums. *Transactions of the Cambridge Philosophical Society*, 9(8), 1851. [12](#)
- [77] JR Blake and AT Chwang. Fundamental singularities of viscous flow. *Journal of Engineering Mathematics*, 8(1):23–29, 1974. [12](#), [75](#)
- [78] Knut Drescher, Jörn Dunkel, Luis H Cisneros, Sujoy Ganguly, and Raymond E Goldstein. Fluid dynamics and noise in bacterial cell–cell and cell–surface scattering. *Proceedings of the National Academy of Sciences*, 108(27):10940–10945, 2011. [12](#), [15](#), [23](#), [24](#)
- [79] Marco Polin, Idan Tuval, Knut Drescher, Jerry P Gollub, and Raymond E Goldstein. Chlamydomonas swims with two “gears” in a eukaryotic version of run-and-tumble locomotion. *Science*, 325(5939):487–490, 2009. [12](#)
- [80] Knut Drescher, Raymond E Goldstein, Nicolas Michel, Marco Polin, and Idan Tuval. Direct measurement of the flow field around swimming microorganisms. *Physical Review Letters*, 105(16):168101, 2010. [14](#)
- [81] JM Rallison. Note on the faxen relations for a particle in stokes flow. *Journal of Fluid Mechanics*, 88(03):529–533, 1978. [14](#)
- [82] George B Jeffery. The motion of ellipsoidal particles immersed in a viscous fluid. *Proceedings of the Royal Society of London. Series A, Containing papers of a mathematical and physical character*, pages 161–179, 1922. [14](#), [74](#)
- [83] Roberto Rusconi, Jeffrey S Guasto, and Roman Stocker. Bacterial transport suppressed by fluid shear. *Nature Physics*, pages 212–217, 2014. [14](#)
- [84] Kyriacos C Leptos, Jeffrey S Guasto, Jerry P Gollub, Adriana I Pesci, and Raymond E Goldstein. Dynamics of enhanced tracer diffusion in suspensions of swimming eukaryotic microorganisms. *Physical Review Letters*, 103(19):198103, 2009. [14](#)

- [85] Gastón Mino, Thomas E Mallouk, Thierry Darnige, Mauricio Hoyos, Jeremi Dauchet, Jocelyn Dunstan, Rodrigo Soto, Yang Wang, Annie Rousselet, and Eric Clement. Enhanced diffusion due to active swimmers at a solid surface. *Physical Review Letters*, 106(4):048102, 2011. [14](#)
- [86] Takuji Ishikawa, Go Sekiya, Yohsuke Imai, and Takami Yamaguchi. Hydrodynamic interactions between two swimming bacteria. *Biophysical Journal*, 93(6):2217–2225, 2007. [14](#)
- [87] A Kaiser, K Popowa, HH Wensink, and H Löwen. Capturing self-propelled particles in a moving microwedge. *Physical Review E*, 88(2):022311, 2013. [15](#)
- [88] Andreas Kaiser, Anton Peshkov, Andrey Sokolov, Borge ten Hagen, Hartmut Löwen, and Igor S Aranson. Transport powered by bacterial turbulence. *Physical Review Letters*, 112(15):158101, 2014. [15](#), [17](#)
- [89] David Saintillan and Michael J Shelley. Orientational order and instabilities in suspensions of self-locomoting rods. *Physical Review Letters*, 99(5):058102, 2007. [15](#), [23](#), [58](#), [116](#)
- [90] Shawn D Ryan, Andrey Sokolov, Leonid Berlyand, and Igor S Aranson. Correlation properties of collective motion in bacterial suspensions. *New journal of physics*, 15(10):105021, 2013. [15](#), [23](#), [73](#), [116](#)
- [91] Ricard Matas-Navarro, Ramin Golestanian, Tanniemola B Liverpool, and Suzanne M Fielding. Hydrodynamic suppression of phase separation in active suspensions. *Physical Review E*, 90(3):032304, 2014. [15](#), [23](#), [83](#), [116](#), [120](#)
- [92] A. Sokolov, R.E. Goldstein, F.I. Feldchtein, and I.S. Aranson. Enhanced mixing and spatial instability in concentrated bacterial suspensions. *Physical Review E*, 80(3):031903, 2009. [15](#), [17](#), [19](#), [23](#), [31](#)
- [93] Andrey Sokolov and Igor S Aranson. Physical properties of collective motion in suspensions of bacteria. *Physical Review Letters*, 109(24):248109, 2012. [15](#), [17](#), [18](#), [31](#), [112](#), [115](#), [116](#)

- [94] Petr Denissenko, Vasily Kantsler, David J Smith, and Jackson Kirkman-Brown. Human spermatozoa migration in microchannels reveals boundary-following navigation. *Proceedings of the National Academy of Sciences*, 109(21):8007–8010, 2012. [15](#)
- [95] W Thielicke and EJ Stamhuis. Pivlab – towards user-friendly, affordable and accurate digital particle image velocimetry in matlab. *Journal of Open Research Software*, 2(1):e30, 2014. [16](#)
- [96] Jörn Dunkel, Sebastian Heidenreich, Knut Drescher, Henricus H Wensink, Markus Bär, and Raymond E Goldstein. Fluid dynamics of bacterial turbulence. *Physical Review Letters*, 110(22):228102, 2013. [17](#), [18](#), [21](#), [31](#), [112](#), [115](#)
- [97] Idan Tuval, Luis Cisneros, Christopher Dombrowski, Charles W Wolgemuth, John O Kessler, and Raymond E Goldstein. Bacterial swimming and oxygen transport near contact lines. *Proceedings of the National Academy of Sciences*, 102(7):2277–2282, 2005. [19](#), [23](#)
- [98] John Toner, Yuhai Tu, and Sriram Ramaswamy. Hydrodynamics and phases of flocks. *Annals of Physics*, 318(1):170–244, 2005. [19](#), [20](#), [21](#)
- [99] Tamás Vicsek, András Czirók, Eshel Ben-Jacob, Inon Cohen, and Ofer Shochet. Novel type of phase transition in a system of self-driven particles. *Physical Review Letters*, 75(6):1226, 1995. [19](#), [20](#), [22](#), [73](#), [115](#)
- [100] John Toner and Yuhai Tu. Long-range order in a two-dimensional dynamical xy model: how birds fly together. *Physical Review Letters*, 75(23):4326, 1995. [19](#)
- [101] H Chaté, F Ginelli, G Grégoire, F Peruani, and F Raynaud. Modeling collective motion: variations on the vicsek model. *The European Physical Journal B-Condensed Matter and Complex Systems*, 64(3):451–456, 2008. [20](#)
- [102] J Swift and Pierre C Hohenberg. Hydrodynamic fluctuations at the convective instability. *Physical Review A*, 15(1):319, 1977. [21](#)
- [103] Miha Ravnik and Julia M Yeomans. Confined active nematic flow in cylindrical capillaries. *Physical Review Letters*, 110(2):026001, 2013. [22](#), [47](#), [85](#)

- [104] Sumesh P Thampi, Ramin Golestanian, and Julia M Yeomans. Instabilities and topological defects in active nematics. *EPL (Europhysics Letters)*, 105(1):18001, 2014. [22](#)
- [105] SM Fielding, D Marenduzzo, and ME Cates. Nonlinear dynamics and rheology of active fluids: Simulations in two dimensions. *Physical Review E*, 83(4):041910, 2011. [22](#), [47](#), [85](#)
- [106] Nigel J Mottram and Christopher JP Newton. Introduction to q-tensor theory. *arXiv preprint arXiv:1409.3542*, 2014. [22](#)
- [107] Sumesh P Thampi, Ramin Golestanian, and Julia M Yeomans. Screened hydrodynamics in an active nematic. *arXiv preprint arXiv:1407.1211*, 2014. [22](#)
- [108] SA Edwards and JM Yeomans. Spontaneous flow states in active nematics: A unified picture. *EPL (Europhysics Letters)*, 85(1):18008, 2009. [22](#)
- [109] Adrien Lefauve and David Saintillan. Globally aligned states and hydrodynamic traffic jams in confined suspensions of active asymmetric particles. *Physical Review E*, 89(2):021002, 2014. [23](#), [115](#)
- [110] Alan Cheng Hou Tsang and Eva Kanso. Flagella-induced transitions in the collective behavior of confined microswimmers. *arXiv preprint arXiv:1405.1148*, 2014. [23](#)
- [111] Alan Cheng Hou Tsang and Eva Kanso. Circularly-confined microswimmers exhibit multiple global patterns. *arXiv preprint arXiv:1411.3311*, 2014. [23](#)
- [112] Julie A Theriot and Timothy J Mitchison. The rate of actin based motility of intracellular listeria monocytogenes equals the rate of actin polymerization. *Nature*, 357:21, 1992. [24](#)
- [113] Allison P Berke, Linda Turner, Howard C Berg, and Eric Lauga. Hydrodynamic attraction of swimming microorganisms by surfaces. *Physical Review Letters*, 101(3):038102, 2008. [24](#), [46](#), [115](#)
- [114] Guanglai Li, James Besson, Liana Nisimova, Daniel Munger, Panrapee Mahatmr, Jay X Tang, Martin R Maxey, and Yves V Brun. Accumulation of

- swimming bacteria near a solid surface. *Physical Review E*, 84(4):041932, 2011. [24](#), [46](#), [115](#)
- [115] Guanglai Li and Jay X Tang. Accumulation of microswimmers near a surface mediated by collision and rotational brownian motion. *Physical Review Letters*, 103(7):078101, 2009. [24](#)
- [116] Vasily Kantsler, Jörn Dunkel, Marco Polin, and Raymond E Goldstein. Ciliary contact interactions dominate surface scattering of swimming eukaryotes. *Proceedings of the National Academy of Sciences*, 110(4):1187–1192, 2013. [24](#)
- [117] L. Rothschild. Non-random distribution of bull spermatozoa in a drop of sperm suspension. *Nature*, 198(488):1221, 1963. [24](#)
- [118] Diego Lopez and Eric Lauga. Dynamics of swimming bacteria at complex interfaces. *Physics of Fluids (1994-present)*, 26(7):071902, 2014. [26](#)
- [119] Eric Lauga, Willow R DiLuzio, George M Whitesides, and Howard A Stone. Swimming in circles: motion of bacteria near solid boundaries. *Biophysical Journal*, 90(2):400–412, 2006. [26](#), [115](#)
- [120] R Di Leonardo, D Dell’Arciprete, L Angelani, and V Iebba. Swimming with an image. *Physical Review Letters*, 106(3):038101, 2011. [26](#), [75](#), [115](#)
- [121] Jane Hill, Ozge Kalkanci, Jonathan L McMurry, and Hur Koser. Hydrodynamic surface interactions enable *Escherichia coli* to seek efficient routes to swim upstream. *Physical Review Letters*, 98(6):068101, 2007. [26](#)
- [122] Tolga Kaya and Hur Koser. Direct upstream motility in *Escherichia coli*. *Biophysical Journal*, 102(7):1514–1523, 2012. [26](#), [46](#)
- [123] Marcos, Henry C Fu, Thomas R Powers, and Roman Stocker. Bacterial rheotaxis. *Proceedings of the National Academy of Sciences*, 109(13):4780–4785, 2012. [26](#), [46](#)
- [124] Takuji Ishikawa, Tatsuya Shioiri, Keiko Numayama-Tsuruta, Hironori Ueno, Yohsuke Imai, and Takami Yamaguchi. Separation of motile bacteria using drift velocity in a microchannel. *Lab on a Chip*, 14(5):1023–1032, 2014. [26](#), [46](#)

- [125] Bo Li and Sean X Sun. Coherent motions in confluent cell monolayer sheets. *Biophysical Journal*, 107(7):1532–1541, 2014. [27](#), [44](#), [45](#)
- [126] Abhishek Kumar, Ananyo Maitra, Madhuresh Sumit, Sriram Ramaswamy, and GV Shivashankar. Actomyosin contractility rotates the cell nucleus. *Scientific Reports*, 4, 2014. [27](#), [44](#), [45](#)
- [127] Antoine Bricard, Jean-Baptiste Caussin, Nicolas Desreumaux, Olivier Dauchot, and Denis Bartolo. Emergence of macroscopic directed motion in populations of motile colloids. *Nature*, 503(7474):95–98, 2013. [27](#), [115](#), [119](#)
- [128] Yoshio Yotsuyanagi. Recherches sur les phénomènes moteurs dans les fragments de protoplasme isolés: I. mouvement rotatoire et le processus de son apparition. *Cytologia*, 18(2):146–156, 1953. [29](#)
- [129] Yoshio Yotsuyanagi. Recherches sur les phénomènes moteurs dans les fragments de protoplasme isolés. II. Divers mouvements déterminés par la condition de milieu. *Cytologia*, 18:202, 1953. [29](#), [44](#)
- [130] Jan-Willem van de Meent, Andy J Sederman, Lynn F Gladden, and Raymond E Goldstein. Measurement of cytoplasmic streaming in single plant cells by magnetic resonance velocimetry. *Journal of Fluid Mechanics*, 642:5–14, 2010. [29](#)
- [131] Francis G Woodhouse and Raymond E Goldstein. Spontaneous circulation of confined active suspensions. *Physical Review Letters*, 109(16):168105, 2012. [29](#), [31](#), [44](#), [85](#)
- [132] Mathieu Pinot, Villier Steiner, Benoit Dehapiot, Byung-Kuk Yoo, Franck Chesnel, Laurent Blanchoin, Charles Kervrann, and Zoher Gueroui. Confinement induces actin flow in a meiotic cytoplasm. *Proceedings of the National Academy of Sciences*, 109(29):11705–11710, 2012. [31](#)
- [133] AM Jimenez, M Roche, Mathieu Pinot, Pascal Panizza, Laurent Courbin, and Zoher Gueroui. Towards high throughput production of artificial egg oocytes using microfluidics. *Lab on a Chip*, 11(3):429–434, 2011. [31](#)
- [134] Nobuhito Mori and Kuang-An Chang. *Introduction to mPIV*, July 2009. [35](#)

- [135] Christopher Dombrowski, Luis Cisneros, Sunita Chatkaew, Raymond E Goldstein, and John O Kessler. Self-concentration and large-scale coherence in bacterial dynamics. *Physical Review Letters*, 93(9):098103, 2004. [35](#), [46](#), [115](#)
- [136] Amit Rabani, Gil Ariel, and Avraham Be'er. Collective motion of spherical bacteria. *PloS one*, 8(12):e83760, 2013. [35](#), [46](#), [80](#)
- [137] Carl D Meinhart, Steve T Wereley, and Juan G Santiago. A piv algorithm for estimating time-averaged velocity fields. *Journal of Fluids Engineering*, 122(2):285–289, 2000. [35](#)
- [138] Rana Rezakhaniha, Aristotelis Agianniotis, Jelle Tymen Christiaan Schrauwen, Alessandra Griffa, Daniel Sage, CVC Bouten, FN Van de Vosse, Michaël Unser, and Nikolaos Stergiopoulos. Experimental investigation of collagen waviness and orientation in the arterial adventitia using confocal laser scanning microscopy. *Biomechanics and Modeling in Mechanobiology*, 11(3-4):461–473, 2012. [35](#), [36](#)
- [139] ID Vladescu, EJ Marsden, J Schwarz-Linek, VA Martinez, J Arlt, AN Morozov, D Marenduzzo, ME Cates, and WCK Poon. Filling an emulsion drop with motile bacteria. *arXiv preprint arXiv:1407.6859*, 2014. [43](#), [119](#)
- [140] A Costanzo, R Di Leonardo, G Ruocco, and L Angelani. Transport of self-propelling bacteria in micro-channel flow. *Journal of Physics: Condensed Matter*, 24(6):065101, 2012. [47](#), [74](#), [85](#)
- [141] James P Brody, Paul Yager, Raymond E Goldstein, and Robert H Austin. Biotechnology at low reynolds numbers. *Biophysical Journal*, 71(6):3430–3441, 1996. [53](#), [56](#)
- [142] Nicholas Darnton, Linda Turner, Kenneth Breuer, and Howard C Berg. Moving fluid with bacterial carpets. *Biophysical Journal*, 86(3):1863–1870, 2004. [59](#), [84](#)
- [143] Min Jun Kim and Kenneth S Breuer. Microfluidic Pump Powered by Self-Organizing Bacteria. *Small*, 4(1):111–118, 2008. [59](#), [84](#)

- [144] Mario Cachile, Laurent Talon, Juan M Gomba, Jean-Pierre Hulin, and Harold Auradou. Stokes flow paths separation and recirculation cells in x-junctions of varying angle. *Physics of Fluids*, 24(2):021704, 2012. [61](#)
- [145] Kris M Blair, Linda Turner, Jared T Winkelman, Howard C Berg, and Daniel B Kearns. A molecular clutch disables flagella in the *Bacillus subtilis* biofilm. *Science*, 320(5883):1636–1638, 2008. [67](#)
- [146] C Hohenegger and MJ Shelley. *New trends in the physics and mechanics of biological systems.*, volume 92 of *Lecture Notes of the Les Houches Summer School*. July 2009. [74](#)
- [147] Robert Macnab and DE Koshland Jr. Bacterial motility and chemotaxis: light-induced tumbling response and visualization of individual flagella. *Journal of molecular biology*, 84(3):399–406, 1974. [80](#)
- [148] Shengtao Lu, Wuguo Bi, Fang Liu, Xiangyang Wu, Bengang Xing, and Edwin KL Yeow. Loss of Collective Motion in Swarming Bacteria Undergoing Stress. *Physical Review Letters*, 111(20):208101, 2013. [80](#)
- [149] GH Wannier. Antiferromagnetism. the triangular ising net. *Physical Review*, 79(2):357, 1950. [91](#)
- [150] VG Vaks, AI Larkin, and Yu N Ovchinnikov. Ising model with interaction between non-nearest neighbors. *Soviet Physics JETP*, 22:820–826, 1966. [99](#)
- [151] P Azaria, HT Diep, and H Giacomini. Ordering in the centered-square-lattice Ising model. *Physical Review. B, Condensed matter*, 39(1):740–742, 1989. [99](#)
- [152] QN Chen, MP Qin, J Chen, ZC Wei, HH Zhao, B Normand, and T Xiang. Partial order and finite-temperature phase transitions in Potts models on irregular lattices. *Physical Review Letters*, 16:107, 2011. [99](#)
- [153] Sho C Takatori and John F Brady. Towards a 'thermodynamics' of active matter. *arXiv preprint arXiv:1411.5776*, 2014. [113](#)

- [154] Florian Thüroff, Christoph A Weber, and Erwin Frey. Numerical treatment of the boltzmann equation for self-propelled particle systems. *Physical Review X*, 4(4):041030, 2014. [113](#), [115](#)
- [155] SC Takatori, W Yan, and JF Brady. Swim pressure: Stress generation in active matter. *Physical Review Letters*, 113(2):028103, 2014. [113](#)
- [156] Igor S Aranson, Andrey Sokolov, John O Kessler, and Raymond E Goldstein. Model for dynamical coherence in thin films of self-propelled microorganisms. *Physical Review E*, 75(4):040901, 2007. [115](#)
- [157] Andrey Sokolov and Igor S Aranson. Reduction of viscosity in suspension of swimming bacteria. *Physical Review Letters*, 103(14):148101, 2009. [117](#)
- [158] David Seč, Tine Porenta, Miha Ravnik, and Slobodan Žumer. Geometrical frustration of chiral ordering in cholesteric droplets. *Soft Matter*, 8(48):11982–11988, 2012. [119](#)
- [159] Klaus von Klitzing. The quantum hall effect-an edge phenomenon? *Physica B: Condensed Matter*, 184(1):1–6, 1993. [119](#)
- [160] Shuang Zhou, Andrey Sokolov, Oleg D Lavrentovich, and Igor S Aranson. Living liquid crystals. *Proceedings of the National Academy of Sciences*, 111(4):1265–1270, 2014. [120](#)
- [161] François Peaudecerf and Raymond E. Goldstein. Feeding ducks, bacterial chemotaxis, and the gini index. 2014. [120](#)